PLACE IN RETURN BOX to remove this checkout from your record. TO AVOID FINES return on or before date due. MAY BE RECALLED with earlier due date if requested.

DATE DUE	DATE DUE	DATE DUE

11/00 c:/CIRC/DateDue.p65-p.14

NUMERICAL SIMULATIONS OF A DEVELOPING TURBULENT WALL JET ALONG A THERMALLY ACTIVE SURFACE

Ву

Qingtian Wang

A THESIS

Submitted to
Michigan State University
in partial fulfillment of the requirements
for the degree of

MASTER OF SCIENCE

Department of Mechanical Engineering

1999

ABSTRACT

NUMERICAL SIMULATIONS OF A DEVELOPING TURBULENT WALL JET ALONG A THERMALLY ACTIVE SURFACE

By

Qingtian Wang

In support of defogging studies of automotive vehicles, a 2D steady state numerical simulation and phase change modeling for a developing wall jet experimental facility were performed with a commercially available CFD code, FLUENT.

The velocity, temperature, and turbulence fluctuations were predicted with the standard k- ϵ , the realizable k- ϵ , and the Reynolds stress turbulence models. The simulation results were compared to experimental measurements after they were outer and inner scaled. The numerical predictions are in good agreement with the experimental data in outer scaling for isothermal and non-isothermal simulations without phase change.

Two phase change models were developed to perform the mass transfer simulation. The surface phase model was implemented, and gives promising water vapor condensation predictions in comparison with experimental drip-off tests. The volumetric phase change model is analytically established, and needs future work on implementation.

Copyright by Qingtian Wang 1999 To Xiaohui and my family

ACKNOWLEDGMENTS

I wish to express my heartfelt thanks to my advisor, Dr. John J. McGrath, for his constructive supervision and constant support during the entire program.

I would like to thank my committee members, Dr. Tom Shih and Dr. Abraham Engeda, for their advice and assistance.

The experimental data in the present study were collected and processed by Paul Hoke and Rene Neust. I must thank them as their generous contribution makes all the experimental confirmations possible. Meanwhile, I would like to thank Dr. Bashar AdbdulNour and Ford Motor Company for initializing the geometry for the 2D model and the continuous technical support during the course of the study.

I want to thank some of my fellow graduate students for their help: Bin Lian, Gloria Elliot, Al Aksan, and Shi Zheng.

I also want to thank Dr. Jayanta Sanyal and Dr. Aniruddha Mukhopadhyay at FLUENT, INC., for their help in developing the user defined functions.

TABLE OF CONTENTS

TABLE OF C	CONTE	NT	VI
LIST OF TAI	BLES	•••••••••••••••••••••••••••••••••••••••	IX
LIST OF FIG	URES.	•••••••••••••••••••••••••••••••••••••••	X
LIST OF SYI	MBOLS		. XII
CHAPTER 1	INTR	ODUCTION AND BACKGROUND INVESTIGATION	1
1.1	PROBL	EM STATEMENT	1
1.2	BACKG	ROUND INVESTIGATION AND PREVIOUS WORK	3
	1.2.1	Wall Jet: Basic Illustration	3
	1.2.2	Previous Work: Velocity Distribution and	
		Turbulence Quantities	5
	1.2.3	Previous Work: Temperature Distribution and	
		Phase Change	6
1.3	SUMM	ARY	10
CHAPTER2	NUM	ERICAL METHODOLOGY	12
2.1	BASIC	MODELS AND EQUATIONS	12
	2.1.1	Continuity and Momentum Equations	12
	2.1.2	Energy Equation	13
	2.1.3	Species Transport Equation (Concentration Equation)	15
2.2	DISCR	ETIZATION AND MESH GENERATION	16
2.3	TURB	JLENCE MODELS	19
	2.3.1	Standard k-ε Model	22
	2.3.2	Realizable k-ε Model	27
	2.3.3	Reynolds Stress Model (RMS)	30
2.4	NEAR	WALL TREATMENT	31
	2.4.1	The Turbulence Boundary Layer and	

		the Law of the Wall	32
	2.4.2	Near Wall Modeling in FLUENT	36
2.	5 SUMM	1ARY	39
CHAPTE	R 3 SIM	ULATION WITHOUT PHASE CHANGE	40
3.	1 SOLU	TION PROCEDURE	40
	3.1.1	Pre-processing	41
	3.1.2	Model Control	42
	3.1.3	Near Wall Treatment	43
	3.1.4	Unit System	43
	3.1.5	Material Properties	44
	3.1.6	Operating Conditions	45
	3.1.7	Boundary Conditions	45
	3.1.8	Solution Control	47
	3.1.9	Convergence Judgement	48
3.2	2 RESUL	TS AND DISCUSSIONS OF THE	
		ISOTHERMAL SIMULATION	49
	3.2.1	Velocity Profiles	50
	3.2.2	Turbulence Fluctuations	54
3.3	3 RESUL	TS AND DISCUSSIONS OF THE	
		NON-ISOTHERMAL SIMULATION	57
3.4	4 SUMM	ARY	61
CHAPTE	R4 SIM	ULATIONS WITH PHASE CHANGE MODELS	87
4.	1 SOME	BASICS ABOUT MASS TRANSFER	88
	4.1.1	General Mixture	88
	4.1.2	Water Vapor and Dry Air	90
4.2	2 SURFA	ACE PHASE CHANGE MODEL	91
	4.2.1	Model Analysis	92
	4.2.2	Model Implementation	94
	4.2.3	Results and Comparisons	97
4 :	3 VOLUM	METRIC PHASE CHANGE MODEL	108

		4.3.1 Model Analysis	108
		4.3.2 Model Implementation	113
		4.3.3 Results and Comparisons	116
	4.4	SUMMARY AND DISCUSSION	116
CHAF	PTER	5 COCLUSIONS AND RECOMMENDATIONS	
		FOR FUTURE WORK	118
	5.1	SIMULATIONS WITHOUT PHASE CHANGE	118
	5.2	SIMULATIONS WITH PHASE CHANGE	119
APPE	NDIC	CES	122
	Α.	SIMULATIONS OF OUTER-SCALED SNS	123
	В.	SIMULATIONS OF INNER-SCALED	
		FLUCTUATIONS WITH RSM	124
	C.	SIMULATION OF TEMPERATURE PROFILS	
		(OUTER SCALING)	126
	D.	SIMULATION OF THE INNER-SCALED TEMPERATURE	
		PROFILE AND THE HEAT TRANSFER COEFFICIENT	127
	E.	UDF TO IMPOSE SATURATION MASS FRACTION AS	
		BOUNDARY CONDITION AND CALCULATE THE VAPOR MASS	3
		FLUX (SURFACE PHASE CHANGE MODEL)	128
	F.	COMPARISON OF NUMERICAL PREDITION WITH THE	
		SIMILARITY SOLUTION (LAMINAR FLOW, FLAT PLATE)	130
	G.	PREDICTION OF MOLE FRACTION PROFILES OF WATER	
		VAPOR BY THE SURFACE PHASE CHANGE MODEL	131
	H.	USER DEFINED FUNCTION FOR THE VOLUMETRIC PHASE	
		CHANGE MODEL (METHOD (1))	134
	I.	USER DEFINED FUNCTION FOR THE VOLUMETRIC PHASE	
		CHANGE MODEL (METHOD (2))	138
LICT	OE D	REFERENCES	4 4 2
LIGIL	ur K	EFERENLE3	-4/

LIST OF TABLES

TABLE 1	DEFAULT VALUES OF PHYSICAL PROPERTIES	
	OF AIR IN FLUENT	.44

LIST OF FIGURES

PAGE	GURE	FIG
2	ILLUSTRATION OF EXPERIMENTAL SETUP	1.
4	CONFIGURATION OF A 2-D WALL JET	2.
5	THERMAL CONDITIONS OF A WALL JET	3.
	SCHEMATIC OF A HEAT/MASS TRANSFER PROBLEM	4.
7	OVER A FLAT PLATE	
17	CONTROL VOLUME USED FOR DISCRETIZATION	5.
	ZONES IN THE TURBULENCE BOUNDARY LAYER	6.
33	(REPRODUCED FROM [13])	
42	GEOMETRY AND BOUNDARY TYPES OF THE SIMULATION	7 .
63	DEVELOPMENT OF VELOCITY PROFILE	8.
63	PLOT OF VELOCITY MAGNITUDE	9.
64	CONTOURS OF VELOCITY MAGNITUDE	10.
64	CONTOURS OF STATIC PRESSURE	11.
65	VISUALIZATION OF VELOCITY VECTORS	12.
66	VISCOSITY-AFFECTED SUBLAYER (RE _Y < 200)	13.
	COMPARISON OF VELOCITY PROFILES	14.
67	(OUTER SCALING, ske, A)	
	COMPARISON OF VELOCITY PROFILES	15.
68	(OUTER SCALING, ske, B)	
	COMPARISON OF VELOCITY PROFILES	16.
69	(OUTER SCALING, rke, A)	
	COMPARISON OF VELOCITY PROFILES	17.
70	(OUTER SCALING, rke, B)	
	COMPARISON OF VELOCITY PROFILES	18.
71	(OUTER SCALING, RSM, A)	
	COMPARISON OF VELOCITY PROFILES	19.
72	(OUTER SCALING, RSM, B)	

20 .	COMPARISON OF TURBULENT VISCOSITY RATIO (A)	73
21.	COMPARISON OF TURBULENT VISCOSITY RATIO (B)	74
22.	COMPARSION OF VELOCITY PROFILES (INNER SCALING)	75
23.	COMPARISON OF u ⁺ DISTRIBUTION	76
24.	OVERALL INNER-SCALED PREDICTIONS OF	
	u ⁺ DISTRIBUTION (ske)	77
25 .	OVERALL INNER-SCALED PREDICTIONS OF	
	u ⁺ DISTRIBUTION (rke AND RSM)	78
26.	COMPARISON OF SNS (OUTER SCALING, A)	79
27 .	COMPARISON OF SNS (OUTER SCALING, B)	80
28.	COMPARISON OF u'* (INNER SCALING, A)	81
29.	COMPARISON OF u'* (INNER SCALING, B)	82
30.	COMPARISON OF $\overline{v'}$ (INNER SCALING)	83
31.	COMPARISON OF $\overline{u'v'}^{\dagger}$ (INNER SCALING)	84
32 .	COMPARISON OF TEMPERATURE PROFILES	
	IN OUTER SCALING	85
33.	COMPARISON OF INNER-SCALED TEMPERATURE	
	PROFILES AT X/W = 10.8	86
34.	2D FLAT PLATE GEOMETRY	97
35 .	ILLUSTRATION OF FACE AND CELL VALUES	100
36.	COMPARISON OF MASS TRANSFER	
	COEFFICIENT (LAMINAR, FLAT PLATE)	101
37.	RATIO OF ANALYTICAL TO NUMERICAL	
	SOLUTIONS FOR h _m (LAMINAR, FLAT PLATE)	101
38.	PREDICTIONS OF VAPOR MASS FLUX ON THE WALL	103
39.	COMPARISON OF RELATIVE HUMIDITY AT X/W =10.8	104
40.	COMPARISON OF CONDENSATION RATE OF THE PLATE	105
41.	COMPARISON OF SHERWOOD NUMBER	108
42.	CONTROL VOLUME FOR PHASE CHANGE ANALYSIS	111

LIST OF SYMBOLS

c_p specific heat at constant pressure (J/kg-K)

D mass diffusivity (m²/s)

D_{i',m} diffusion coefficient of species i' in the mixture (m²/s)

D_t effective diffusion coefficient due to turbulence (m²/s)

E total internal energy (J/m3)

h heat transfer coefficient (W/m²-K)

h_m local mass transfer coefficient (m/s)

J_{i',i} mass diffusion flux of species i' in i direction (kg/m²-s)

J_w mass flux at the wall (kg/m²-s)

 k, ϵ kinetic energy and its dissipation rate

k_{eff} effective thermal conductivity (W/m-K)

Le Lewis number $Le = \frac{Sc}{Pr} = \frac{\alpha}{D}$

m_{i'} mass of species i' (kg)

m''' volumetric rate of the creation of the water vapor (kg/m³-s)

M_t turbulent Mach number

P_{sat} saturation pressure (Pa)

P_v partial pressure of vapor in the mixture (Pa)

Pr Prandtl number $Pr = \frac{v}{\alpha}$

q"_{app} apparent heat flux (W/m²)

 q''_0 heat flux at y = 0 (wall surface) (W/m²)

R_{i'} mass source (or sink) of species i' (kg/m³-s)

Re_v turbulent Reynolds number

Rew Reynolds number based on the jet nozzle width

S_{i'} mass generation rate of species i' (kg/m³-s)

S_m source term in the mass continuity equation (kg/m³-s)

Sc Schmidt number $Sc = \frac{v}{D}$

Sc_t $Sc_t = \frac{\mu_t}{\rho D_t}$ is the turbulent Schmidt number (default value 0.7)

Sh Sherwood number based on the width of jet nozzle w, $Sh = \frac{h_m w}{D}$

SNS streamwise normal stress, SNS = $100 \frac{\overline{u'}^2}{U_{max}^2}$

T* normalized temperature

T_{dp} dew point temperature (K)

T_{jet} temperature at the jet nozzle (K)

T_s, T₀ temperature of the plate surface (K or °C)

T_{ref} reference temperature (K)

u, v, w velocity components in x, y and z direction (m/s)

 $u_{v_1}v_v$ x and y velocity components of water vapor (m/s)

 u_{τ} friction velocity (m/s)

U velocity magnitude (m/s)

U_{max} maximum velocity magnitude (m/s)

U_{1/2} one half of the maximum velocity magnitude (m/s)

U_{jet} velocity at the jet nozzle (m/s)

w width of the jet nozzle (slot width) (m)

 x^+ , y^+ , u^+ , v^+ wall coordinates

x_{i'} mole fraction of species i'

y_m y location where the velocity takes the maximum value in the profile

(m)

y, u wall units

Greek Letters

 $\alpha \qquad \text{thermal diffusivity } \alpha = \frac{k}{\rho c_P} \text{ (m}^2/\text{s)}$

β coefficient of thermal expansion

 δ_2 y location where velocity magnitude takes the value of U/2 (m)

δij kronecker delta

 ϵ_{M} momentum eddy diffusivity (m²/s)

 ε_H thermal eddy diffusivity (m²/s)

φ relative humidity

 $\Phi_{l'}$ mass fraction of species i'

 Φ_{∞} main stream mass fraction

μ dynamic viscosity (kg/s-m)

 μ_{eff} effective viscosity (kg/s-m)

 μ_t turbulent viscosity (kg/s-m)

v kinetic viscosity (m²/s)

)	density of the mixture (kg/m³)
) _{i'}	mass concentration of species i' (kg/m³)
D _W	mass concentration at the wall (kg/m³)
O∞	mass concentration in the main stream (kg/m³
τ ₀	shear stress at the surface of the wall (Pa)
Cii	stress tensor (Pa)

Chapter 1

INTRODUCTION AND BACKGROUND INVESTIGATION

1.1 Problem Statement

The motivation for the present study was to provide a Computational Fluid Dynamics (CFD) simulation of experimental results related to basic research of the defogger in motor vehicles. Defogging effects on the interior windshield surface is an important safety factor for automobiles. It is generally investigated by experimental tests. Meanwhile, with the development of CFD techniques and its obvious benefits compared to conventional experimental methods, it is desirable to perform satisfactory numerical simulations and predictions to improve the defogger design. The current study is serves as an initial step towards this goal.

An experimental facility was constructed at the Heat Transfer Lab in Department of Mechanical Engineering, Michigan State University [1]. It defines the geometry and boundary conditions for the CFD computation. Therefore, the data obtained from this facility are utilized as experimental verification of the CFD predictions. A commercially available CFD code FLUENT (unstructured version 5.0) was adopted as the tool to implement the numerical simulations. The code runs on a Windows NT 4.0 platform. The hardware is a DELL PC with a 400MHz Pentium II CPU and 256MB RAM.

This thesis is comprised of two foci:

- (1) Prediction of the steady state wall jet velocity and temperature distributions with currently available numerical models that come with the commercial solver; and
- (2) Theoretical analysis and modeling of the fogging phase change phenomenon and its numerical implementation with FLUENT.

 The experimental setup produced by Hoke [1] is depicted in Figure 1.

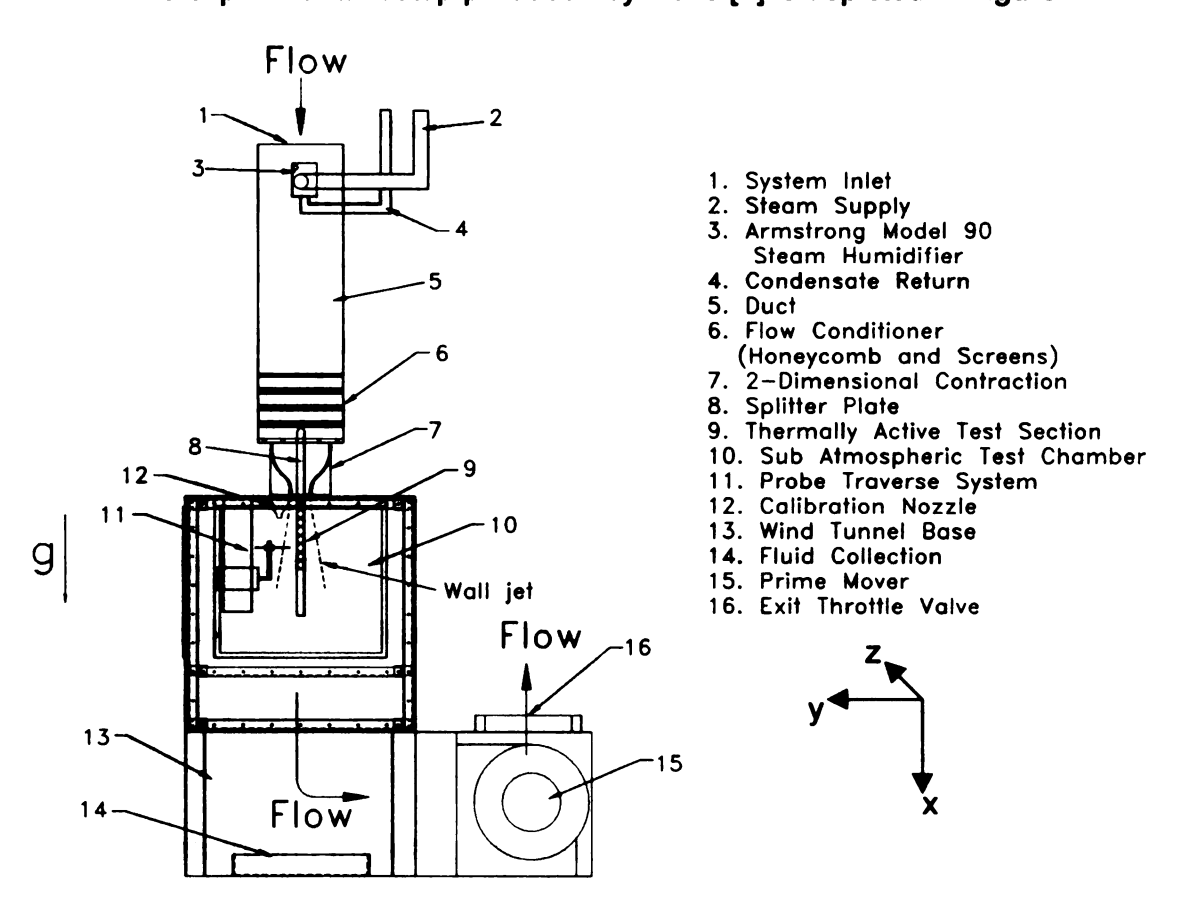


Figure 1. Illustration of Experimental Setup

The region of interest for both the numerical and experimental investigations is the thermally active test section 9 (there are actually two identical regions due to the symmetry of the facility). The design of the experimental facility makes it possible to provide an adjustable flow pattern in this

region. The driving force for the whole system is the pressure differential between the system inlet 1 and wind tunnel base 13 created by the prime mover 15. The pressure driven flow forms two identical wall jets along the thermally active plate surface in 9 after passing through the contraction 7 and being separated by the splitter plate 8. The pressure differential, the temperature of the plate surface and the relative humidity of the flow can all be adjusted according to the experimental needs [1].

The fluid studied is a mixture of water and non-condensable air. The numerical simulation includes investigation of the velocity field, the turbulence quantities, and the temperature field. Meanwhile, since the plate surface temperature T_s is adjustable, a phase change (condensation or evaporation) of water will occur under certain thermal circumstances. When T_s is below the dew point of water, for instance, there will be liquid water condensing onto the wall surface, accompanied with latent heat release. This is of most concern in windshield defogger designing. In turn, modeling the phase change phenomenon becomes very necessary.

1.2 Background Investigation and Previous Work

1.2.1 Wall Jet: Basic Illustration

A wall jet is defined by Launder and Rodi [3] as a shear flow directed along a wall where, by virtue of the initially supplied momentum, at any station, the streamwise velocity over some region within the shear flow exceeds that in the external stream. Some other researchers define a wall jet as a jet of fluid

impinging onto a wall at an angle from 0 to 90 degrees [3] [4]. As a first step of defogger research, the impinging angle of the currently studied wall jet is zero.

Figure 2 defines some basic velocity field configurations of a two dimensional wall jet flowing tangentially to the wall surface (zero impinging angle). In the figure, w is the width of the jet exit nozzle, U_{jet} is the velocity (magnitude) at the slot exit, U_{max} is the maximum velocity of the velocity profile, $U_{1/2} = U_{max} / 2$, y_m is the location where the velocity $U = U_{max}$, and δ_2 is the y location where $U = U_{1/2}$.

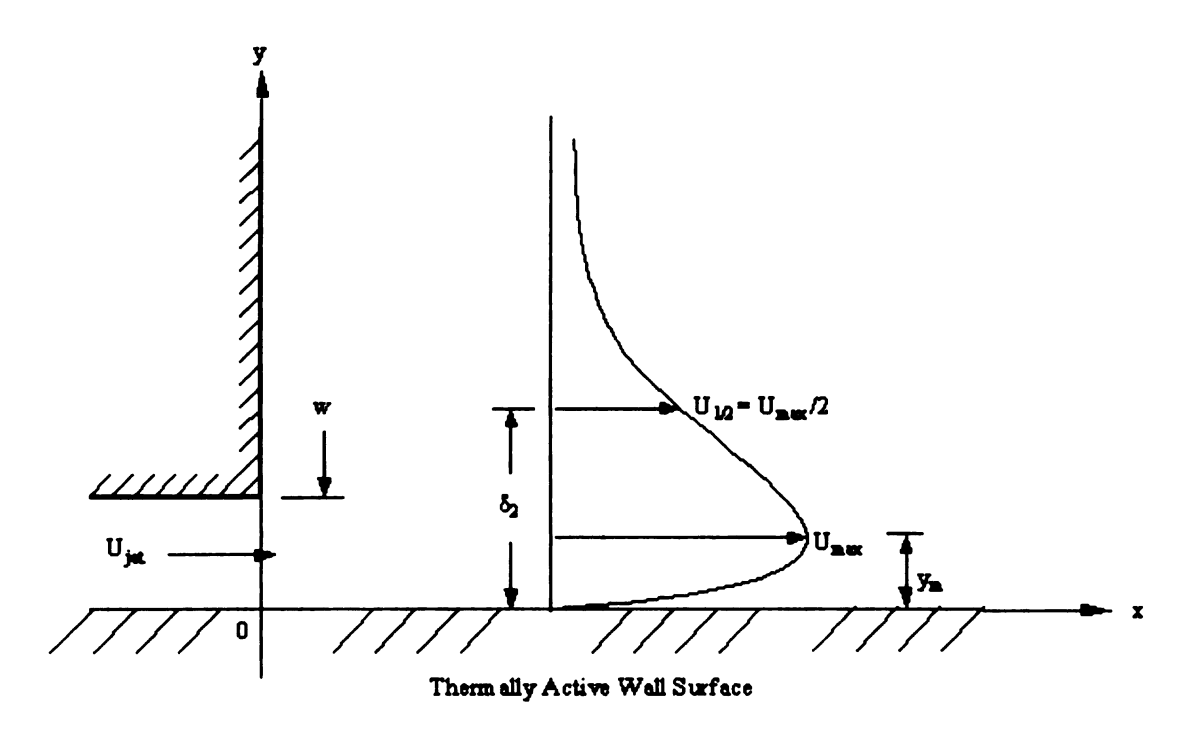


Figure 2. Configuration of a 2-D Wall Jet

If the temperature of the plate surface is different from that of the main stream of the wall jet, the temperature distribution in the wall jet will be of interest. Figure 3 shows a schematic view of the thermal conditions of a typical wall jet with Ts < Tjet, where Ts is the temperature of the isothermal wall surface, Tjet is

the temperature at the jet nozzle, $T\infty$ is the far field temperature, and Tmax is the maximum temperature.

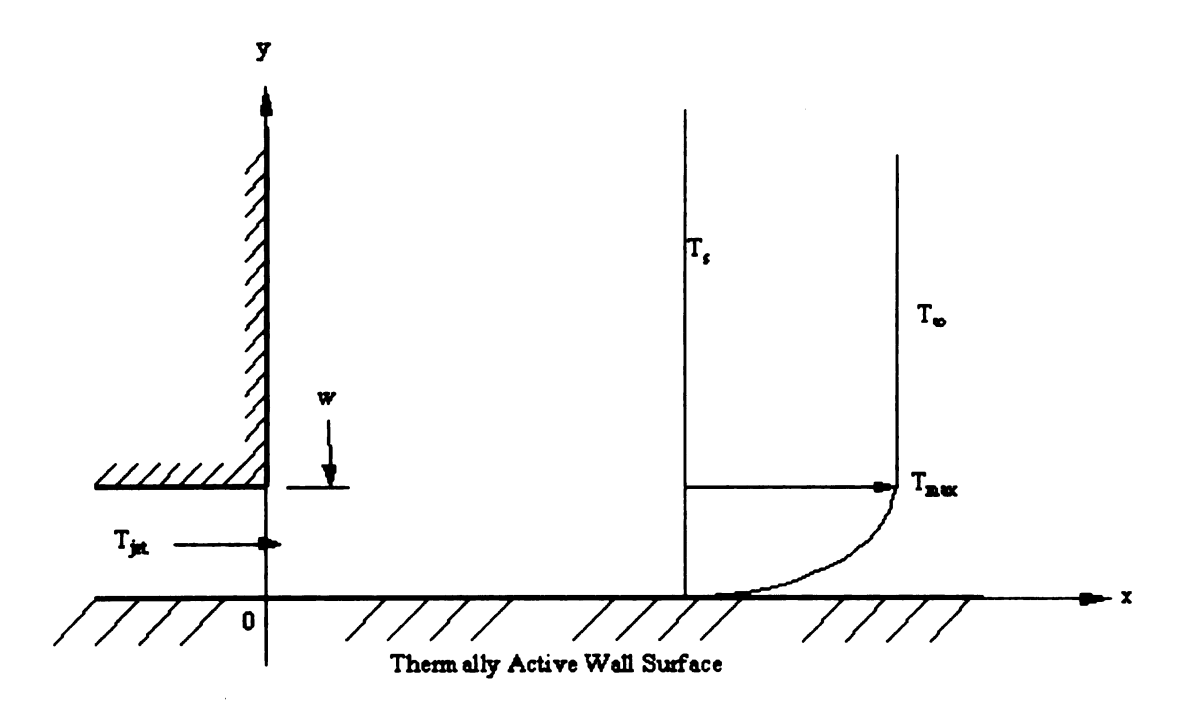


Figure 3. Thermal Conditions of a Wall Jet

Note that the fluid of the wall jet is a mixture of condensable water and non-condensable air. The concentration distribution of water vapor is of importance from the standpoint of phase change and mass transfer. The mass flux on the wall surface due to condensation/evaporation is especially of interest for the study of a defogger.

1.2.2 Previous Work: Velocity Distribution and Turbulence Quantities

The nature of a wall jet has been explored by many former researchers.

Launder and Rodi [2] gave the most comprehensive review of the previous work on the flow field up to 1980. Their attention was mainly focused on the

velocity field and turbulence quantities. Heat and mass transfer were not included.

In 1992, Wygnanski, Katz and Horev [5] published their experimental data in the region where the downstream distance is greater than 20 slot width $(x \ge 20w)$. They claimed that the bulk of the flow is self-similar by outer scaling (U/Umax as a function of y/ δ 2), where the term self-similar (or self-preserving) means that a dimensionless quantity depends on only one lateral or transverse dimensionless variable. Hence, the distribution preserves its normalized shape as the flow proceeds downstream [6]. It is believed that the wall jet was well developed for the case of their research, which is beyond the region of interest for the current study.

Eriksson, Karlson and Persson [7] published velocity and turbulence data for a wider region in 1998. In the lateral direction, their data ranged between 0 to 150 slot widths ($0 \le x \le 150w$). In the transverse direction, they paid special attention to the near wall region and collected data below y+=4 (y+, u+ are inner scaling coordinates) by using the Laser-Doppler (LDV or LDA) technique. The x and y components of the velocity vector can be distinguished with this technique. They found that the data in the range $40 \le x/w \le 150$ was reasonably consistent with similarity, claiming that the mean velocity profiles were self-similar in inner scaling up to y+=100-200, and that the turbulence quantities showed similarity in a much shorter range in terms of y+.

1.2.3 Previous Work: Temperature Distribution and Phase Change

As mentioned previously, if the temperature of the wall surface is different from that of the free stream, the temperature distribution is of interest. Moreover, note that the fluid studied is a mixture of condensable water and non-condensable air. The concentration of water vapor is influenced by the temperature distribution and phase change (condensation/evaporation). For the study of the windshield defogger, the phase change and mass transfer phenomena, especially that on the wall surface and in the near-wall region, are issues of utmost importance.

A simple situation is the so-called "forced convection condensation on a flat plate in the presence of a non-condensable gas", where, in the current study the non-condensable gas is dry air. This is shown in Figure 4, which also shows the dimensional nomenclature and coordinates.

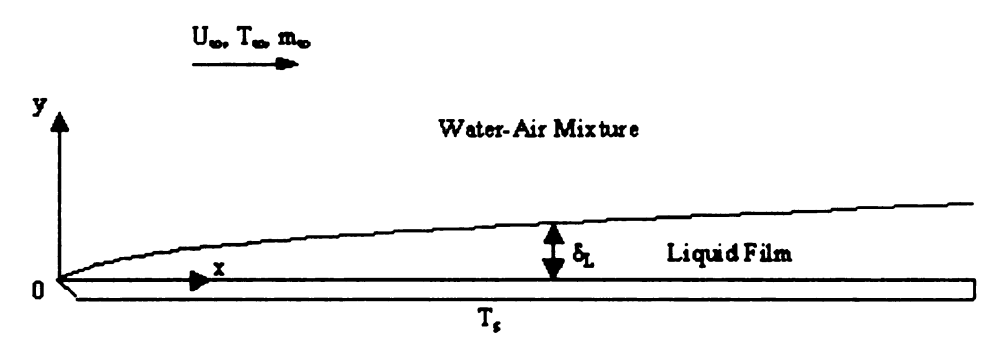


Figure 4. Schematic of a heat/mass transfer problem over a flat plate

U∞, T∞ and m∞ are free stream velocity, temperature and mass fraction of water vapor, respectively. δL is the thickness of the liquid water film on the plate surface due to condensation.

Sparrow, Minkowycz and Saddy [8] worked on the case of laminar flow in the 1960s. The liquid film on the plate surface was included in their analysis by

both numerical and integral methods. It was assumed that the vapor was saturated in the main stream and at the interface between the gaseous phase and liquid film. Furthermore, they assumed the phase change only occurred at the interface. The possible volumetric condensation of water vapor to water droplets in the boundary layer of the water-air mixture was not considered. Therefore, no alteration was needed in the continuity, energy and concentration (species diffusion) equations for the binary gaseous mixture. They claimed that the resistance of the liquid-gas interface to the forced condensation is negligible.

Another investigation of the laminar case was by Hijikata and Mori [9] in 1973. The possibility of volumetric condensation of vapor (i.e. the fog formation) was considered to satisfy the local thermodynamic equilibrium of the water-air mixture. Therefore, the mixture became a two-species (air and water), two-phase (gaseous air-vapor and liquid water droplets) system in their model. Corresponding alterations in the governing equations were made to capture the volumetric phase change (condensation of vapor to liquid droplets) phenomenon. The boundary layer equations were solved by the integral method, assuming the liquid film is "very thin" so that the temperature of the liquid film and that of the interface were assumed equal to the temperature of the plate surface. Their analysis showed that, for a vapor-air mixture with a small temperature difference between the free stream and the plate surface (less than 50°C), the effect of volumetric condensation on the heat and mass flux is dependant upon the relationship between the temperature and concentration difference. If the difference of temperature is dominant compared to that of concentration, the heat flux to the liquid film will not be altered very much by the volumetric condensation, and the mass flux is smaller for the case with condensation than that without. In other words, for the case with thermodynamic equilibrium considered, the temperature distribution does not vary drastically, while the slope of the concentration profile becomes smaller away from the plate surface.

Otherwise, if the concentration difference (i.e. the difference of water vapor mass fraction between the main stream and plate surface) plays a more important role, the heat flux to the liquid film is mainly produced by the latent heat released due to the phase change of mass flux.

The same "thin film" assumption was adopted by Legay-Desesquelles and Prunet-Foch [10]. By using the finite difference method, they numerically solved both laminar and turbulent cases of the problem with volumetric phase change considered. The numerical calculation was compared to experimental data. Their calculation showed that in the case when phase change occurred in the boundary layer, larger heat and mass transfer at the wall were predicted compared to the case of dry air. These results appear to be consistent with the case in Hijikata and Mori's study, in which the concentration difference is dominant compared to the difference of temperature. This seems reasonable since the temperature difference in Legay-Desesquelles and Prunet-Foch's study is less than 20 °C.

The most comprehensive analysis of the laminar case was carried out by Matuszkiewicz and Vernier [11] in 1991. Instead of adopting the "thin film" assumption, the effect of liquid film was taken into account analytically.

Moreover, the liquid phase in the main stream was modeled by analyzing the mass fraction of liquid water (droplets). The concept of "source terms" in the species diffusion and energy equations was explicitly introduced to take care of the overall phase change phenomenon. Their results showed that for fluid with Lewis number Le < 1 (which is the case for vapor-air mixture), the saturated condition does not hold all the way through the boundary layer unless the droplet (water liquid) mass fraction in the main stream has a certain minimum value. In other words, if the droplet mass fraction is less than the minimum value, there exits regions in the boundary layer where the water vapor is superheated. For Le > 1, the saturated condition holds throughout the boundary layer whatever value the main stream droplet mass fraction takes. They found that the heat flux to the wall surface is only slightly influenced by the presence of droplets in the condensation boundary layer. Also, the "thin film" assumption is only valid when the vapor mass fraction is very low. That is, the assumption is valid for the airvapor system since the mass fraction of water vapor is usually less than 0.1.

It is also worth mentioning that in the analysis of all the researchers, the assumption that the interface is impermeable to non-condensable air was made. Therefore, the transverse velocity component of non-condensable air was set to be zero for the boundary (or jump) condition at the interface.

1.3 Summary

As can be seen from the previous analysis, the task of simulating a wall jet is complicated, especially when it is coupled with heat transfer and phase change

phenomenon. Extensive modeling work is needed for the coupling of heat and mass transfer. The goal of the current study is to tackle this task numerically with the commercially available tool FLUENT. A better understanding of this problem through the CFD study can serve as the first step towards the optimization of windshield defogger design.

Chapter 2

NUMERICAL METHODOLOGY

The commercial software FLUENT is utilized as a workbench to carry numerical computation and implement necessary physical models developed by the user. It should be pointed out that it is not the focus of the current study to improve the numerical methodology (such as the turbulence models) of the code. Nevertheless, the comparison between the simulation and experimental data may provide suggestions on choosing the appropriate numerical methods (turbulence models, for instance).

It is beneficial, however, to know what is available in commercial CFD package. Following is a brief introduction to the relative numerical methodology employed by FLUENT, and some necessary background physical theories.

2.1 Basic Models and Equations

2.1.1 Continuity and Momentum Equations

FLUENT solves conservation equations for mass and momentum for all flows. For flows with heat transfer, the energy conservation equation is solved. For flows involving species which are mixing or reacting, FLUENT solves the species conservation equation. Additional transport equations are also solved when the flow is turbulent.

The continuity equation, or conservation equation of mass, solved by FLUENT takes the form [12]:

$$\frac{\partial \rho}{\partial t} + \frac{\partial}{\partial x_i} (\rho u_i) = S_m \tag{2.1}$$

This is a general form of continuity equation and is valid for both incompressible and compressible flows. S_m (kg/m³-s) includes the source term of mass added to the continuous phase from the dispersed second phase (e.g. due to vaporization of liquid droplets) and any user-defined sources.

Later in the current study, a user-defined source term will be introduced to take into account the condensation/evaporation of water.

In an inertial (non-accelerating) system, the momentum equation (Navier-Stokes Equation) in the *i* direction solved by FLUENT is:

$$\frac{\partial}{\partial t}(\rho u_i) + \frac{\partial}{\partial x_i}(\rho u_i u_i) = -\frac{\partial p}{\partial x_i} + \frac{\partial \tau_{ij}}{\partial x_i} + \rho g_i + F_i$$
 (2.2)

where p is the static pressure, ρg_i is the gravitational body force, F_i (N/m³) are the external body forces in the *i* direction and other model-dependent source terms such as porous media user-defined sources, and τ_{ij} is the stress tensor given by [13]:

$$\tau_{ij} = \mu \left(\frac{\partial u_i}{\partial x_j} + \frac{\partial u_j}{\partial x_i} \right) - \frac{2}{3} \mu \frac{\partial u_k}{\partial x_k} \delta_{ij}$$
 (2.3)

where μ is the dynamic viscosity and δ_{ij} is the Kronecker delta function (δ_{ij} =1 if i = j and δ_{ij} = 0 if i \neq j). The second term on the right-hand side is the effect of volume dilation.

2.1.2 Energy Equation

FLUENT can solve a heat transfer problem within both fluid and solid regions in the computational domain. The energy equation solved in FLUENT takes the following form:

$$\frac{\partial}{\partial t}(\rho E) + \frac{\partial}{\partial x_i} \left[u_i (\rho E + p) \right] = \frac{\partial}{\partial x_i} \left[k_{eff} \frac{\partial T}{\partial x_i} - \sum_{j'} h_{j'} J_{j'} + u_j (\tau_{ij})_{eff} \right] + S_h \qquad (2.4)$$

 S_h (W/m³) is the source term for chemical reaction, and any other user-defined volumetric source. The first three terms on the right-hand side of equation (2.4) represent heat transfer due to conduction, species diffusion and viscous dissipation, respectively. k_{eff} is the effective thermal conductivity; and $(\tau_{ij})_{eff}$ is the deviatoric stress tensor. They will be discussed more in turbulence models. $J_{j'}$ is the diffusion flux of species i'.

In equation (2.4), E is the total energy

$$E = h - \frac{p}{\rho} + \frac{u_i^2}{2} \tag{2.5}$$

where h is the sensible enthalpy. If $\Phi_{j'}$ is the mass fraction of species j', h is defined as

$$h = \sum_{j'} \Phi_{j'} h_{j'} \tag{2.6}$$

for an ideal gas. And for incompressible flow,

$$h = \sum_{j'} \Phi_{j'} h_{j'} + \frac{p}{\rho}$$
 (2.7)

where hi is given by

$$h_{j'} = \int_{T_{n'}}^{T} c_{p,j'} dT \tag{2.8}$$

The reference temperature T_{ref} in FLUENT is 298.15 K.

2.1.3 Species Transport Equation (Concentration Equation)

FLUENT models the mixing and transport of chemical species by solving the conservation equation of convection, diffusion and reaction sources for each individual species. Therefore, it can be used to model species transport with or without chemical reaction. The four reaction modeling approaches available are:

- Generalized finite formulation
- Mixture fraction/PDF formulation
- Non-equilibrium (flamelet) formulation
- Premixed combustion formulation

None of these models will be used for the present problem.

FLUENT predicts the local mass fraction for each species, $\Phi_{i'}$, by solving the convection-diffusion equation for the i'th species. The general form of this equation is

$$\frac{\partial}{\partial t} (\rho \Phi_{i'}) + \frac{\partial}{\partial x_i} (\rho u_i \Phi_{i'}) = -\frac{\partial}{\partial x_i} J_{i',i} + R_{i'} + S_{i'}$$
(2.9)

Equation (2.9) is also known as the "concentration equation" [14], in which $R_{i'}$ is the mass source (or sink) due to chemical reaction, and $S_{i'}$ (kg/m³-s) is the mass generation rate by addition from the dispersed phase and other user-defined sources.

In laminar flows, $J_{i',i}$ is the diffusion flux of species i' due to the concentration gradient in the i direction. FLUENT uses the dilute approximation, under which $J_{i',i}$ can be written as

$$J_{i',i} = -\rho D_{i',m} \frac{\partial \Phi_{i'}}{\partial x_i} \tag{2.10}$$

where $D_{i',m}$ (m²/s) is the diffusion coefficient of species i' in the mixture, and is also known as the mass diffusivity or diffusion constant [14]. Equation (2.10) takes the same form as Fick's Law for a binary mixture.

In turbulent flows, the mass diffusion flux is computed by

$$J_{i',i} = -\left(\rho D_{i',m} + \frac{\mu_i}{Sc_i}\right) \frac{\partial \Phi_{i'}}{\partial x_i}$$
 (2.11)

where $Sc_t = \frac{\mu_t}{\rho D_t}$ is the turbulent Schmidt number with a default value of 0.7, μ_t is

the turbulent eddy viscosity, and D_t is the effective diffusion coefficient due to turbulence.

The transport of enthalpy due to species diffusion

$$\nabla \cdot \left[\sum_{i'=1}^{N} (h_{i'}) J_{i'} \right]$$

is not negligible for many mixture flows, especially when the Lewis number

$$Le = \frac{Sc}{Pr} = \frac{\alpha}{D} = \frac{\rho c_p}{kD}$$

is far from unity (If air ($Pr = \frac{v}{\alpha} = 0.7$) is the main fluid, $Sc = \frac{v}{D}$ of water is 0.6, and

Le is 0.86 [14]). Here $\alpha = \frac{k}{\rho c_p}$ is the thermal diffusivity, v is the kinetic viscosity,

and D is the mass diffusivity.

2.2 Discretization and Mesh Generation

The finite volume method (FVM) is used in FLUENT to convert the governing equations to algebraic equations that can be solved numerically.

In the finite volume approach, the integral form of the governing equations is solved. The discrete nature of the computational model is recognized at the outset. This feature is shared in common with the finite element method (FEM).

Instead of solving the equations at points of the computational domain, as is the case for the finite difference method (FDM), in FVM the physical domain is divided into small volumes (or areas for 2-D cases) known as control volumes. The physical law is satisfied over a finite region rather than only at a point as the mesh is shrunk to zero. The governing equations are integrated for each control volumes, which yields discrete equations that convert each quantity to a control-volume basis. A distinctive character of FVM is that a "balance" of a physical quantity is always maintained for the control volume in the neighborhood of each grid point.

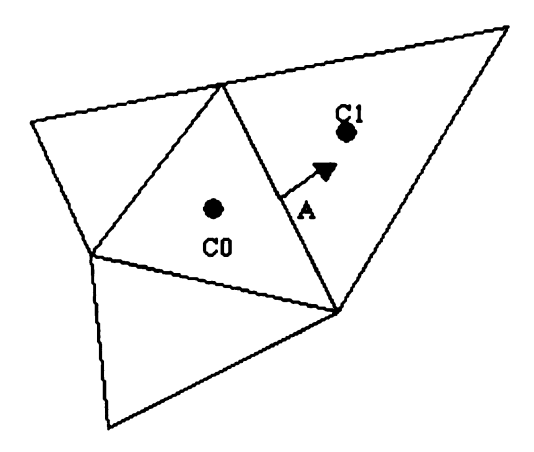


Figure 5. Control Volume used for Discretization

FLUENT stores the discrete values of the physical quantity at the cell centers (C0 and C1 in Figure 5) of the control volumes as shown in Figure 5.

The convection terms in the governing equations require the face values, which are interpolated from the center values. This is obtained by an upwind scheme. "Upwinding" means that the face value is derived from the quantities in the upstream cell relative to the normal velocity direction.

The first order upwind accuracy was employed in the present study as no significant difference was observed compared to the second order scheme in predicting the outer scaled velocity profiles (outer scaling will described in section 3.2.1).

An advantage of the finite volume method (FVM) over the finite difference method (FDM) is that the use of an unstructured mesh is allowed, since arbitrary volumes can be utilized to subdivide the physical domain. This is very important when the physical domain is highly irregular and complicated, where a structured mesh would be difficult to construct. Also, since the integral equations are solved directly in the physical domain, no coordinate transformation from physical to computational domain is needed [13].

FLUENT 5.0 is an unstructured solver. It uses internal data structures to assign an order to the cells, faces and grid points in the mesh, and to maintain contact between adjacent cells. Therefore, it does not require (i, j, k) indexing to locate neighboring cells. The solver does not force an overall structure or topology on the grid [12]. This provides a flexibility to use the grid topology that is best for the specific problem of interest. In addition, for a complicated physical

domain, an unstructured mesh is much easier to generate compared to a structured one. When an unstructured approach is employed, the unstructured mesh generator (Gambit is the so-called pre-processor used by FLUENT to generate the mesh.) is used to create the grids automatically, and the user can concentrate his/her effort on defining the configuration of interest.

As a trade-off, unstructured grids require the connectivity information to be stored cell-by-cell as opposed to block-by-block. Additional storage, therefore, is necessary compared to the structured approach. From the standpoint of solver efficiency, unstructured solvers are usually not as computationally efficient as their structured counterparts [13]. Also when doing mesh generation, one needs to keep in mind that numerical diffusion can be minimized when the flow is aligned with the mesh [12].

In the present study, the mesh was refined from $y^+ \cong 3$ to $y+ \cong 1$ for the wall adjacent cells of the thermally active surface without significant difference observed in the prediction for the outer-scaled mean velocity (more about y^+ and outer scaling can be found in section 2.4.1 and 3.2.1, respectively).

2.3 Turbulence Models

The Reynolds number based on the jet nozzle width, Re_w, for the current study is

$$Re_{w} = \frac{\rho U_{jet} w}{\mu} \approx 1.3 \times 10^{4}$$

The flow is believed to be turbulent based on this number.

Turbulent fluid motion is an irregular condition of flow in which the various quantities show a random variation with time and space coordinates so that statistically distinct average values can be discerned [15]. In the conventional Reynolds decomposition, the randomly changing flow variables are defined as

$$f = \bar{f} + f' \tag{2.12}$$

where f is the symbolic flow variable, \bar{f} is the time-averaged quantity, and f' is the fluctuating component. The time-averaged quantity, \bar{f} , is defined as

$$\bar{f} = \frac{1}{\Lambda t} \int_{t_0}^{t_0 + \Delta t} f dt \tag{2.13}$$

where Δt should be large compared to the period of fluctuations of the turbulence, but small compared to the time constant for any slow variations associated with ordinary unsteady flow.

By definition, for symbolic flow variables f and g

$$\overline{f'} \equiv 0, \qquad \overline{fg'} = 0, \qquad \overline{fg} = \overline{fg}, \qquad \overline{f+g} = \overline{f} + \overline{g}$$
 (2.14)

Note that $\overline{ff'} \neq 0$. In fact, the root mean square of the velocity fluctuations is defined as the turbulence intensity.

Compared to laminar flows, turbulent flows are usually associated with higher values of friction drag and pressure drop, and the diffusion rates of scalar quantities are usually larger.

It is known that the unsteady Navier-Stokes equations are the governing equations for turbulent flows in the continuum regime. However, solving those equations directly, which is known as Direct Numerical Simulation (DNS) of turbulent flows, is limited by current computational resources. Although

techniques like parallel processing are showing promising progress [16], it is still computationally too expensive to simulate directly in practical engineering problems. Instead, the exact governing equations are manipulated to remove the small scales. This results in a modified set of equations that are less expensive to solve. The modification, however, brings in additional unknown variables. Turbulence models, therefore, are needed to connect these variables to the known quantities and achieve "closure" to the modified equation set.

With the above-mentioned Reynolds decomposition, the instantaneous (exact) continuity and momentum equations can be time (Reynolds, or ensemble) averaged. Dropping the over bar on the mean velocity, \overline{u} , the so-called Reynolds-Averaged Navier-Stokes (RANS) equations can be written in the Cartesian tensor form as:

$$\frac{\partial \rho}{\partial t} + \frac{\partial}{\partial x_i} (\rho u_i) = 0 \tag{2.15}$$

$$\rho \frac{Du_i}{Dt} = -\frac{\partial p}{\partial x_i} + \frac{\partial}{\partial x_j} \left[\mu \left(\frac{\partial u_i}{\partial x_j} + \frac{\partial u_j}{\partial x_i} - \frac{2}{3} \delta_{ij} \frac{\partial u_k}{\partial x_k} \right) \right] + \frac{\partial}{\partial x_j} \left(-\rho \overline{u_i' u_j'} \right)$$
(2.16)

Compared to the instantaneous Navier-Stokes equations, now the velocities and other variables represent time-averaged (mean) values.

The additional terms, $-\rho u_i^{\prime} u_j^{\prime}$, are called Reynolds stresses, which represent the turbulence effects. These terms are the ones that need to be modeled in order to close equation (2.16). The turbulence models employed in the current study are briefly introduced. More details for the standard k- ε model are given as an example of how the turbulence models work.

It is worth noting that there does not exist single turbulence model that is superior for all kinds of problems. The choice of turbulence model generally depends on the physics of the specific problem, practical experience for a specific class of problems, the available computational resources, and the amount of time required for the simulation. Therefore, a basic understanding of various models is needed for an appropriate choice.

2.3.1 Standard k-€ Model

Two-equation models are the simplest "complete models" of turbulence [12], in which the turbulent velocity and length scales are independently determined by solving two separate transport equations. The standard k- ε model in FLUENT belongs to this turbulence model class. It is a semi-empirical model based on the calculation of the turbulence kinetic energy (k) and its dissipation rate (ε), where the turbulent kinetic energy (k) is defined as

$$k = \frac{1}{2} \overline{u_i' u_i'}$$
 (2.17)

and ε can be written as

$$\varepsilon = C_d \frac{k^{3/2}}{I} \tag{2.18}$$

where C_d is a drag coefficient approximately equal to 1, and L is the diameter of an imaginary fluid mass packet [17].

Note that in FLUENT, a related quantity output, the turbulent intensity, is given by

$$I = \frac{\sqrt{\frac{2}{3}k}}{V} \tag{2.19}$$

where k is the turbulent kinetic energy, and V is a reference mean velocity magnitude specified by the user in "reference values" with a default value of 1m/s. This definition is inconsistent with the usual definition of turbulence intensity where the numerator in (2.19) is the local mean fluctuation, and V is the local mean velocity. When imposed as boundary conditions, however, the turbulence intensity takes the definition in the usual sense.

The transport equation of k is derived from the complete momentum equations (detailed procedure and be found in reference [17]). The transport equation for ε , however, is obtained by physical reasoning and bears little resemblance to its mathematically exact counterpart [12].

The assumption in the derivation of the model is that the flow is fully turbulent, and that the effects of molecular viscosity are negligible. Therefore, the standard k- ϵ model is valid only for fully turbulent flows.

Boussinesq Hypothesis and Modeling of Turbulent Viscosity

To model the Reynolds stresses, $-\rho \overline{u_i} \overline{u_j}$, the Boussinesq hypothesis

$$-\rho \overline{u_i' u_j'} = \mu_i \left(\frac{\partial u_i}{\partial x_j} + \frac{\partial u_j}{\partial x_i} \right) - \frac{2}{3} \left(\rho k + \mu_i \frac{\partial u_i}{\partial x_i} \right) \delta_{ij}$$
 (2.20)

is adopted in k- ϵ models, which suggests that the apparent turbulent shear stresses is related to the rate of mean strain through an apparent scalar, namely, the turbulent or "eddy" viscosity. In equation (2.20), μ_t is the eddy viscosity, k is the turbulent kinetic energy, and δ_{ii} is the Kronecker delta.

The turbulent viscosity, μ_t , is modeled in terms of k and ϵ :

$$\mu_{\iota} = \rho C_{\mu} \frac{k^2}{\varepsilon} \tag{2.21}$$

where C_μ is a constant. It is clear that two additional transport equations for k and ϵ are needed to close the system.

Transport Equations for the Standard k-€ Model

The two transport equations for the turbulent kinetic energy, k, and its dissipation rate, ε , are

$$\rho \frac{Dk}{Dt} = \frac{\partial}{\partial x_i} \left[\left(\mu + \frac{\mu_i}{\sigma_k} \right) \frac{\partial k}{\partial x_i} \right] + G_k + G_b - \rho \varepsilon - Y_M$$
 (2.22)

$$\rho \frac{D\varepsilon}{Dt} = \frac{\partial}{\partial x_i} \left[\left(\mu + \frac{\mu_i}{\sigma_i} \right) \frac{\partial \varepsilon}{\partial x_i} \right] + C_{1\varepsilon} \frac{\varepsilon}{k} \left(G_k + C_{3\varepsilon} G_b \right) - C_{2\varepsilon} \rho \frac{\varepsilon^2}{k}$$
 (2.23)

In equation (2.22) and (2.23), G_k represents the generation of turbulent kinetic energy due to the mean velocity gradients. G_b represents the generation of turbulent kinetic energy due to buoyancy. Y_M represents the contribution of the fluctuating dilation in compressible turbulence due to the overall dissipation rate. $C_{1\epsilon}$, $C_{2\epsilon}$ and $C_{3\epsilon}$ are constants. σ_k and σ_ϵ are the turbulent Prandtl numbers for k and ϵ , respectively.

Furthermore, G_k , G_b and Y_M are modeled in terms of the known flow variables so that the entire system is brought to a "closure":

Gk represents the production of turbulent kinetic energy, and is defined as

$$G_k = -\rho u_i u_j \frac{\partial u_j}{\partial x_i}$$
 (2.24)

Or, to be consistent with the Boussinesq hypothesis.

$$G_{k} = \mu_{k} S^{2} \tag{2.25}$$

where S is the modulus of the mean rate-of-strain tensor, defined as

$$S = \sqrt{2S_{ij}S_{ij}} \tag{2.26}$$

with the mean strain rate Sii given by

$$S_{ij} = \frac{1}{2} \left(\frac{\partial u_i}{\partial x_j} + \frac{\partial u_j}{\partial x_i} \right) \tag{2.27}$$

G_b is written as

$$G_b = \beta g_i \frac{\mu_i}{\text{Pr}_i} \frac{\partial T}{\partial x_i}$$
 (2.28)

where Pr_t is the turbulent Prandtl number for energy with a default value 0.85 in FLUENT. β is the coefficient of thermal expansion, defined as

$$\beta = -\frac{1}{\rho} \left(\frac{\partial \rho}{\partial T} \right)_{n} \tag{2.29}$$

 Y_{M} takes into account the compressibility effects for high Mach number flows:

$$Y_{M} = 2\rho \varepsilon M_{L}^{2} \tag{2.30}$$

where Mt is the turbulent Mach number, defined as

$$M_{t} = \sqrt{\frac{k}{a^2}} \tag{2.31}$$

where a is the speed of sound, and k is the turbulent kinetic energy.

Model Constants

The constants in equations (2.21), (2.22) and (2.23) take the following default values in FLUENT:

$$C_{1\varepsilon}=1.44$$
, $C_{2\varepsilon}=1.92$, $C_{\mu}=0.09$, $\sigma_{k}=1.0$, $\sigma_{\varepsilon}=1.3$

These values come from experiments with air and water for fundamental turbulent shear flows, and have been found to work well for a wide range of wall-bounded and free shear flows. Users are able to adjust these default values in FLUENT.

Heat and Mass Transfer Modeling

Turbulent heat transfer is modeled using the concept of Reynolds' analogy to turbulent momentum transfer. The "modeled" energy equation has already been given by equation (2.4).

$$\frac{\partial}{\partial t}(\rho E) + \frac{\partial}{\partial x_i} \left[u_i(\rho E + p) \right] = \frac{\partial}{\partial x_i} \left[k_{eff} \frac{\partial T}{\partial x_i} - \sum_{i'} h_{i'} J_{j'} + u_j(\tau_{ij})_{eff} \right] + S_h$$

The term involving $(\tau_{ij})_{eff}$ represents the viscous heating. The deviatoric stress tensor, $(\tau_{ij})_{eff}$, is defined as

$$\left(\tau_{ij}\right)_{eff} = \mu_{eff} \left(\frac{\partial u_j}{\partial x_i} + \frac{\partial u_i}{\partial x_j}\right) - \frac{2}{3} \mu_{eff} \frac{\partial u_i}{\partial x_i} \delta_{ij}$$
 (2.32)

Note the difference between equation (2.32) and (2.3). The effective thermal conductivity k_{eff} and μ_{eff} are given by

$$k_{eff} = k + k_{l} \tag{2.33}$$

and

$$\mu_{eff} = \mu + \mu_t \tag{2.34}$$

where kt is the turbulent thermal conductivity

$$k_{t} = \frac{c_{p}\mu_{t}}{\text{Pr}_{t}} \tag{2.35}$$

with the default value of the turbulent Prandtl number, Pr set to 0.85.

Similar treatment is applied to turbulent mass transfer. Note that in equation (2.11), the turbulent Schmidt number takes the default value 0.7.

2.3.2 Realizable k-€ Model

There are two main deficiencies in traditional k-ε models.

First, by combining the Boussinesq hypothesis (2.19) and the definition of eddy viscosity (2.20) and keeping C_{μ} as a constant, a negative value may be obtained for the normal stress, $\overline{u'^2}$, which is supposed to be positive. Meanwhile, the so-called Schwarz inequality for shear stresses can be violated. This "non-realizable" case happens when the strain is large enough [12]. The way to ensure "realizable" is to make C_{μ} variable according to the mean flow (mean deformation) and the turbulence (k, ϵ).

Second, the modeled transport equation of ϵ in traditional k- ϵ models is believed to be responsible for the unexpectedly poor prediction of the spreading rate for axisymetric jets (the well-known round-jet anomaly).

The realizable k- ϵ model is intended to address the above mentioned weaknesses by adopting:

 \blacksquare A new eddy-viscosity formula with a variable C_{μ}

27

 A new transport equation for ε based on the dynamic equation of the mean-square vorticity fluctuation

Modeling the Turbulent Viscosity

In the realizable k- ϵ model, the turbulent viscosity takes the same form as that in the standard k- ϵ model (2.20).

$$\mu_{\iota} = \rho C_{\mu} \frac{k^2}{\varepsilon}$$

However, C_{μ} is no longer a constant:

$$C_{\mu} = \frac{1}{A_0 + A_s \frac{U^* k}{\epsilon}} \tag{2.36}$$

where

$$U^* \equiv \sqrt{S_{ij}S_{ij} + \widetilde{\Omega}_{ij}\widetilde{\Omega}_{ij}}$$
 (2.37)

and

$$\widetilde{\Omega}_{ii} = \Omega_{ii} - 2\varepsilon_{iik}\omega_k$$

$$\Omega_{ij} = \overline{\Omega_{ij}} - \varepsilon_{ijk}\omega_k$$

where $\overline{\Omega_{ij}}$ is the mean rate-of-rotation tensor viewed in the rotating reference frame with the angular velocity ω_k . The model constants A_0 and A_s are given by

$$A_0 = 4.04$$
 , $A_s = \sqrt{6}\cos\phi$

where

$$\phi = \frac{1}{3} \arccos(\sqrt{6}W), \quad W = \frac{S_{ij}S_{jk}S_{ki}}{\widetilde{S}}, \qquad \widetilde{S} = \sqrt{S_{ij}S_{ij}}$$

Therefore, C_{μ} is a function of the mean strain and rotation rates, the angular velocity of the system rotation, and the turbulence fields (k, ϵ).

Transport Equations for the Realizable k-€ Model

In the realizable k- ε model, the transport equations for k and ε are

$$\rho \frac{Dk}{Dt} = \frac{\partial}{\partial x_j} \left[\left(\mu + \frac{\mu_t}{\sigma_k} \right) \frac{\partial k}{\partial x_j} \right] + G_k + G_b - \rho \varepsilon - Y_M$$
 (2.38)

and

$$\rho \frac{D\varepsilon}{Dt} = \frac{\partial}{\partial x_i} \left[\left(\mu + \frac{\mu_i}{\sigma_k} \right) \frac{\partial \varepsilon}{\partial x_i} \right] + \rho C_1 S\varepsilon - \rho C_2 \frac{\varepsilon^2}{k + \sqrt{v\varepsilon}} + C_{1\varepsilon} \frac{\varepsilon}{k} C_{3\varepsilon} G_b$$
 (2.39)

where

$$C_1 = \max \left[0.43, \frac{\eta}{\eta + 5} \right]$$

and

$$n = Sk / \varepsilon$$

Note that the transport equation for k is the same as that for the standard k- ϵ model, while the one for ϵ is quite different.

Model Constants

$$C_{1\varepsilon} = 1.44$$
, $C_2 = 1.9$, $\sigma_k = 1.0$, $\sigma_{\varepsilon} = 1.2$

Heat and Mass Transfer Modeling

The modeling of heat and mass transfer for the realizable k- ϵ model is the same as that of the standard k- ϵ model.

It has been found that the realizable k-ε model is substantially better in predicting flows like rotating homogeneous shear flows, free flows including jets and mixing layers, channel and boundary layer flows and separate flows. In particular, it resolves the round-jet anomaly which occurs in standard k-ε model.

2.3.3 The Reynolds Stress Model (RMS)

The Reynolds Stress Models differ from the k- ϵ models in that the isotropic eddy-viscosity assumption is abandoned, and turbulent shearing stress is not assumed to be proportional to the rate of mean strain. That is, in a 2-D incompressible flow,

$$-\rho\overline{u'v'}\neq\mu_{\iota}\left(\frac{\partial u}{\partial y}+\frac{\partial v}{\partial x}\right).$$

Reynolds Stress Models are more general than those based on the Boussinesq assumption and are expected to give better predictions for flows with sudden change in the mean strain rate or with effects such as streamline curvature or gradients in the Reynolds normal stresses [13]. Meanwhile, it is also more computationally expensive compared to the two-equation models.

The Reynolds Stress Model (RSM) provided in FLUENT closes the Reynolds-averaged Navier-Strokes equations by solving the transport equations for the Reynolds stresses and an equation for the dissipation rate. The transport equations for the Reynolds stresses are derived by taking the moments of the

exact momentum equations. For instance, in 2-D incompressible flow, the *i*th exact momentum equation is multiplied by the fluctuating velocity component u_j' and then the product of u_i' and the *j*th momentum equation are added. The results are then Reynolds-averaged:

$$\frac{1}{u_i N_j + u_j N_i} = 0 {(2.40)}$$

where N_i and N_j are the *i*th and *j*th components of the Navier-Stokes equation, respectively. This kind of manipulation results in four additional equations in 2D flows, and seven additional equations in 3D flows.

Several terms in the exact transport equation (2.40) are unknown, and turbulence models are required to close the equations. Details of modeling for these terms can be found in [12].

In the Reynolds stress model, FLUENT solves the equation for turbulent kinetic energy (k) that is essentially identical to that of the standard k- ϵ model in the entire computational domain, but the k obtained is used only for boundary conditions. For cases other than the boundary condition, k is obtained by taking the trace of the Reynolds stress tensor (2.17):

$$k = \frac{1}{2} \overline{u_i' u_i'}$$

The dissipation tensor, ϵ_{ij} , is modeled as

$$\varepsilon_{ij} = \frac{2}{3} \delta_{ij} \left(\rho \varepsilon + Y_M \right) \tag{2.41}$$

where the scalar dissipation rate, ϵ , is computed the same way as it is for the standard k- ϵ model.

In the Reynolds Stress Model, the turbulent viscosity and heat/mass transfer are modeled similarly to the standard k-ε model.

2.4 Near Wall Treatment

The presence of walls significantly affects turbulent flows, and is obviously of interest for the study of wall jets. First of all, as with laminar flows, the velocity field is affected by the no-slip condition at the wall surface. Meanwhile, from the standpoint of turbulence, the flow is also affected in non-trivial ways due to the existence of the wall. In the region very close to the wall, viscous damping reduces tangential velocity fluctuations, and the kinematic blocking reduces the normal fluctuations. Farther away from the wall surface in the near-wall region, however, the turbulence is rapidly augmented by the production of turbulent kinetic energy due to the large gradients in mean velocity [12].

It is in the near wall region that flow variables undergo drastic changes, and the transport of momentum and other scalars is most vigorous. Walls are also the main source of turbulence. Therefore, the near-wall modeling is critical for the numerical simulations. Good resolution in the near wall region determines the success of the wall-bounded turbulent flow predictions.

The turbulence models introduced in Chapter 2 are primarily valid for turbulent core flows (the flow in the regions somewhat far from walls). Therefore, near wall treatment is necessary to make these models work for wall-bounded flows as well.

2.4.1 The Turbulence Boundary Layer and the Law of the Wall

Experiments show that the turbulence boundary layer can be subdivided into two zones, namely, the inner region and the outer region as shown in Figure 6.

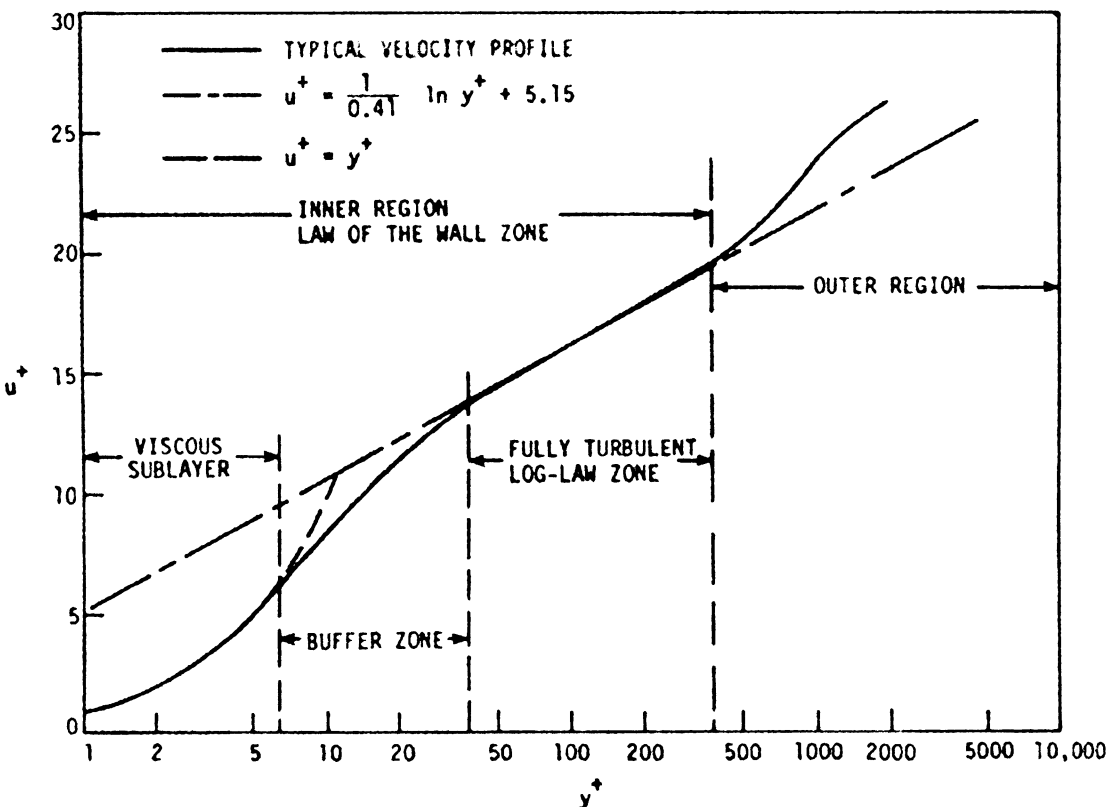


Figure 6. Zones in the turbulence boundary layer (reproduced from [13])

The boundary layer equation can be written as [17]

$$\overline{u}\frac{\partial \overline{u}}{\partial x} + \overline{v}\frac{\partial \overline{u}}{\partial y} = -\frac{d\overline{P}}{dx} + \frac{1}{\rho}\frac{\partial}{\partial y} \left[\mu \frac{\partial \overline{u}}{\partial y} - \rho \overline{u'v'}\right]$$
 (2.42)

Since the size of u' fluctuation corresponding to v' appears to depend on the steepness of the average \overline{u} profile [17], the notation of eddy shear stress makes sense:

$$-\rho \overline{u'v'} = \rho \varepsilon_{\mathsf{M}} \, \frac{\partial \overline{u}}{\partial y} \tag{2.43}$$

where the empirical function ϵ_M is called momentum eddy diffusivity. Or, to keep the consistency with the turbulent viscosity, it also has the meaning of kinetic viscosity due to turbulence, and can be written as v_t . Thus, in equation (2.42), the molecular diffusion shear stress $\mu \frac{\partial \overline{u}}{\partial y}$ is augmented by the time-averaged eddy shear stress $-\rho \overline{u'v'}$. The apparent shear stress τ_{app} , therefore, can be given as

$$\tau_{app} = \mu \frac{\partial \overline{u}}{\partial y} - \rho \overline{u'v'} = \rho (v + \varepsilon_{M}) \frac{\partial \overline{u}}{\partial y}$$
 (2.44)

Note that ε_M is a flow parameter, not a fluid property.

Substituting (2.43) into the boundary layer equation (2.42) yields

$$\overline{u}\frac{\partial \overline{u}}{\partial x} + \overline{v}\frac{\partial \overline{u}}{\partial y} = -\frac{1}{\rho}\frac{d\overline{P}}{dx} + \frac{\partial}{\partial y}\left[\left(v + \varepsilon_{M}\right)\frac{\partial \overline{u}}{\partial y}\right]$$
 (2.45)

There exits a region close enough to the wall that the left-hand side of equation (2.45) is sufficiently small, while the longitudinal pressure gradient $\frac{d\overline{P}}{dx}$ is zero as in the case of uniform flow parallel to a flat plate. This region is also characterized by an apparent shear stress that does not vary with y:

$$\left(v + \varepsilon_{M}\right) \frac{\partial \overline{u}}{\partial v} = \frac{\tau_{0}}{\rho} \tag{2.46}$$

in which τ_0 is the actual shear stress at the wall surface, that is, the apparent shear stress, τ_{app} , at y = 0 where the Reynolds stress $-\rho \overline{u'v'}$ vanishes. The

constant apparent shear stress assumption in equation (2.46) defines the inner region in Figure 6.

To nondimensionalize equation (2.45) in the inner region, the so-called friction velocity was introduced in the turbulence literature:

$$u_{r} = \left(\frac{\tau_{0}}{\rho}\right)^{1/2} \tag{2.47}$$

With the following nondimensionalization know as the wall coordinates

$$u^{+} = \frac{\overline{u}}{u_{r}}, \qquad v^{+} = \frac{\overline{v}}{u_{r}}$$

$$x^{+} = \frac{xu_{r}}{v}, \qquad y^{+} = \frac{yu_{r}}{v}$$
(2.48)

and the constant τ_{app} assumption (2.46), equation (2.45) can be written as

$$\left(1 + \frac{\varepsilon_M}{v}\right) \frac{\partial u^+}{\partial y^+} = 1 \tag{2.49}$$

which determines the velocity distribution in the inner region.

With equation (2.49), the inner region can be further subdivided into three sublayers according to the relationship between the momentum eddy diffusivity ϵ_{M} (v_{t}) and v as shown in Figure 6:

- (1) The viscous sublayer, where $v \gg \epsilon_M$.
- (2) The buffer zone, where ν and ϵ_M are of the same order of magnitude.
- (3) The fully turbulent sublayer (or the log-law zone), where $\epsilon_{\text{M}} >> \nu$.

In the viscous sublayer, the flow is almost laminar-like. Dropping the term v/ϵ_M in equation (2.49), we learn that velocity has a linear profile:

$$u^+ = y^+ \tag{2.50}$$

In the fully turbulent sublayer, the effects of turbulence are dominant. The equation (2.49) reduces to

$$\frac{\varepsilon_M}{v} \frac{\partial u^+}{\partial v^+} = 1 \tag{2.51}$$

and the velocity profile takes the form [17]

$$u^{+} = A \ln y^{+} + B \tag{2.52}$$

where A and B are two empirical constants. Equation (2.52) is known as the law of the wall, which is valid in the log-law zone in Figure 6.

2.4.2 Near Wall Modeling in FLUENT

There are two approaches available in FLUENT to model the near wall region: the wall functions and the two-layer zonal model.

Wall Functions

In this approach, the viscous-affected inner region (the viscous sublayer and buffer zone in Figure 6) is not resolved. Instead, the semi-empirical formulas called "wall functions" are adopted to "bridge" the inner region between the wall and the fully turbulent sublayer.

First, the wall units u and y were introduced:

$$u^* = \frac{C_{\mu}^{1/4} k^{1/2} \overline{u}}{\tau_0 / \rho}, \qquad y^* = \frac{\rho C_{\mu}^{1/4} k^{1/2} y}{\mu}$$
 (2.53)

where k is the turbulent kinetic energy.

When y < 11.225, FLUENT applies the laminar stress-strain relationship for the velocity profile:

$$u^* = y^* \tag{2.54}$$

When y' > 11.225, the law of the wall is employed as

$$u^* = \frac{1}{\kappa} \ln(Ey^*) \tag{2.55}$$

where κ is the von Karman's constant (= 0.42), E (= 9.81)is an empirical constant. (The logarithmic law for mean velocity (2.55) is known to be valid for $y^* > 30 \sim 60$.) It is worth noting that the law of the wall employed in FLUENT (2.55) is based on the wall units y^* and u^* rather than the wall coordinates y^* and u^* .

The Reynolds' analogy between momentum and energy transport gives a similar logarithmic law for mean temperature [12].

If the wall function approach is chosen in k- ϵ models or RSM, the k equation is solved in the entire domain with the boundary condition

$$\frac{\partial k}{\partial n} = 0 \tag{2.56}$$

imposed at the wall surface, where n is the local coordinate normal to the wall.

In the wall-adjacent cells, the production of kinetic energy, G_k , is computed from [12]

$$G_{k} \approx \tau_{0} \frac{\partial \overline{u}}{\partial y} = \tau_{0} \frac{\tau_{0}}{\kappa \rho C_{u}^{\frac{1}{4}} k^{\frac{1}{2}} y}$$
 (2.57)

And instead of solving the ε equation, ε is computed from

$$\varepsilon = \frac{C_{\mu}^{\frac{3}{4}} k^{\frac{3}{2}}}{\kappa v} \tag{2.58}$$

in the wall-adjacent cells [12].

The wall function approach gives acceptable predictions for most wall-bounded flows with high Reynolds number. However, it is inadequate for low Reynolds number flows or when near wall effects are pervasive, in which the underlying hypotheses for the wall functions cease to be valid (e.g., flow though a small gap as is the case for the present study).

Two-Layer Zonal Model

In this approach, the turbulence models are modified in order to resolve the viscosity-affected region all the way to the viscous sublayer. The entire domain is subdivided into two regions: the viscosity-affected region and the fully-turbulent region. The demarcation of the two regions is determined by the so-called turbulent Reynolds number, Rey, based on the wall-distance. The definition of the turbulent Reynolds number is

$$Re_{y} = \frac{\rho\sqrt{k}y}{\mu}$$
 (2.59)

where y is the normal distance from the wall at the cell centers.

In the viscosity-affected region where Re $_{\rm y}$ < 200, a one-equation model is employed [12]. The same momentum and k equations described earlier are solved. However, the ϵ field is computed from

$$\varepsilon = \frac{k^{3/2}}{l_{\varepsilon}} \tag{2.60}$$

and the turbulent viscosity, μ_t , is computed by

$$\mu_{l} = \rho C_{u} \sqrt{k} l_{\mu} \tag{2.61}$$

where the length scale formulas are given as

$$l_{\varepsilon} = c_{l} y \left[1 - \exp \left(-\frac{\operatorname{Re}_{y}}{A_{\varepsilon}} \right) \right]$$
 (2.62)

$$l_{\mu} = c_{l} y \left[1 - \exp \left(-\frac{\operatorname{Re}_{y}}{A_{\mu}} \right) \right]$$
 (2.63)

The constants in the above equations are

$$c_1 = \kappa C_u^{-3/4}, \quad A_s = 2c_1, \quad A_u = 70$$
 (2.64)

In the fully turbulent region where Re $_{y}$ > 200, the k- ϵ models and RSM are turned on.

Since the near wall effects are considered crucial for the present study, the two-layer-zonal model is believed to be more suitable for the near treatment compared to the wall function approach.

2.5 Summary

FLUENT provides comprehensive models in single-phase, single-species simulations. No existing multi-phase model, however, was found suitable to capture the condensation/evaporation phenomenon in the present study.

Nevertheless, in FLUENT certain portions of the solver are open to the users by User-Defined source terms in the governing equations. It is one of the efforts of the current study to model the phase change effect by implementation of appropriate User Defined Functions (UDF's).

Chapter 3

SIMULATION WITHOUT PHASE CHANGE

This chapter is focused on the velocity and temperature simulations without phase change, the so-called "dry air" condition, which happens when the temperature is higher than the dew point of water vapor everywhere in the computational domain. Simulation results are compared with experimental and published data.

3.1 Solution Procedure

The basic steps to take in order to solve a problem with FLUENT are given as the following:

- Create model geometry and grid with the pre-processor Gambit
- Choose appropriate solver for 2D or 3D modeling when starting the solver
 FLUENT 5
- Import the grid into the solver
- Select the solver formulation: steady or unsteady, explicit or implicit, etc.
- Choose the basic equations to be solved, and additional models need: i.e.
 multi-species
- Specify material properties
- Impose boundary conditions
- Adjust the solution control parameters

- Initialize the flow field
- Calculate a solution
- Save and examine the results
- If necessary, refine the grid or consider revisions to the numerical or physical model

The geometry and mesh generation can be completed by the preprocessor Gambit. The mesh file is then imported into the solver (FLUENT 5 is
actually the solver and post-processor.). The solver also accepts I-DEAS
universal files, NASTRAN files, PATRAN neutral files, and ANSYS prep7 files.
FLUENT also has a fairly strong post-processing function to analyze and
examine the computation results.

3.1.1 Pre-processing

Strictly speaking, the experimental facility is not really a 2D platform. The inlet and outlet are not of the same length in the z direction of Figure 1, and neither of them goes across all the way through the z direction of the facility.

However, since the measurements are taken mainly at the center portion of the z direction of the facility, it is believed that the third direction effect is not significant, and the whole geometry can be treated as a 2D model in the x, y plane.

As mentioned in Chapter 1, the curvature of the contraction is a special design with the aim that the velocity profile distributes evenly along the y direction at the jet nozzle after the flow passes through the contraction [1]. This curve is difficult to create directly with the pre-processor. Therefore, the geometry

of the computation was imported into Gambit as an IGES file created by AutoCAD as shown in Figure 7.

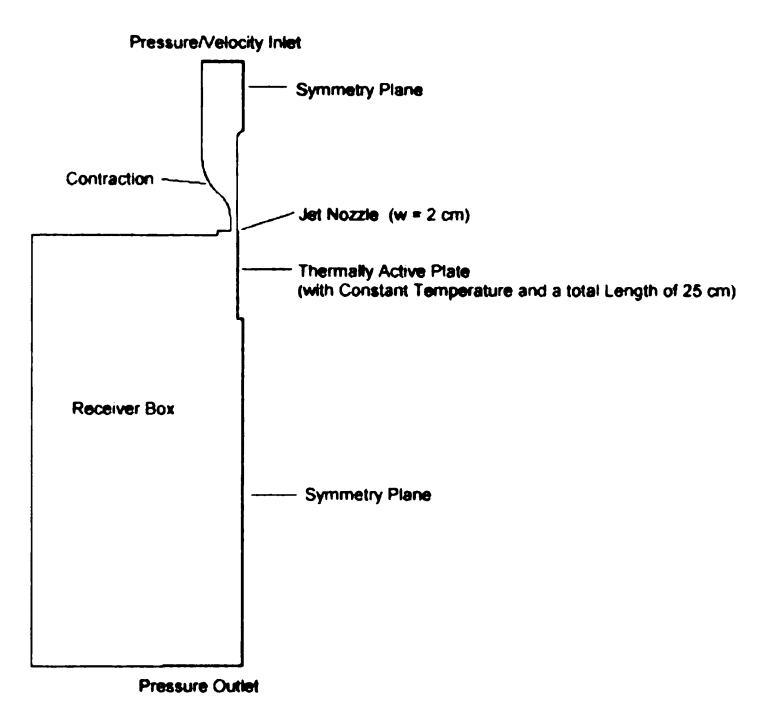


Figure 7. Geometry and Boundary Types of the Simulation

Note that the symmetry of the geometry is taken into account to reduce the computational effort.

The mesh was generated with Gambit with quadrilateral cells. It is well structured and highly clustered in the thermally active test section (see Figure 1), especially in the region near the thermally active plate (See details in the near wall treatment section). The mesh file was then imported into the solver.

3.1.2 Model Control

Solver: Segregated (Governing equations are solved sequentially. i.e.,
 segregated from one another. Because the governing equations are non-

linear (and coupled), several iterations of the solution loop must be performed before a converged solution is obtained [12].)

Formulation: Implicit

Space: 2D

Time: Steady

Energy: Enabled for non-isothermal simulation

Viscous (Turbulence Model): k-ε or RSM

3.1.3 Near Wall Treatment

As was discussed in Chapter 2, given the limitations of the wall function approach and specific needs of the near wall resolution, the two-layer-zonal model is adopted as the near wall treatment for the current study.

3.1.4 Unit System

Internally, FLUENT stores all the parameters and performs all the calculations in SI units. Nevertheless, one can work with different unit systems, even inconsistent units because a correct set of conversion factors is built in the solver, which converts the units one wants to use into the standard SI unit system. The restriction is that boundary profiles, source terms, custom field functions, and user-defined functions must be in the SI units.

The length unit of the AutoCAD design was in inches, and was converted into meters before the calculation. This is for the sake of consistency since all the other parameters work in the SI system.

43

3.1.5 Material Properties

Because no phase change effect is taken into account at the current stage, the fluid is considered as "dry air". The default physical properties of air stored in the FLUENT database (listed in Table 1) were employed.

Table 1. Default Values of Physical Properties of Air in FLUENT

Density ρ	1.225 (kg/m³)
Specific Heat C _p	1006.43 (J/kg-K)
Thermal Conductivity k	0.0242 (W/m-K)
Viscosity μ	1.7894e-05 (kg/m-K)
Molecular Weight	28.966 (kg/kmol)

Also, since the experimental data were measured mostly in the range of common room temperature, it is assumed that physical properties of air do not vary significantly with temperature. It is assumed that all the physical properties are constants and the air is incompressible. This assumption makes the energy equation uncoupled from the continuity and momentum equations. Therefore, it is not necessary to solve the flow equations (continuity, momentum and turbulence) and the energy equation simultaneously. Instead, the temperature field can be calculated based upon simulation of the velocity field (the solution of the flow equations).

3.1.6 Operating Conditions

Operating pressure, p_{op} , is important for incompressible ideal gas flows because it directly determines the density: the incompressible ideal gas law computes density as

$$\rho = \frac{p_{op}}{RT}$$

As for compressible flows,

$$\rho = \frac{p_{op} + p}{RT}$$

where p is the gauge pressure, R is the universal gas constant, and T is the temperature in Kelvin.

The operating pressure for the current simulation is set to be 101325 Pa (1atm). The reference pressure location (where the gauge pressure is always zero) can also be specified. But when pressure boundaries are involved, the reference pressure location is ignored since it is no longer needed [12].

FLUENT uses gauge pressure in calculation. When absolute pressure, p_{abs}, in needed, it is obtained by

$$p_{abs} = p_{op} + p$$

3.1.7 Boundary Conditions

As mentioned earlier, the driving force for the system in Figure 6 is the pressure differential between the inlet and outlet. Pressure inlet and outlet boundary conditions are supposed to be imposed for them. However, it was

found that the simulation results were almost the same when the boundary condition at the inlet was specified as a velocity condition with a constant value.

The thermal boundary conditions that need to be specified are the temperature at the inlet, backflow temperature at the pressure outlet (backflow is predicted numerically at the pressure outlet as seen in Figure 12), and the constant temperature on the surface of the thermally active plate.

FLUENT defaults the boundary condition to be adiabatic wall, where the heat flux equals zero and all the velocity components are zeros. So apart from the two symmetry planes in Figure 6, the only boundary conditions needed for the simulation are:

Inlet:

Total gauge pressure: 0 Pa; or constant velocity: 1.6896 m/s
 (according to the experimental measurement)

Note that the Bernoulli's equation $\frac{p_t = p_s + \frac{1}{2} |V|^2}{\text{holds at the pressure}}$ inlet boundary condition for incompressible flows, where p_t is the total pressure; p_s is the static pressure; and |V| is the velocity magnitude.

- Turbulence intensity: 2.5% (as was measured in experiment);
 Hydraulic diameter: 0.284 m (calculated from the real geometry).
- Total temperature: ~ 298.15 K (room temperature)

Total temperature is the temperature at the thermodynamic state that would exist if the fluid were brought to zero velocity. Static temperature is the temperature that is measured moving with the fluid. For incompressible flows, the total temperature is equal to the static temperature.

Outlet:

Gauge pressure: -60 Pa

Backflow turbulence intensity: ~30% (estimated)

Backflow hydraulic diameter: 0.42 m

The value of backflow turbulence intensity is not known from experimental measurement. Nevertheless, it was found from calculations that the simulation results in the thermally active section are not sensitive to this value since this region is far away from the pressure outlet.

Backflow total temperature: same as the temperature of the inlet

Thermally Active Plate:

Wall boundary with a constant temperature: ~ 278.15 K (adjustable)

It is worth noting that, from the standpoint of comparison, it is the types of boundary conditions that are of importance, but not the magnitudes. Since the simulation results are usually normalized before they compared to other data, many input values for the boundary conditions do not effect the results very much after normalization.

3.1.8 Solution Control

The segregated solver makes it possible to solve the governing equations separately. Since the physical properties are assumed to be constants as was discussed in the section of material properties, the following strategy was taken in order to save some running time.

- Perform velocity simulation by selecting flow equations and while keeping the energy equation deselected
- Perform temperature simulation by turning on the energy equation and deselecting the flow equations after the velocity solution converged

The default under-relaxation factors are kept for the k-ε model. However, it was found difficult to get converged solutions with the Reynolds stress model (RSM). Therefore, more conservative under-relaxation factors are employed for RSM.

Most of the simulations are performed with the first order upwind discretization since no major improvement was achieved with the second order discretization when the velocity data in the wall jet region are compared to the experimental data.

3.1.9 Convergence Judgement

There is no universal method for judging convergence. The residual definitions are employed in FLUENT. The residual of a general variable computed by FLUENT's segregated solver is the imbalance of the variable summed over all the computational cells. It is scaled using a scaling factor representative of the flow rate of the variable through the domain since it is difficult to judge convergence by examining the non-scaled residuals. The solution is considered converged when the scaled residuals go below a certain set of default values that can be changed by the user. The computation will be

stopped when the residuals of the governing equations are less than the corresponding default values.

It was found that the default values of FLUENT for the convergence criterion are not satisfactory in terms of experimental verification. The convergence judgement employed here was not by the value of the residuals themselves, but by their behavior. It was ensured that the residuals continue to decrease (or remain low) for several iterations (say 50 or more) before concluding that the solution has converged.

3.2 Results and Discussions of the Isothermal Simulation

The simulation without phase change is first performed for an isothermal condition, which means that the temperature on the plate temperature equals that of the jet (inlet room temperature). The velocity field and turbulence variables tested from the experimental facility and some other published data are utilized for comparison with the numerical simulation.

The velocity distribution of the flow field is of great interest in the wall jet study. The data in the downstream self-similar region appear to be more interesting to most researchers as introduced in Chapter 1. For the study of the defogger flow, however, more attention needs to be paid in the developing region since on the interior windshield surface of a vehicle it is in the developing region that the defogging effects need to be applied.

The experimental facility (depicted in Figure 7) to be simulated has a jet nozzle with a slot width of 2 cm, and the thermally active plate spans 25 cm

along the streamwise direction of the jet. Six streamwise locations (x/w = 0, 1.59, 3.18, 4.45, 7.62 and 10.8) were chosen to plot velocity profiles from the simulation in order to compare with the experimental measurements. Figure 8 shows the development of the velocity profile simulated by the realizable k- ϵ model. A plot of over-lapped velocity profiles at the six tested locations is given in Figure 9. The abscissa of the plot represents the y distance from the plate (surface of the wall). The ordinate is the magnitude of velocity.

Some visualization of the simulation results is provided to give some basic impressions of the flow field. Figure 10 and Figure 11 are the contour of velocity magnitude and the static pressure, respectively. Figure 12 shows the visualization of velocity vectors in different regions of the flow. Figure 13 depicts the viscosity-affected sublayer at various locations for the two-layer-zonal model for the near wall treatment, where the turbulent Reynolds number, Re_y, is less than 200.

3.2.1 Velocity Profiles

Data in the Outer Scaling

As in most wall jet literature, the velocity profiles were first normalized with outer scaling. That is, the velocity magnitude is normalized by the maximum value of the profile, and the y distance is normalized by δ_2 described in Chapter 1. The numerical simulation was performed with the standard k- ϵ (ske in the Figures) models, the realizable k- ϵ (rke in the Figures), and the Reynolds stress

model (rsm in the Figures). The comparison between the CFD simulation and the experimental data is given by Figure 14 through 19.

It can be observed that the velocity profile predictions of realizable $k-\epsilon$ model and RSM are very similar. According to the test data, they both give a better velocity prediction at the jet nozzle (x/w = 0) and the region close to the nozzle (x/w = 1.59) compared to the standard $k-\epsilon$ model. This means that the realizable $k-\epsilon$ model and RSM better simulate the effect of the upstream contraction. As mentioned earlier, the design purpose of the contraction is to provide an evenly distributed velocity profile at the jet nozzle. This is proved by the experimental measurement at x/w = 0. The standard $k-\epsilon$ model appears to over-predict the friction effect of the curved surface of the contraction so that the velocity magnitude close to the side of the curved surface is smaller than that measured.

On the other hand, however, the standard k- ϵ model gives better predictions as the jet develops along the wall. Especially, for the location where the velocity profile takes the maximum value (y_m in Figure 2), the standard k- ϵ model gives much better predictions than the other two models. This can be explained by the fact that the standard k- ϵ model was originally developed from experiments with air and water for fundamental turbulent shear flows [12]. The empirical model constants of the standard k- ϵ model have been found to be appropriate for plane jets and plane shear layers [17] and a wide range of wall-bounded and free shear flows [12].

The comparison of the development of velocity profiles suggests that the realizable k-ε model and RSM appear to under-predict the diffusion of the turbulence dominated core (free shear layer) as the jet develops along the wall surface. This can be clearly seen from the development of the turbulent viscosity ratio, μ/μ, predicted by the two different models, as shown in Figure 20 and Figure 21. The profile of the ratio of turbulent viscosity to molecular viscosity suggests the development of turbulence. From Figure 20 and 21, it is observed that the standard k-ε model predicts a higher value for the turbulent viscosity at turbulence-dominated core compared to the other two models. This may result in different predictions of the mass transfer according to equation (2.11).

Data in Inner Scaling

The wall coordinates (2.48) scheme introduced in Chapter 2 is also referred to as the inner scaling. Figure 22 shows the velocity comparison of the CFD simulation to experimental data at the initial stage (x/w = 1.59) and the relatively well developed one (x/w = 10.8) with inner scaling.

Wygnanski et al [5] argued that, in the well-developed region far away from the jet nozzle, the constant A in the log-law

$$u^{+} = A\log(y^{+}) + B \tag{3.1}$$

does not vary with the jet Reynolds number Re_w, while B does. Their measurements showed that A always equals 5.5, while B varies between 4.9 to 9.2 as Re_w goes from 3700 to 19300. Given the jet Reynolds number of the

present study (13000 as given in section 2.3), B can be linearly interpolated as a very rough approximation. Thus, equation (3.1) can be written as [18]

$$u^{+} = 5.5\log(y^{+}) + 8.83 \tag{3.2}$$

The plot of this equation is also given in Figure 22 as a reference.

Worth mentioning is that the simulation data of u^+ in Figure 22 is strictly according to the wall coordinates definition (2.48). But the u^+ in the experimental data is actually the velocity magnitude ($U = \sqrt{u^2 + v^2}$) divided by the friction velocity (u_τ) since the technique employed in the measurements in not capable of detecting the individual velocity components (u, v). Although v is considered negligible compared to u (which makes $U \cong u$), the difference between U and u may still account for the discrepancy between the numerical and experimental data in Figure 22.

Figure 23 compares the inner-scaled distribution of u^+ predicted by the standard k- ϵ model to the published data by Eriksson et al [7]. For reference, the overall inner-scaled predictions by the standard k- ϵ model are given in Figure 24.

The experimental data of the u⁺ distributions of Eriksson et al [7] and Hoke et al [18] are quite different in the region close to the jet nozzle. Nevertheless, in the region farther away from the nozzle, the data by Hoke et al [18] appear to agree with the equation (3.1) by Wygnanski et al [5] (x/w = 10.8 in Figure 22). The CFD simulations appear to match well with the experimental data by Eriksson et al [7] (x/w = 10 in Figure 23).

The above comparisons suggest that the wall jet can be considered relatively well-developed farther away from the nozzle when the inner-scaled

data tend to become self-similar. In the near-nozzle region, however, the wall jet is still in the developing state, the inner-scaled data are dependent on the upstream geometry situations for different experimental conditions.

Since the same near wall approach (two-layer zonal model) was adopted for all the three different turbulence models, it is not surprising to see that the predictions of three different turbulence models do not differ from each other very much in inner scaling (Figure 22). All the CFD predictions give lower values of u⁺ compared to the experimental data by Hoke et al.

In the relatively well-developed region (x/w = 10 in Figure 23), the predictions match with the data of Eriksson et al fairly well, especially when y^+ < 100. That is, the two-layer zonal model gives better predictions in the well-developed region of the wall jet.

In fact, the numerical simulations give similar predictions of u⁺ in both the near-nozzle developing region and the relatively well-developed region for y⁺ less than 100 as shown in Figure 24. This suggests that the two-layer zonal model tends to predict the distribution of u⁺ in both regions as if the wall jet is well-developed. The similar predictions can be found in the predictions of the other two turbulence models. The compiled Realizable k-ε (rke) and Reynolds Stress Model (RSM) predictions of the inner-scaled velocity profiles are given in Figure 25.

3.2.2 Turbulence Fluctuations

Data in Outer Scaling

In experimental studies, the so-called Streamwise Normal Stress (SNS) is used to account for the velocity fluctuation due to turbulence. It is defined as

$$SNS = 100 \frac{\overline{u'}^2}{U_{\text{max}}^2}$$
 (3.3)

where $\overline{u'}$ is the fluctuation of the velocity, and U_{max} is the local maximum velocity of the velocity profile at the location x/w.

In the numerical simulations, the fluctuations are assumed to be isotropic in the k- ε models. The magnitude of $\overline{u'}$ can be obtained by using equation (2.19) and setting the reference velocity to be 1 (m/s). For comparison, $\overline{u'}$ is obtained the same way in the Reynolds stress model. Comparisons at the developing region (x/w =1.59) and developed region (x/w =10.8) are plotted in Figure 26.

As can be observed, by using equation (2.19) to get the fluctuations, none of the models provides satisfactory agreement with the experimental data. The standard k-ε model gives worse predictions in the developing region than the other two models.

It is worth noting, nevertheless, the individual stress components ($\overline{u'u'}$, $\overline{v'v'}$, $\overline{u'v'}$ and $\overline{w'w'}$ for 2D flows) can be obtained by the Reynolds stress model (RSM). So the SNS can be obtained directly by the $\overline{u'u'}$ stress in RSM instead of using equation (2.19) for $\overline{u'}$.

Figure 27 shows that the SNS calculated directly from the $\overline{u'u'}$ stress from the RSM matches the experimental data much better than the ones predicted by the isotropic k- ϵ models (see Figure 26).

For reference, the compiled simulations of outer-scaled SNS are included in Appendix A.

Data in Inner Scaling

In the inner scaling, the velocity fluctuation is non-dimensionalized as

$$u^{\prime +} = \frac{\sqrt{\overline{u^{\prime 2}}}}{u_r} \tag{3.4}$$

where u_t is the friction velocity defined in equation (2.47).

Figure 28 shows the inner-scaled comparison of predicted u^{**} distributions and experimental data (Exp in figure) in the developing region (x/w = 1.59) and the developed region (x/w = 10.8). The fluctuation boundary conditions at the pressure inlet are the same for all three turbulence models: turbulence intensity equals 2.5%. The u^{**} distribution by the Reynolds stress model (uu_rsm in figure) was calculated directly from the $\overline{u'u'}$ stress.

None of the models produce predictions that are in very good agreement with the experimental data. The agreement between the standard k- ϵ model (ske in figure 26) predictions and the experimental data is especially poor in the developing region. In contrast to the inner scaled comparison of mean velocity, the experimental data are not consistently larger than the predictions at x/w = 1.59. Thus, it is difficult to explain this solely on the basis of the experimental difficulty in calculating the friction velocity u_{τ} (or the surface shear stress τ_0).

Eriksson et al [7] obtained experimental data for $\overline{u'}$, $\overline{v'}$ and $\overline{u'}\overline{v'}$. Their data showed that the fluctuations appear to become self-similar when x/w is

larger than 40, which suggests that the fluctuations of the current study are developing in the entire length of the plate (x/w \le 12.5). Also, their upstream conditions are different from the present study. Since the fluctuations in the developing region are believed to be highly dependent upon the upstream conditions (especially the turbulence intensity as the boundary condition at the inlet), the value of the direct comparison between the current simulations and the published data is somewhat questionable. Figure 29, 30 and 31 are the comparison of the RSM simulation and Eriksson et al's measurement of $\overline{u'}$, $\overline{v'}$ and $\overline{u'v'}$, respectively. The available streamwise locations for the published data are x/w = 0, 5 and 10 for $\overline{u'}$ (Figure 29), and x/w = 5 and 10 for $\overline{v'}$ and $\overline{u'v'}$ (Figure 30 and 31).

For reference, the simulations of inner-scaled fluctuations with RSM are included in Appendix B.

3.3 Results and Discussions of the Non-Isothermal Simulation

The study of the heat transfer and temperature distribution in a wall jet is rarely found in the literature. It is very important, nevertheless, in terms of the defogger research because the temperature distribution directly affects the concentration distribution of water vapor, and in turn, influences the mass exchange of water on the interior surface of the windshield (the wall surface).

With the assumption of constant physical properties, the velocity simulation is independent of temperature field. However, the success of the temperature field simulation depends on how well the velocity field is predicted.

Data in Outer Scaling

In the outer scaling, the temperature is normalized as

$$T^{\bullet} = \frac{T - T_s}{T_{inter} - T_s} \tag{3.5}$$

where T is the local temperature; T_s is the temperature held constant on the wall surface; and T_{inlet} is the temperature at the inlet of the whole system, which is believed to equal the temperature in the main stream of the jet. For the present simulation, T_{inlet} = 297.15 K (24 °C), and T_s = 277.15 K (4 °C).

The three turbulence models, namely, the standard k- ε model (ske), the realizable k- ε model (rke), and the Reynolds Stress Model (rsm), predict virtually identical temperature profiles in the outer scaling, as can be seen in the x/w = 10.8 profile in Figure 32. Actually, the predictions of the three turbulence models differ the most at x/w =10.8. Even so, the difference is still difficult to detect. Also included in Figure 32 are the comparison of the experimental data and the standard k- ε prediction at x/w =1.59, and x/w = 4.45.

The temperature predictions have better agreement with the experimental data in the relatively well-developed region (x/w =10.8) compared to that in the developing region (x/w =4.45). This appears to be consistent with the velocity predictions shown in Figure 15: At x/w = 4.45, the experimental velocity profile has a larger gradient than the predicted one. And so is the case for the temperature profile at the same streamwise location in Figure 32.

For reference, the simulations of outer-scaled temperature profiles with the standard k- ϵ model are included in Appendix C.

Data in Inner Scaling

The energy equation of a flat plate turbulent boundary layer is given as [17]

$$\overline{u}\frac{\partial \overline{T}}{\partial x} + \overline{v}\frac{\partial \overline{T}}{\partial y} = \frac{\partial}{\partial y} \left[(\alpha + \varepsilon_H) \frac{\partial \overline{T}}{\partial y} \right]$$
 (3.6)

where α is the thermal diffusivity; and the empirical function ϵ_H is known as the thermal eddy diffusivity.

Analogous to the constant τ_{app} assumption made earlier in Chapter 2, it is assumed that the left hand side of equation (3.6) is negligible sufficiently close to the wall, and the apparent heat flux q''_{app} does not depend on y. Thus, equation (3.6) becomes

$$\left(\alpha + \varepsilon_H\right) \frac{\partial \overline{T}}{\partial y} = \left[\left(\alpha + \varepsilon_H\right) \frac{\partial \overline{T}}{\partial y} \right]_{y=0}$$
(3.7)

That is,

$$\left(\alpha + \varepsilon_H\right) \frac{\partial \overline{T}}{\partial \nu} = \frac{-q_0''}{\rho C_B} \tag{3.8}$$

Introducing the wall coordinates in (2.48), equation (3.8) becomes

$$\frac{\rho C_P u_r}{-q_0''} \frac{\partial}{\partial y^+} (\overline{T} - T_0) = \frac{1}{\alpha / \nu + \varepsilon_H / \nu}$$
(3.9)

Defining the temperature in wall coordinates as

$$T^{+}(x^{+}, y^{+}) = (T_{0} - \overline{T}) \frac{\rho C_{p} u_{r}}{q_{0}^{r}}$$
(3.10)

equation (3.9) becomes

$$T^{+} = \int_{0}^{v^{+}} \frac{dy^{+}}{1/\Pr\left(1/\Pr_{t}\right)\left(\varepsilon_{H}/\nu\right)}$$
(3.11)

where Pr is the turbulence Prandtl number, defined as

$$\Pr_{l} = \frac{\varepsilon_{M}}{\varepsilon_{H}} \tag{3.12}$$

Equation (3.12) says that the temperature profile in the constant q''_{app} region is governed by the Prandtl number, the turbulent Prandtl number, and, via the turbulence viscosity ratio ϵ_M/ν , the velocity distribution in the same region.

With similar assumptions and derivation for velocity in Chapter 2, the temperature profile can be obtained from (3.11) [17]:

$$T^{+} = \begin{cases} \Pr y^{+}, (y^{+} < y_{CSL}^{+}) \\ \Pr y_{CSL}^{+} + \frac{\Pr_{t}}{\kappa} \ln \frac{y^{+}}{y_{CSL}^{+}}, (y^{+} > y_{CSL}^{+}) \end{cases}$$
(3.13)

where y_{CSL}^+ is the dimensionless thickness of a conduction sublayer in which the molecular mechanism outweighs the eddy transport of heat [17]. Good agreement with temperature measurements can be achieved when the empirical constants take the following values [17]:

$$Pr_t \cong 0.9, \quad \kappa \cong 0.41, \quad y_{CSL}^+ \cong 13.2$$
 (3.14)

Note that equation (3.13) is valid only in the region where τ_{app} and q^{\bullet}_{0} are both constants.

As can be seen in equation (3.14), in the fully turbulent region where $q^{"}_{app}$ and τ_{app} are still constant, the temperature profile T^{+} is analytically the same as the law of the wall for the velocity profile.

The log-law form of the temperature profile in equation (3.13) for air (Pr = 0.7) is

$$T^{+} = 2.195 \ln y^{+} + 3.58 \tag{3.15}$$

if the empirical constants take the values in equation (3.14).

Figure 33 is the comparison of inner-scaled temperature profiles. The plot of equation (3.15) is also included in Figure 33 for reference. Note that the default value of Pr_t in FLUENT is 0.85 instead of 0.9 in equation (3.15).

Since the numerical prediction matches with the log-law form quantitatively, it is believed that the relatively poor agreement between the experimental and the numerical data is due to the difficulty in measuring the velocity and temperature close enough to the wall so that the shear stress and heat flux at the wall surface (needed in the wall coordinates calculation) can be calculated more accurately.

For reference, the simulation of the inner-scaled temperature profile is included in Appendix D. Also include is the heat transfer coefficient on the wall surface, defined in FLUENT as

$$h = \frac{q_0''}{T_0 - T_{ref}} \tag{3.16}$$

where T_0 is the temperature on the wall surface; T_{ref} is the reference temperature specified by the user as the inlet temperature (main stream temperature in the

jet). Note that q"₀ is positive when the direction of the heat flux is into the computational domain (fluid).

3.4 Summary

For the velocity simulation, the three turbulence models employed (standard k- ε , realizable k- ε , and Reynolds Stress model) give fair predictions for the velocity field compared to the experimental measurements with the two-layer zonal approach for the near wall treatment. The standard k- ε model gives better outer-scaled predictions in the relatively well-developed region far from the jet nozzle. The Reynolds stress model, on the other hand, gives better predictions for the turbulent fluctuations.

For the temperature simulation, the three turbulence models give virtually identical predictions. The simulation results are in fair agreement with experimental measurements in the outer scaling form, and appear to be reasonable compared to the inner-scaled analytical temperature distribution in the log-law form. The reason for the discrepancy between the simulation and the inner-scaled experimental measurements is yet to be found out.

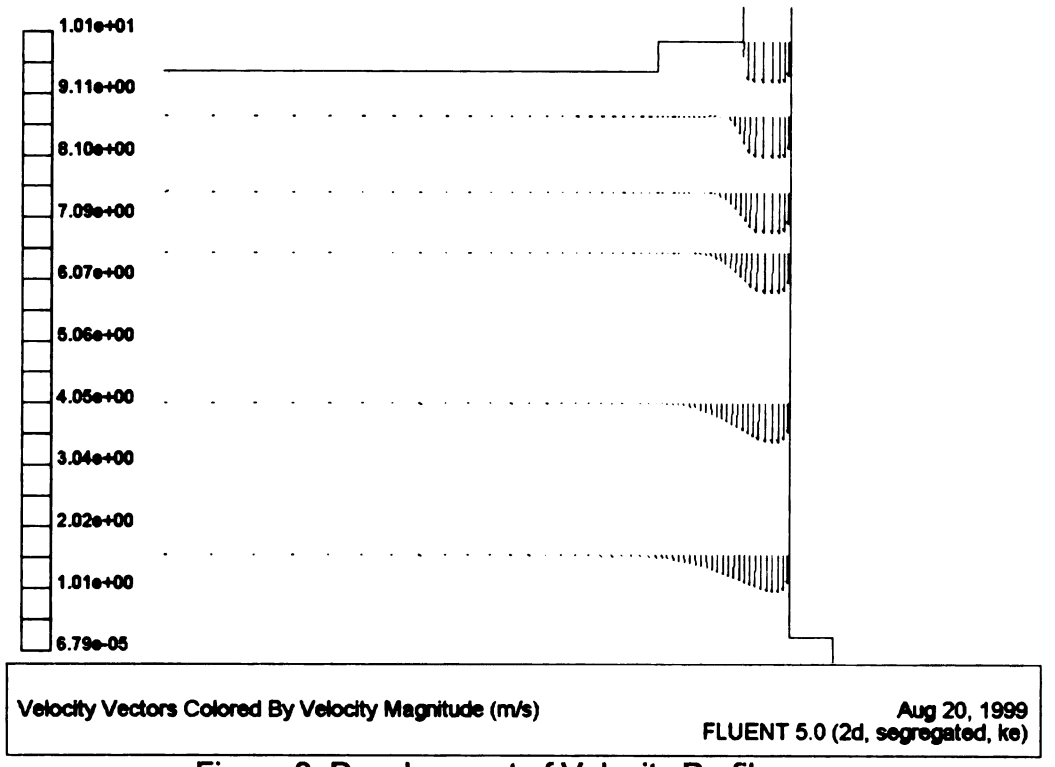


Figure 8. Development of Velocity Profile

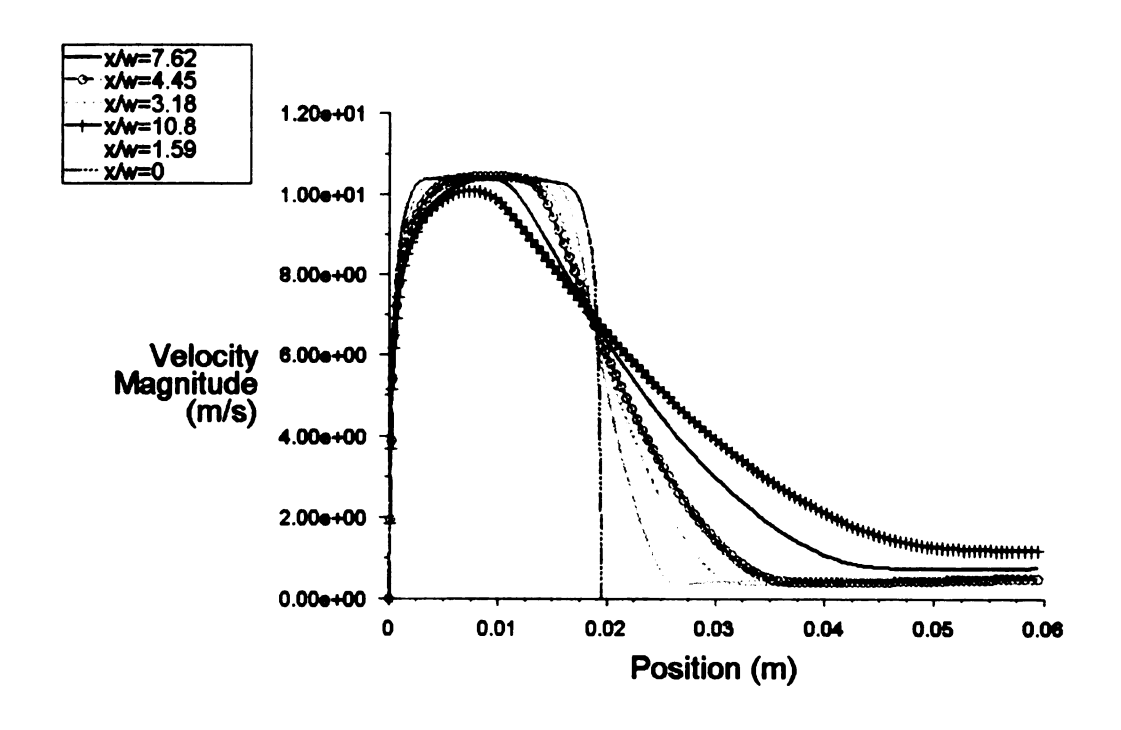
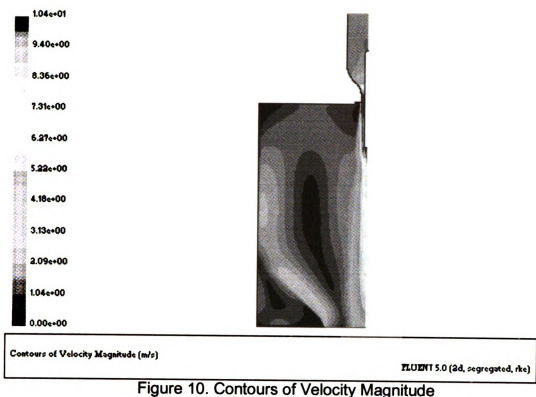




Figure 9. Plot of Velocity Magnitude



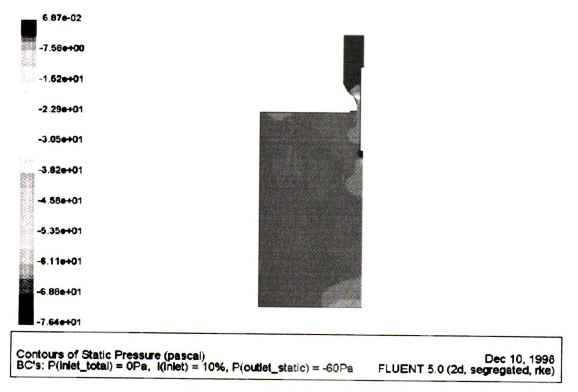


Figure 11. Contours of Static Pressure

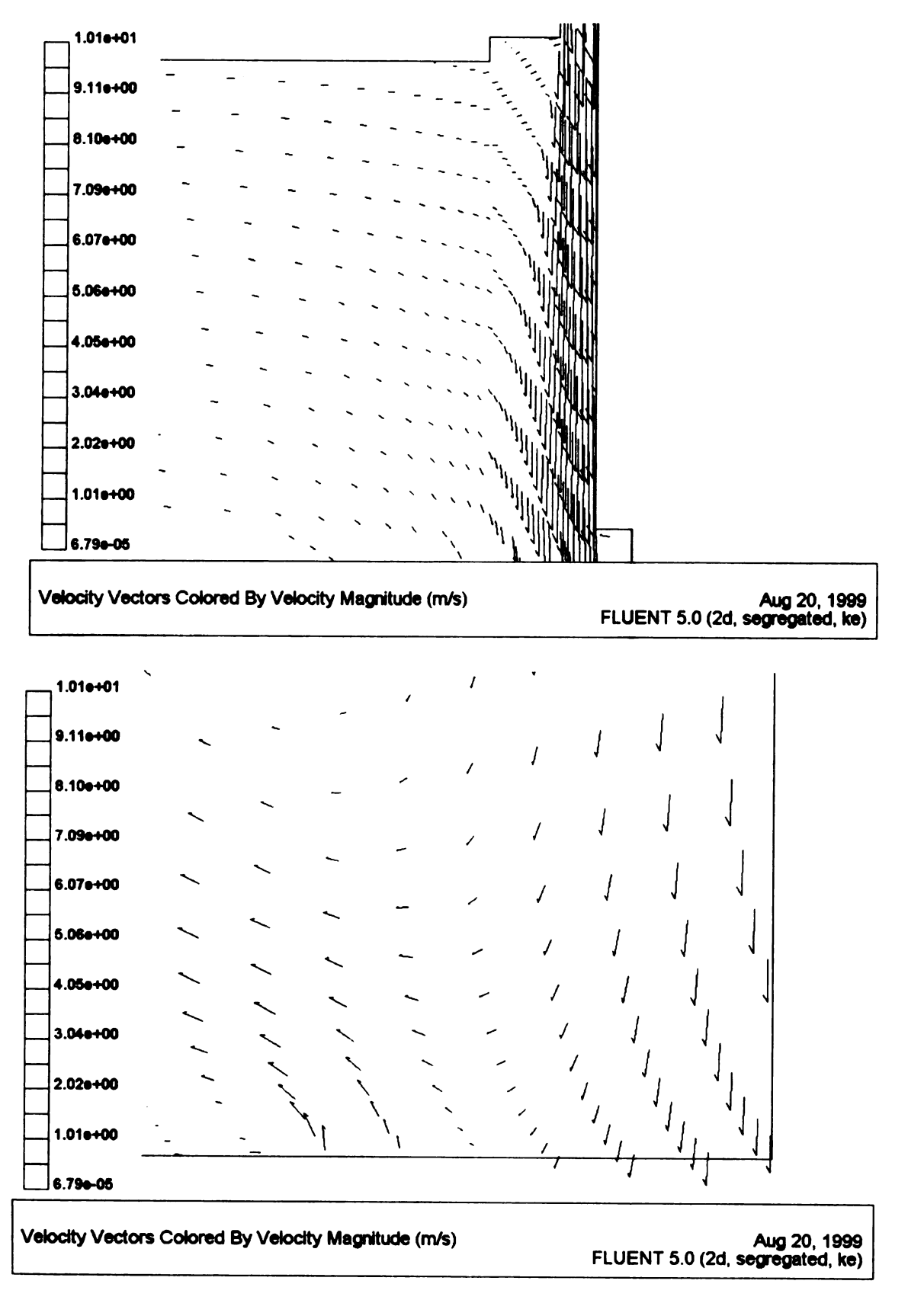


Figure 12. Visulization of Velocity Vectors

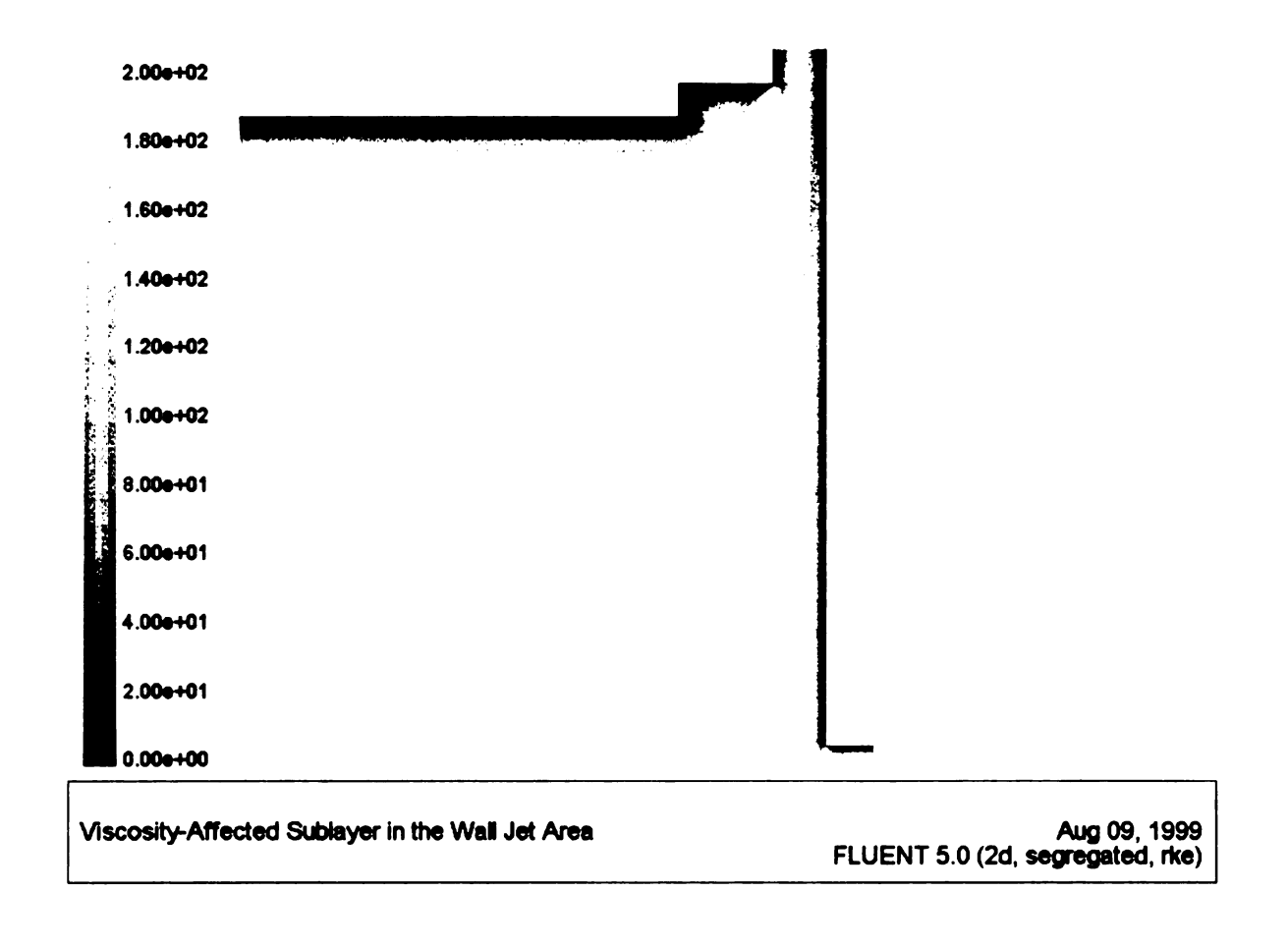
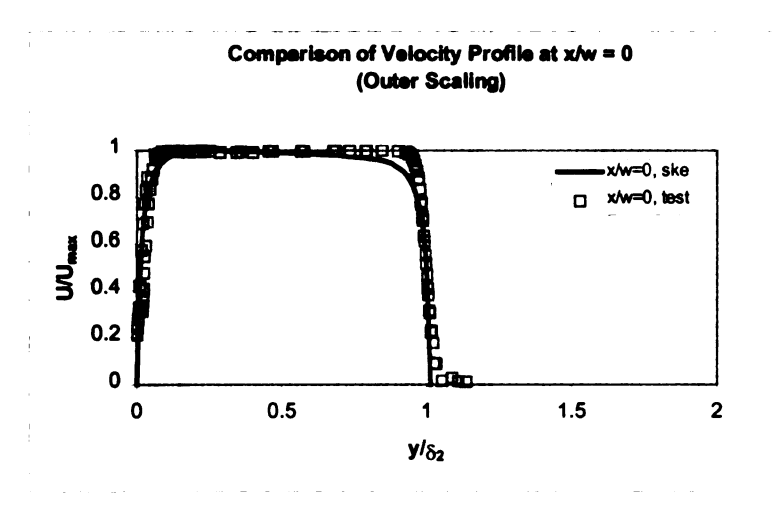
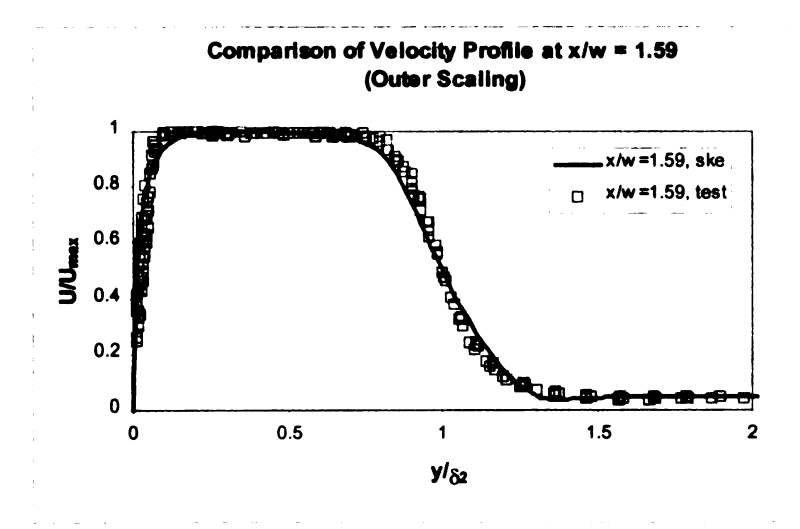


Figure 13. Viscosity-Affected Sublayer (Re_y<200)





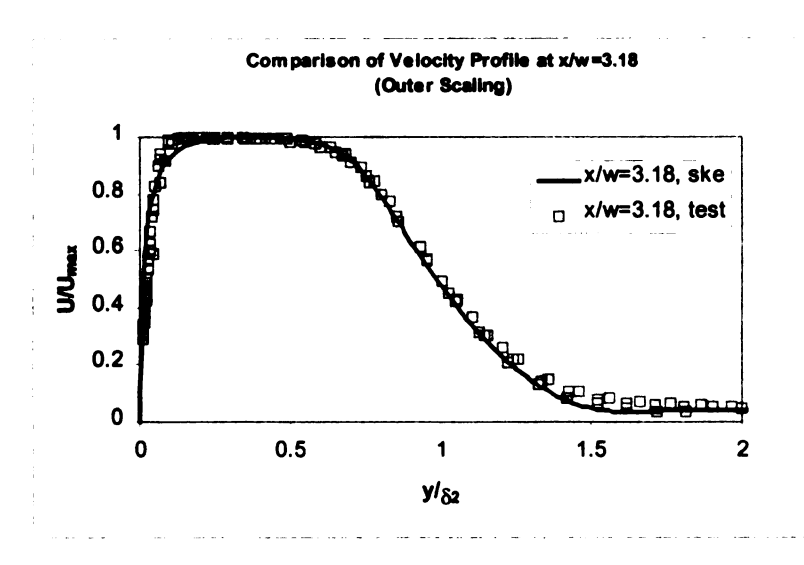
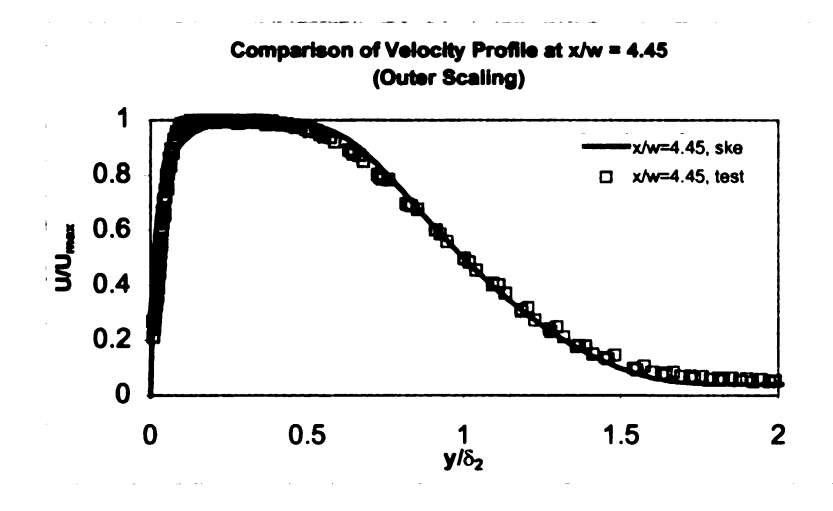
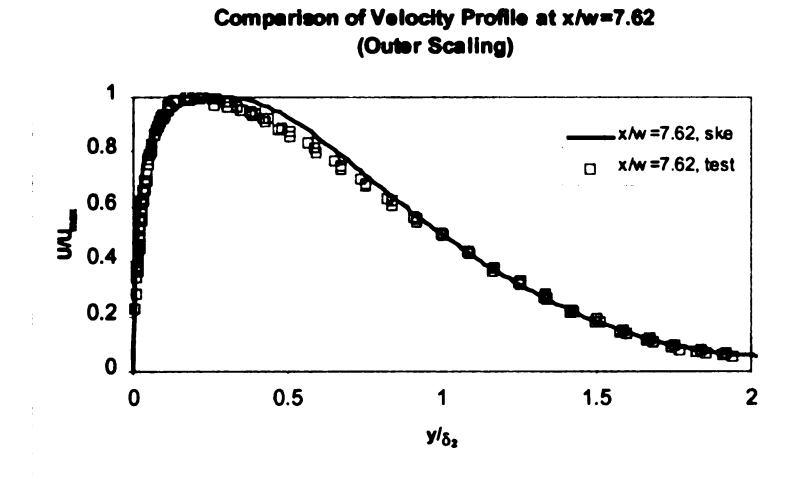


Figure 14. Comparison of Velocity Profiles (Outer Scaling, ske, A)





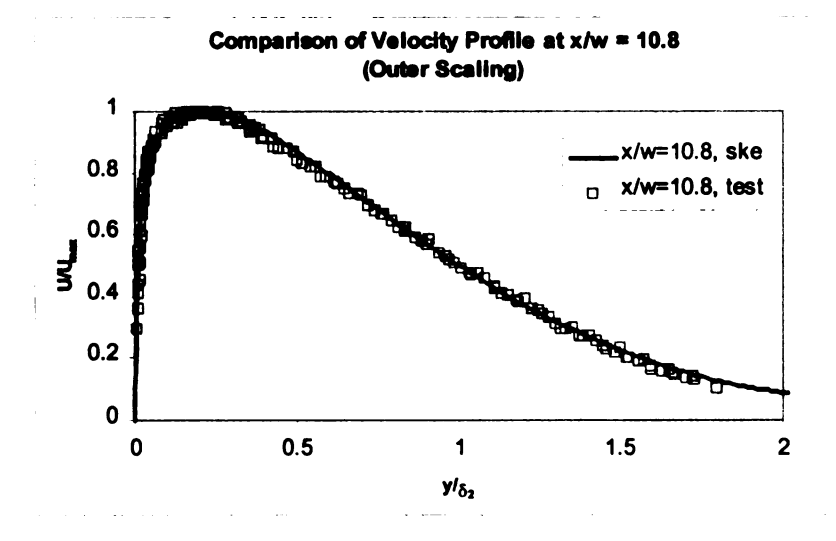
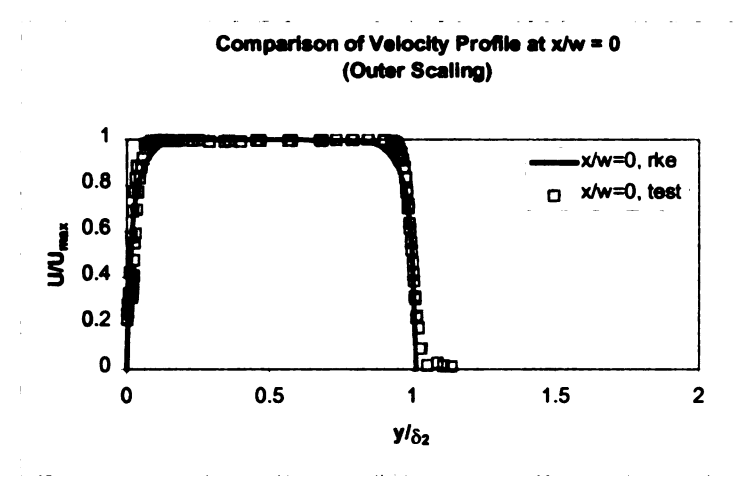
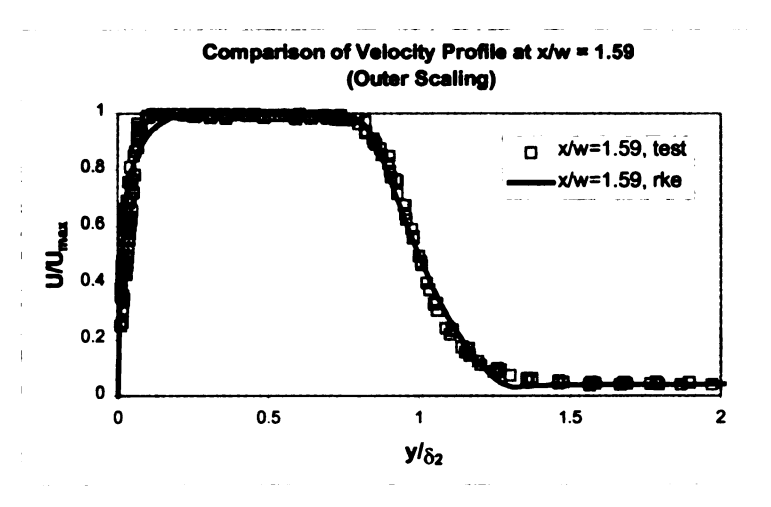


Figure 15. Comparison of Velocity Profiles (Outer Scaling, ske, B)





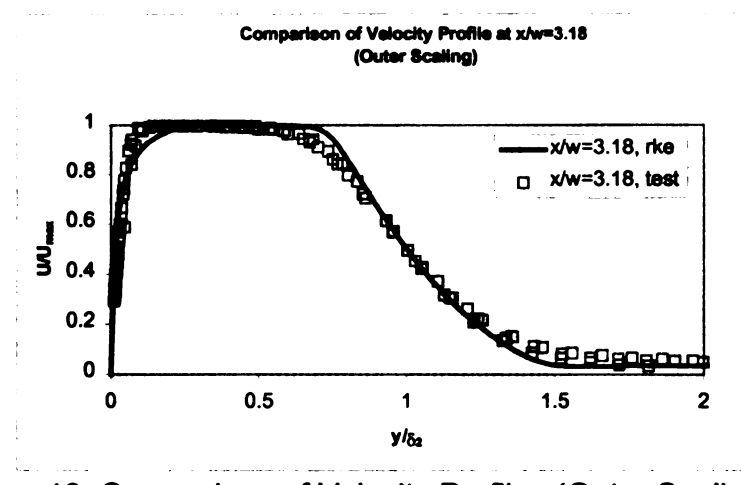
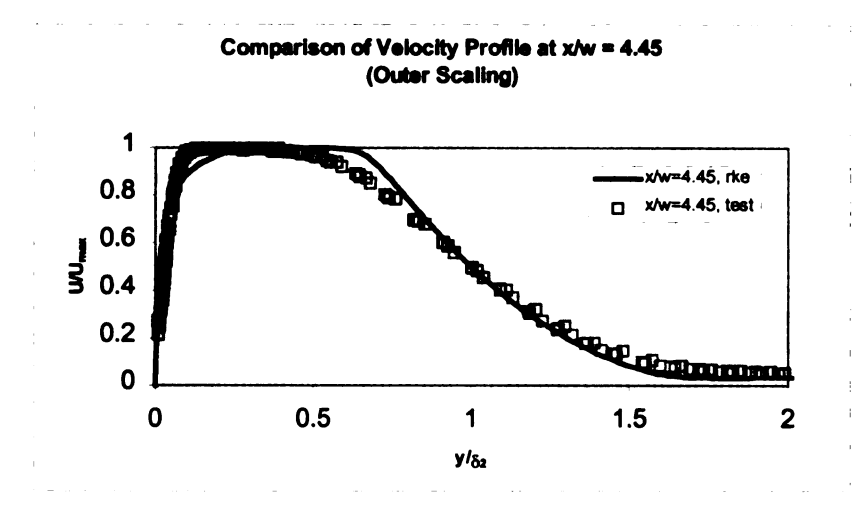
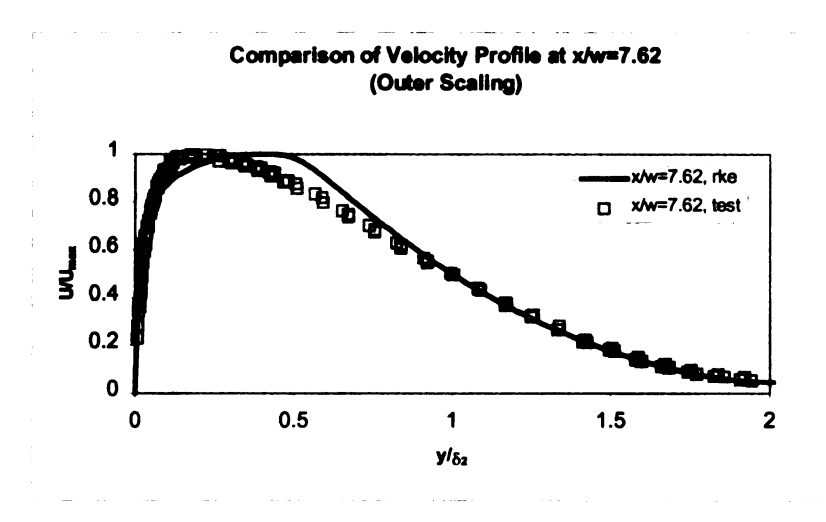


Figure 16. Comparison of Velocity Profiles (Outer Scaling, rke, A)





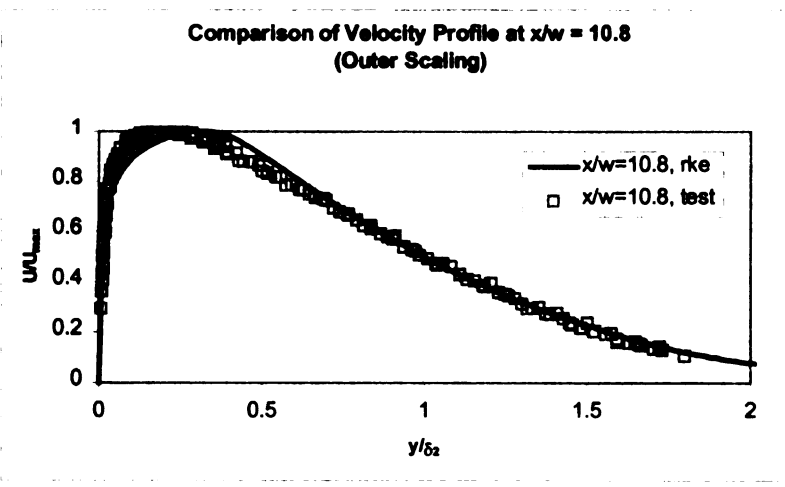
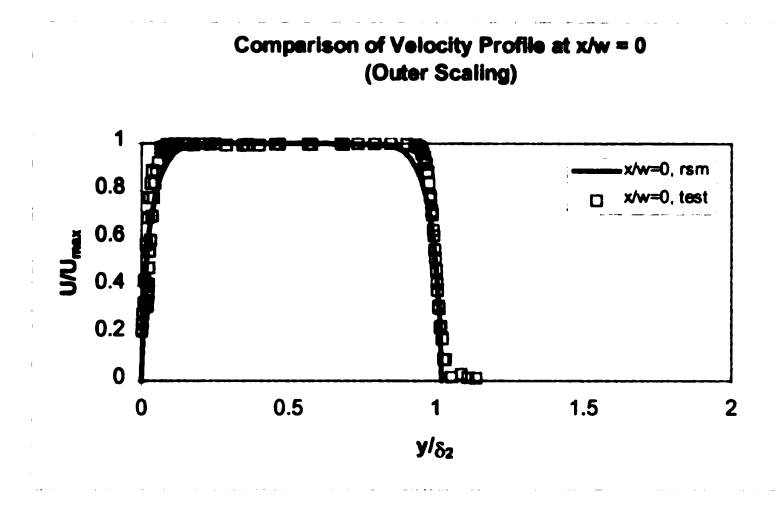
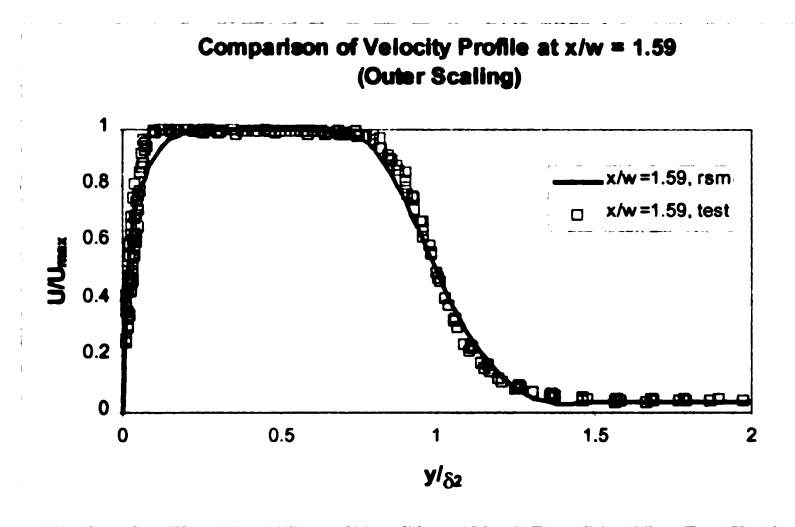


Figure 17. Comparison of Velocity Profiles (Outer Scaling, rke, B)





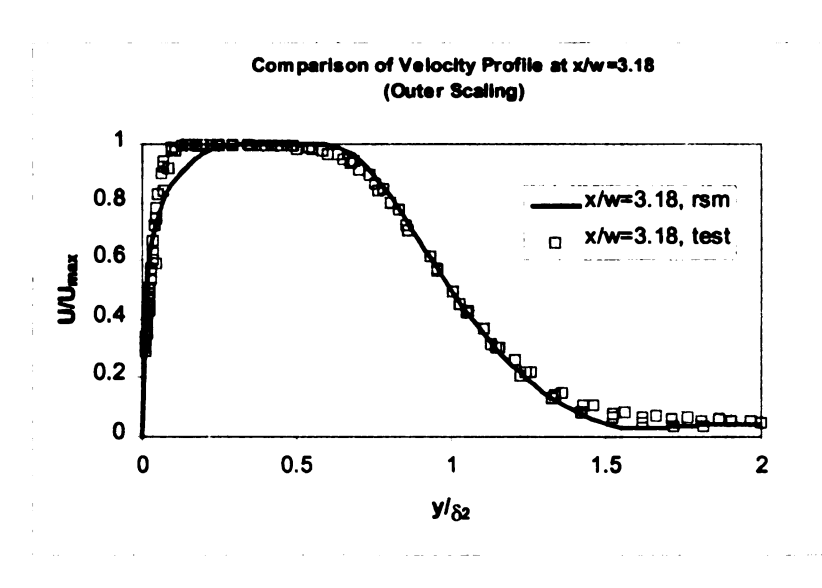
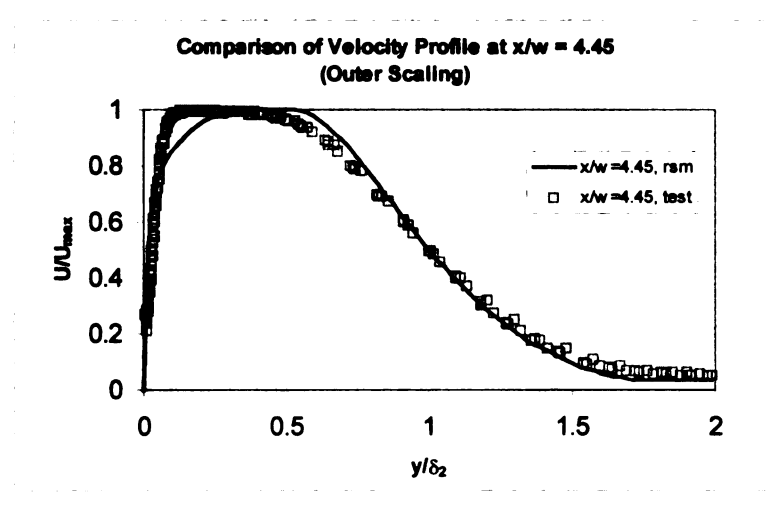
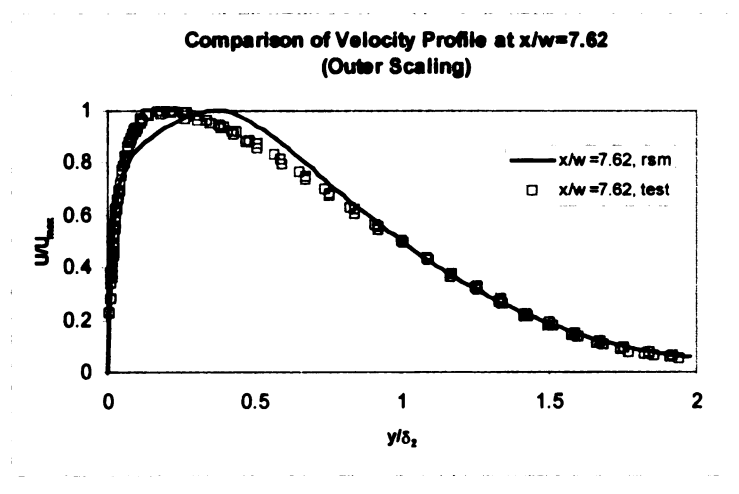


Figure 18. Comparison of Velocity Profiles (Outer Scaling, rsm, A)





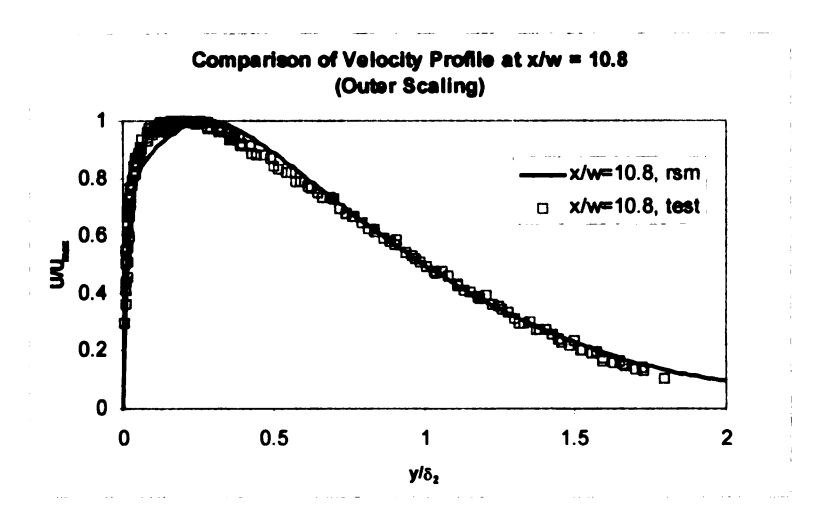
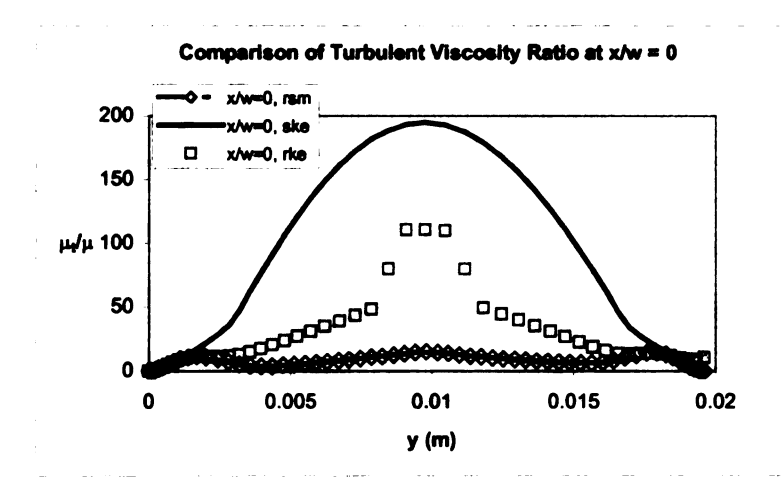
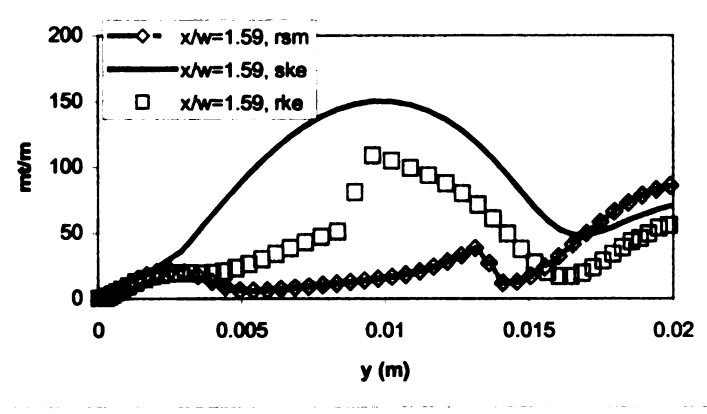


Figure 19. Comparison of Velocity Profiles (Outer Scaling, rsm, B)







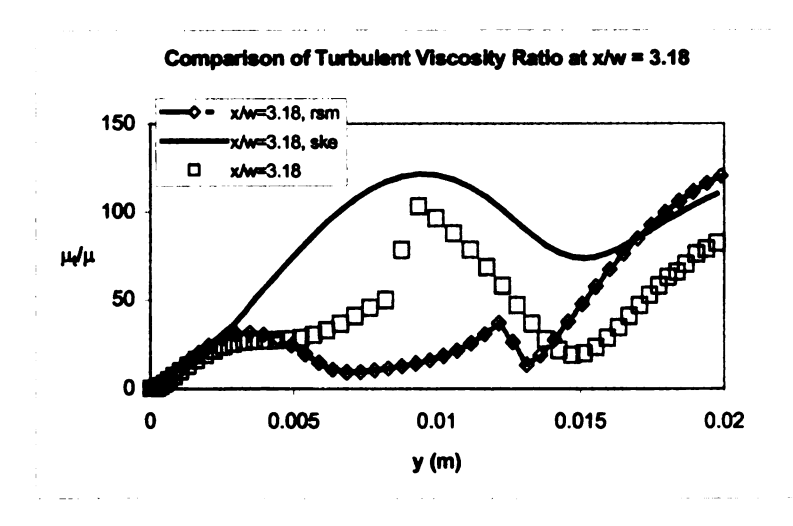
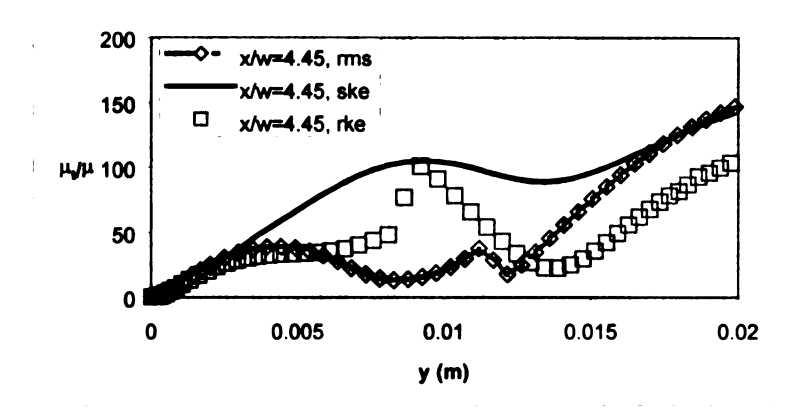
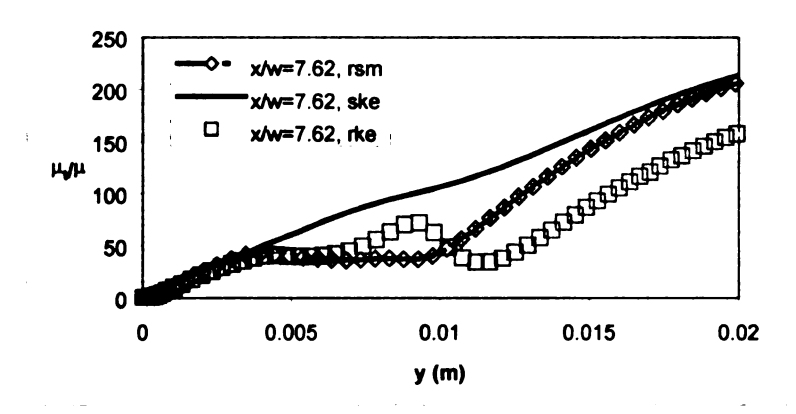


Figure 20. Comparison of Turbulent Viscosity Ratio (A)

Comparison of Turbulent Viscosity Ration at x/w = 4.45



Comparison of Turbulent Viscosity Ratio at x/w = 7.62



Comparison of Turbulent Viscosity Ratio at x/w =10.8

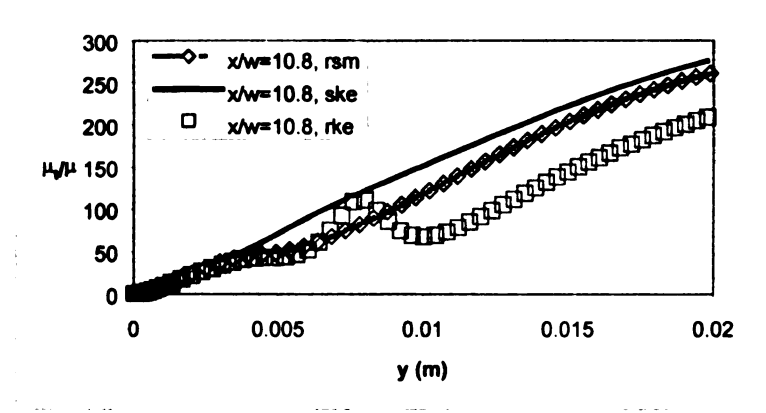
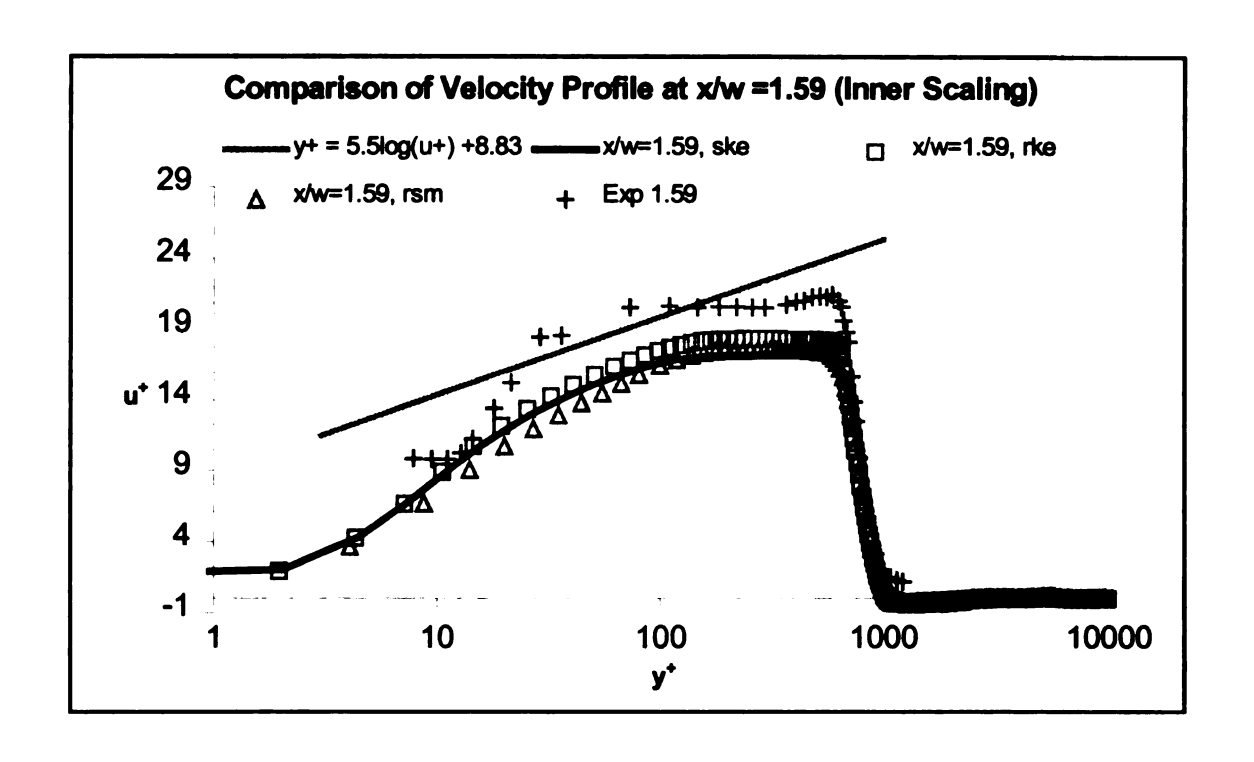


Figure 21. Comparison of Turbulent Viscosity Ratio (B)



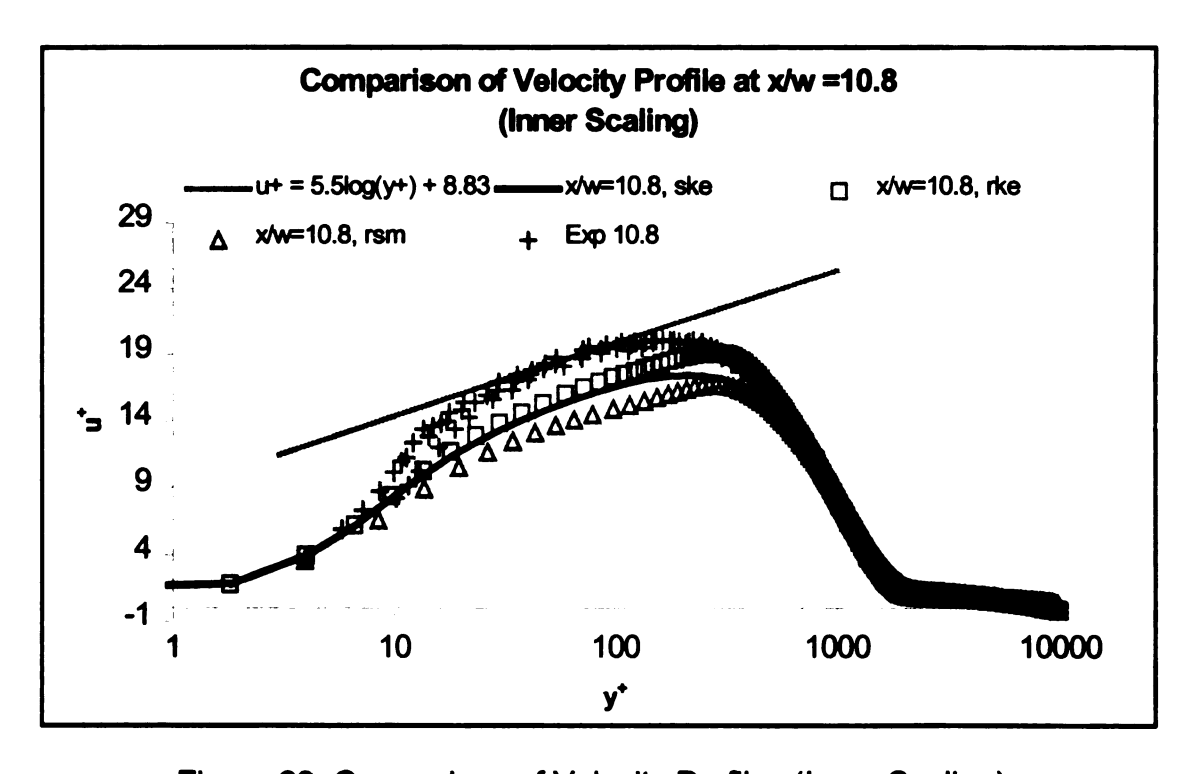
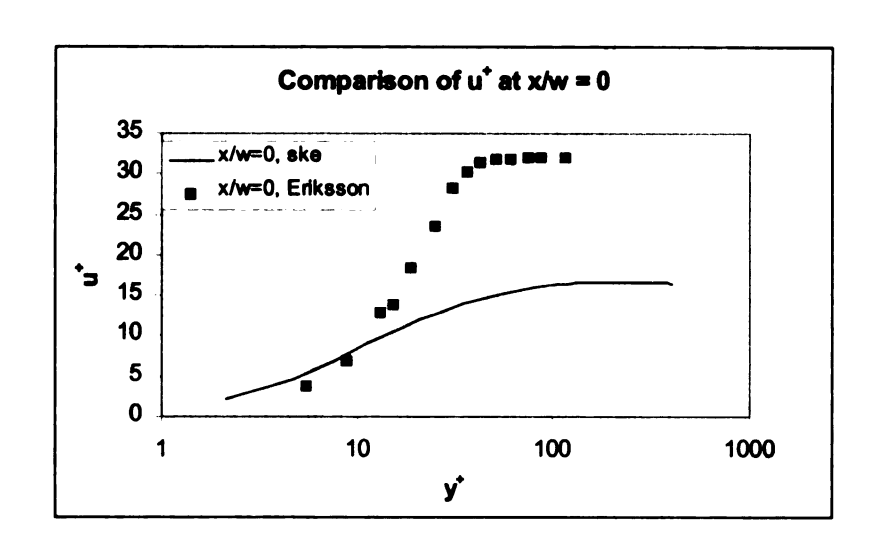
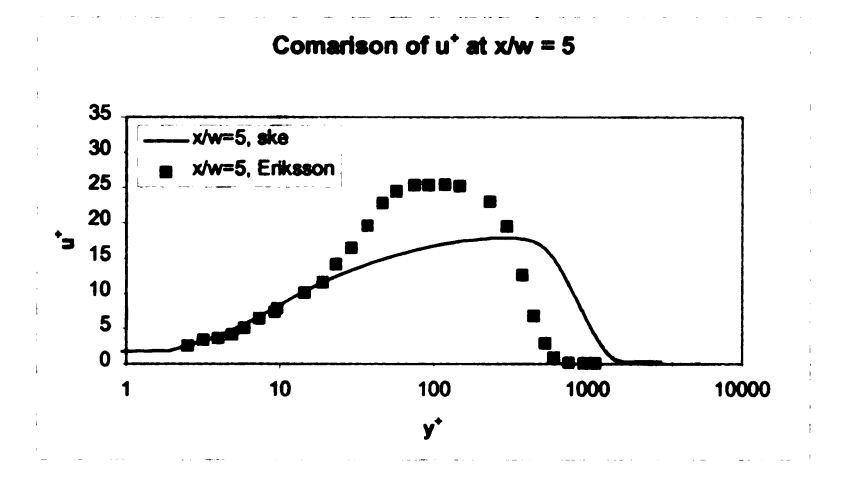


Figure 22. Comparison of Velocity Profiles (Inner Scaling)





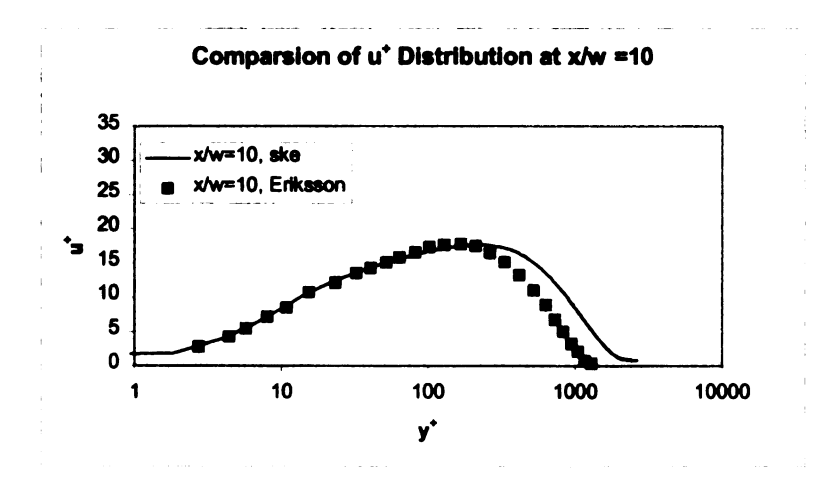


Figure 23. Comparison of u⁺ Distribution

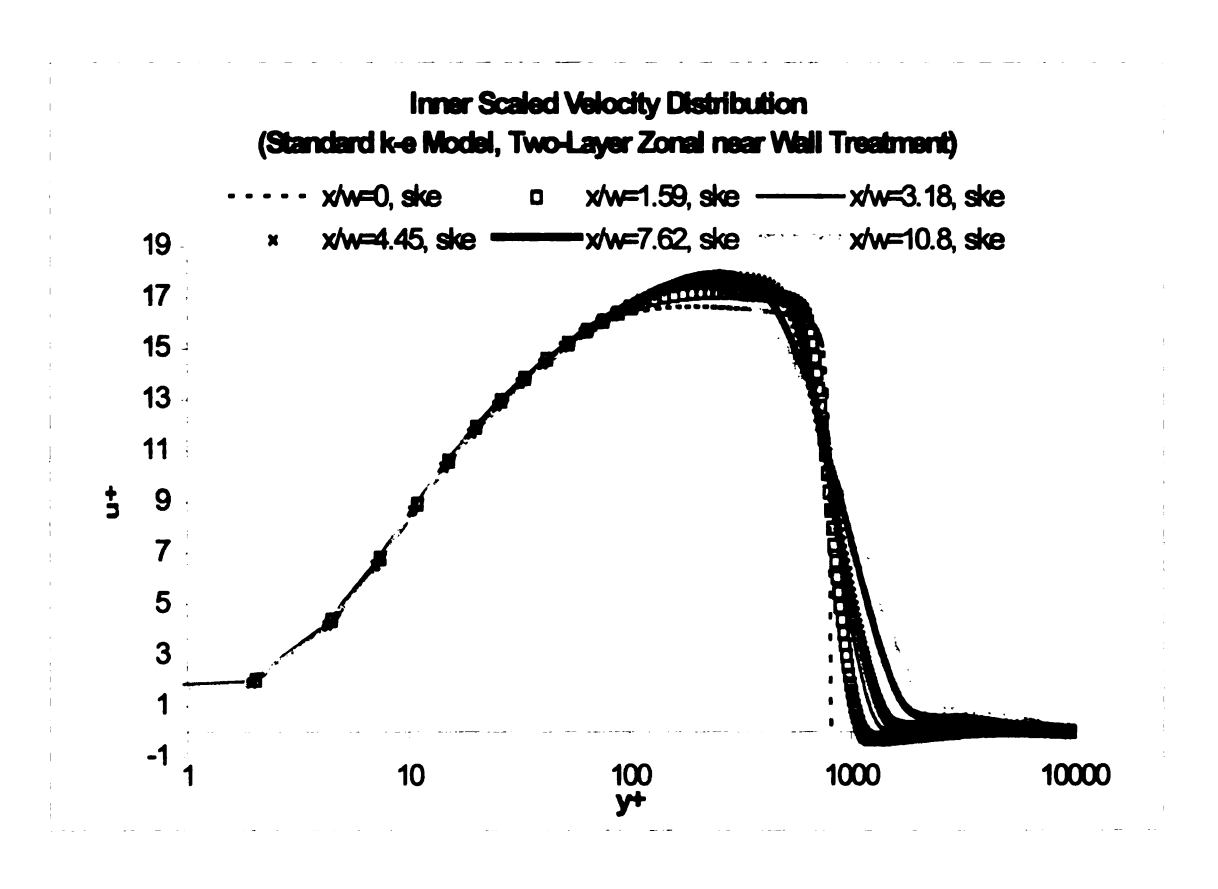
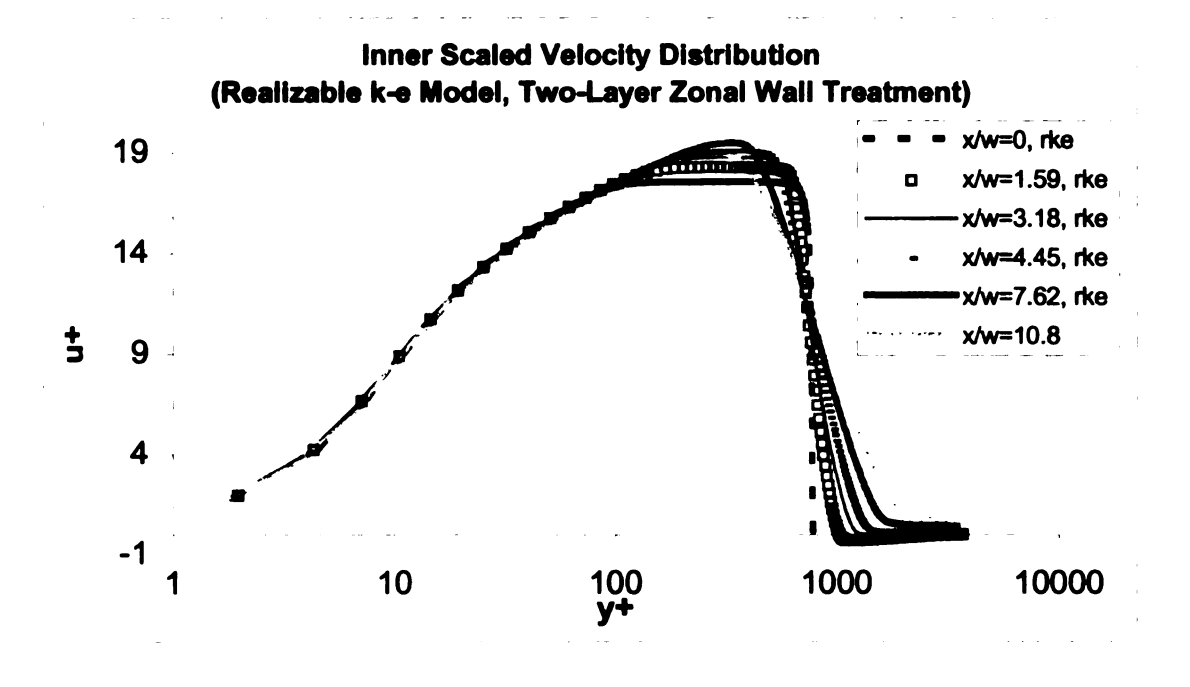


Figure 24. Overall Inner-Scaled Predictions of u⁺ Distribution (ske)



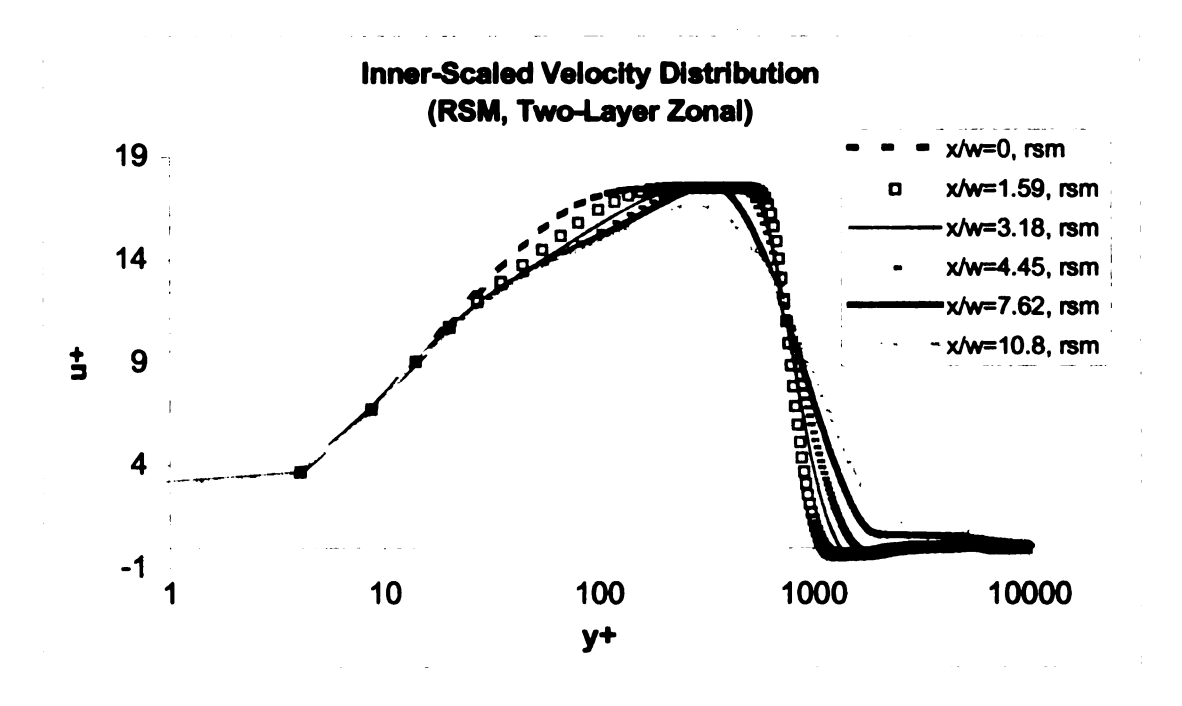
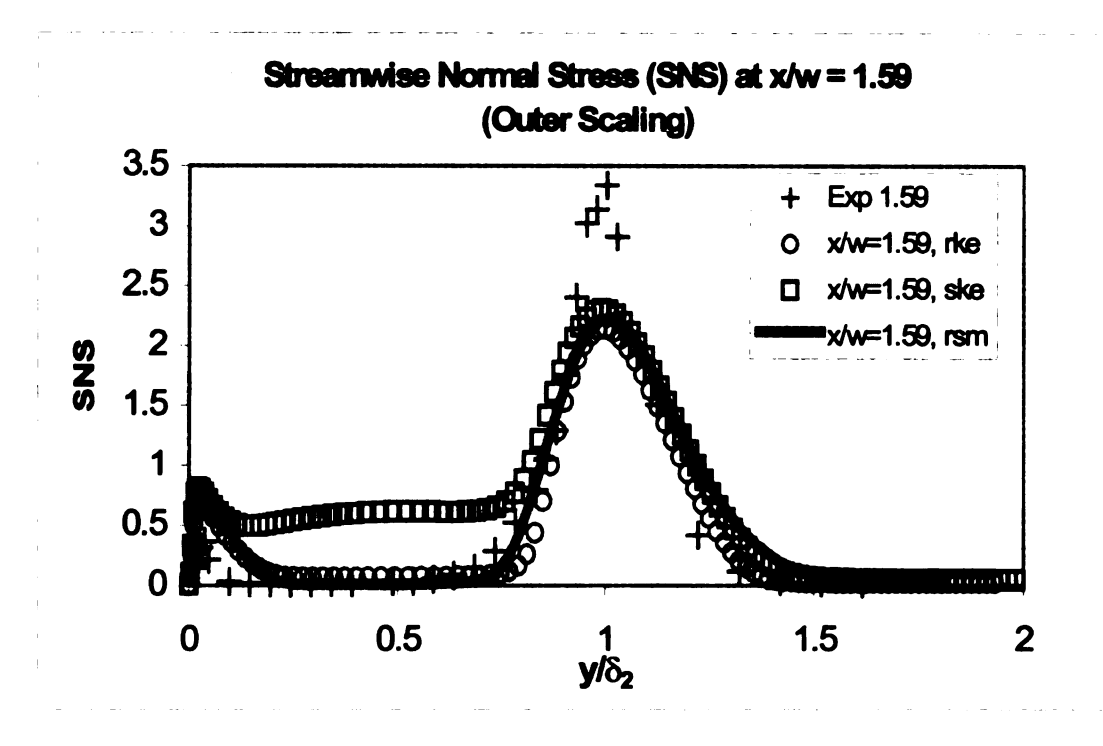


Figure 25. Overall Inner-Scaled Predictions of u⁺ Distribution (rke and RSM)



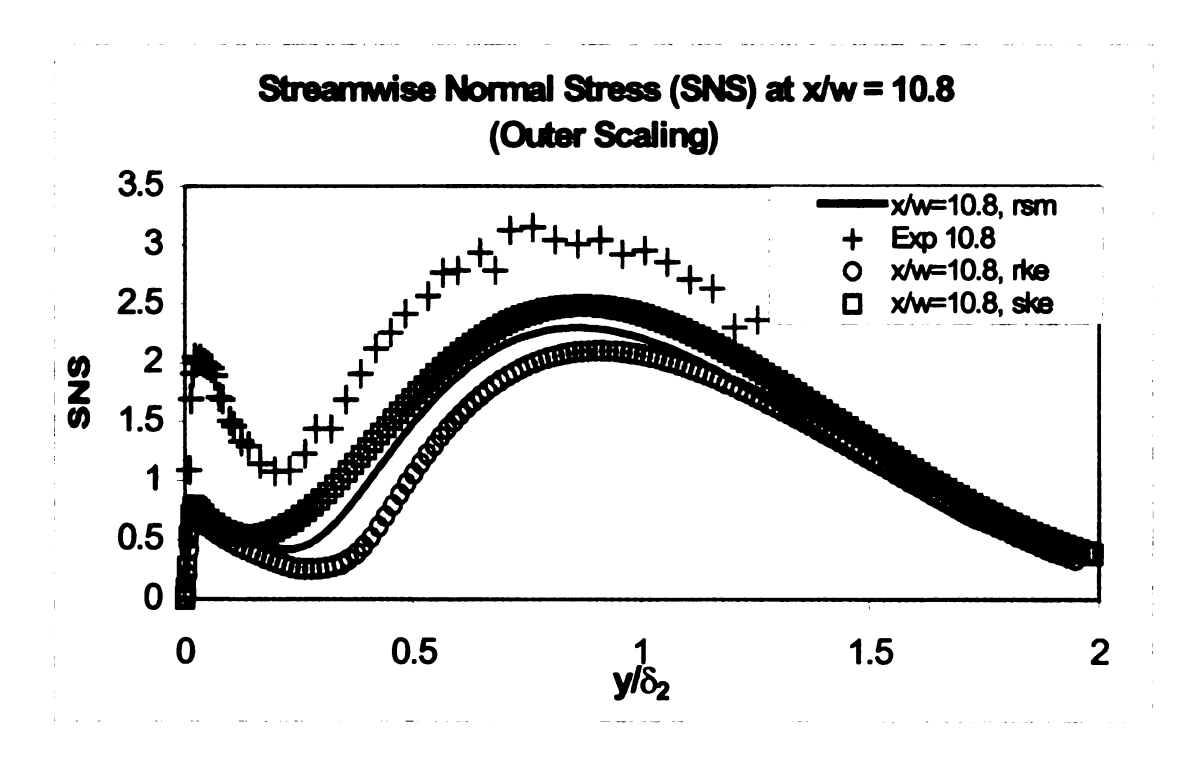
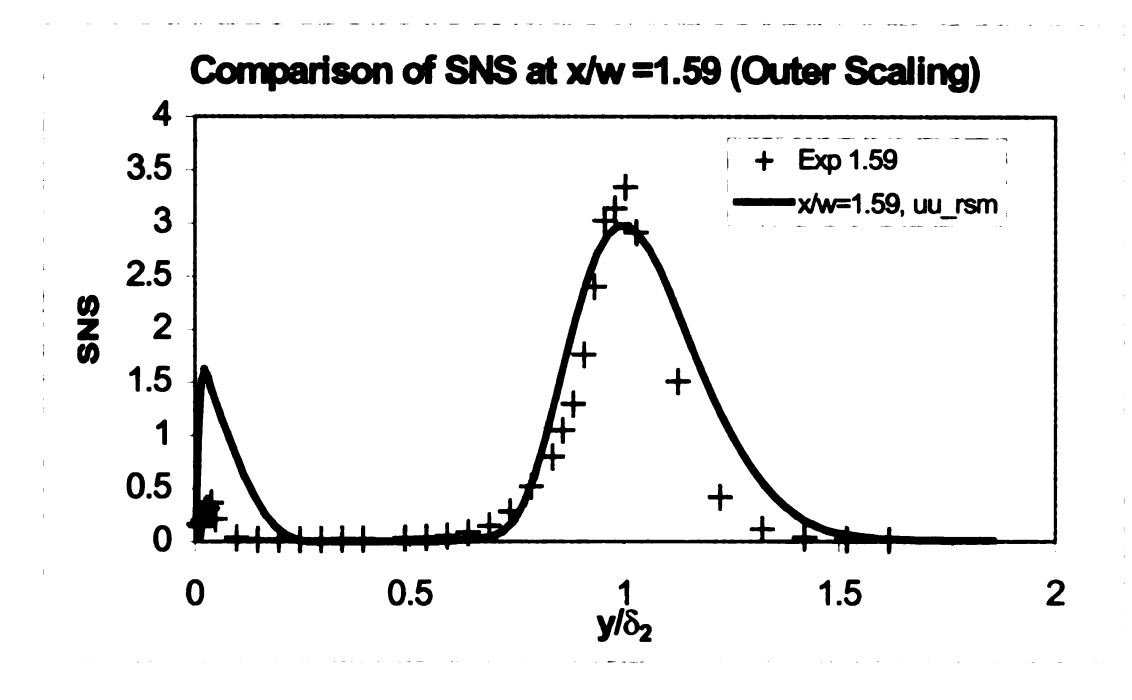


Figure 26. Comparison of SNS (Outer Scaling, A)



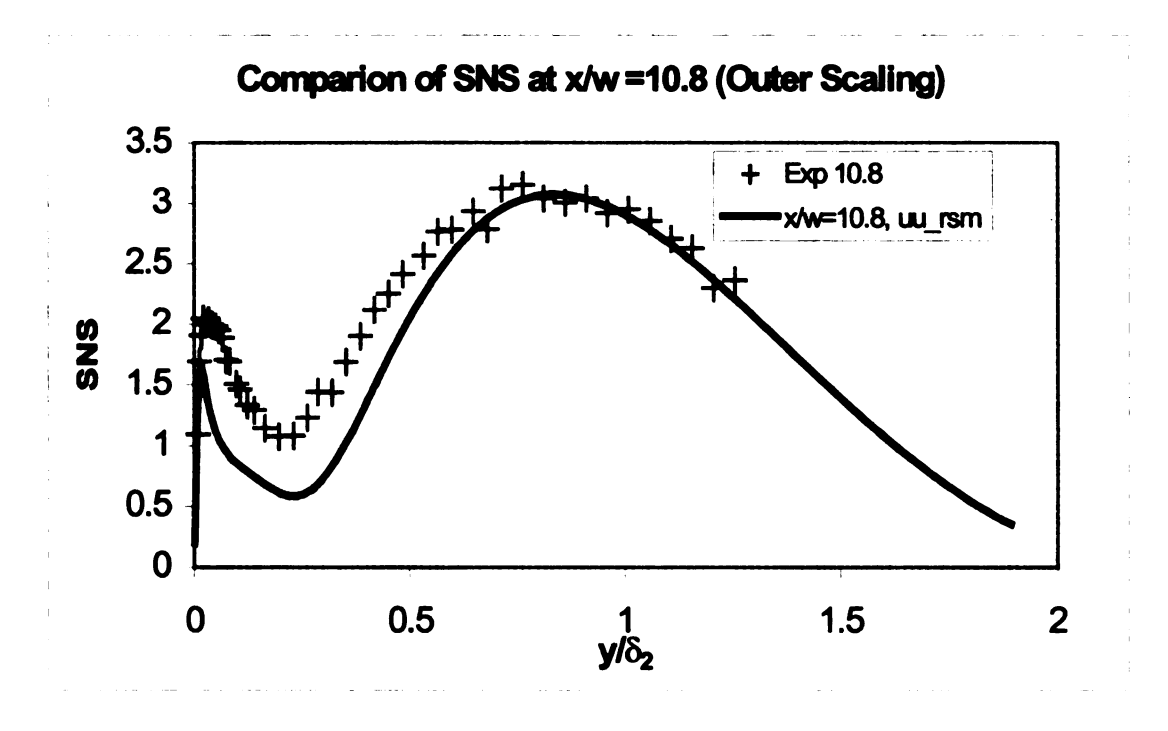
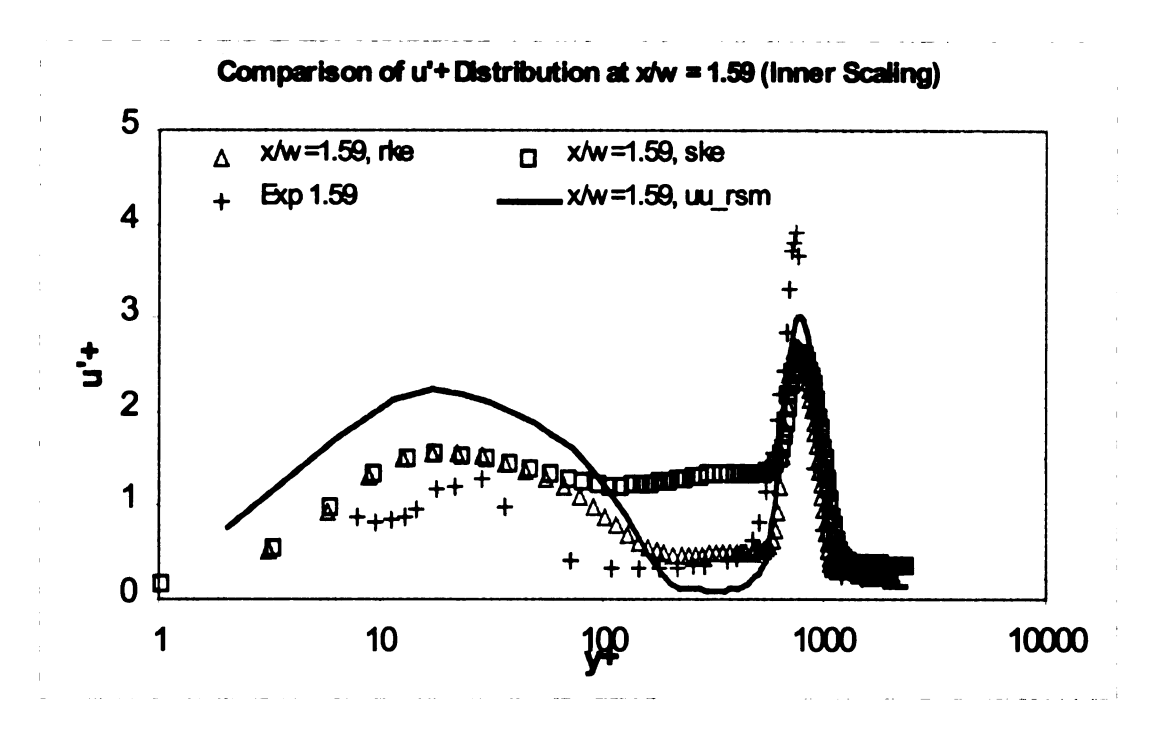


Figure 27. Comparison of SNS (Outer Scaling, B)



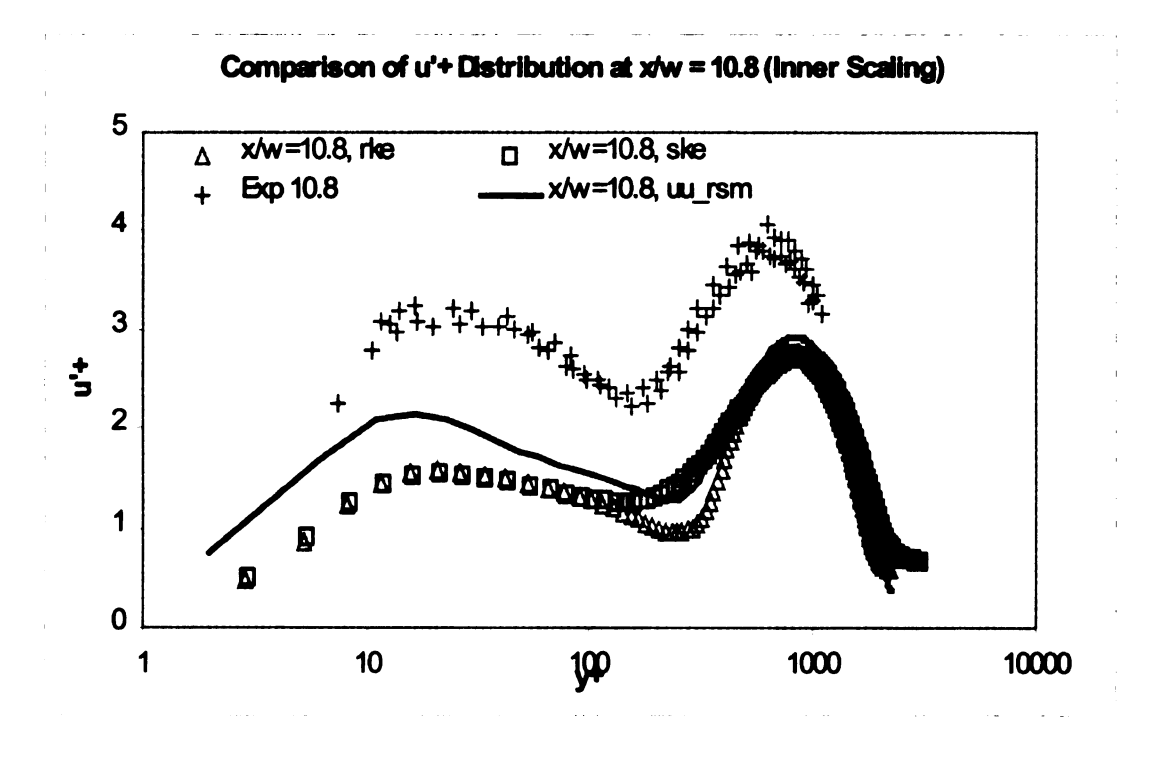
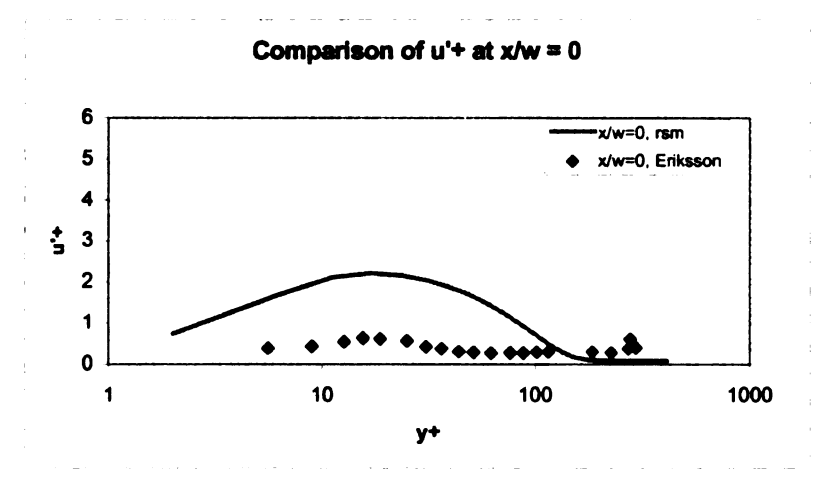
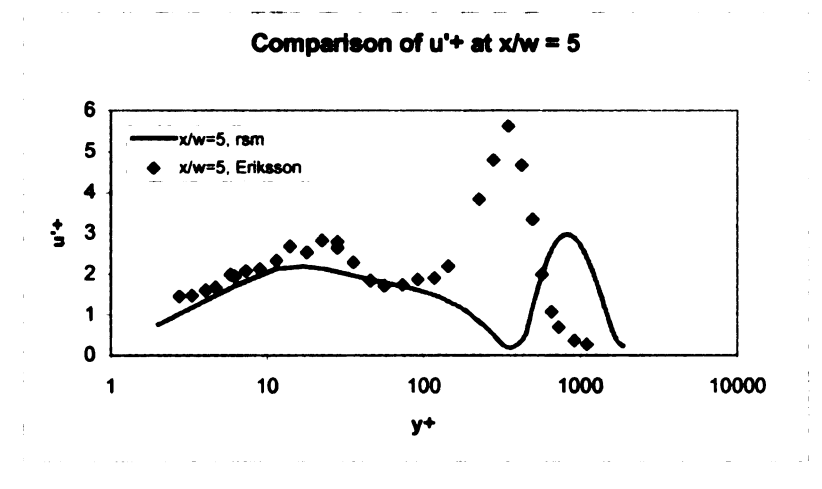


Figure 28. Comparison of u' (Inner Scaling, A)





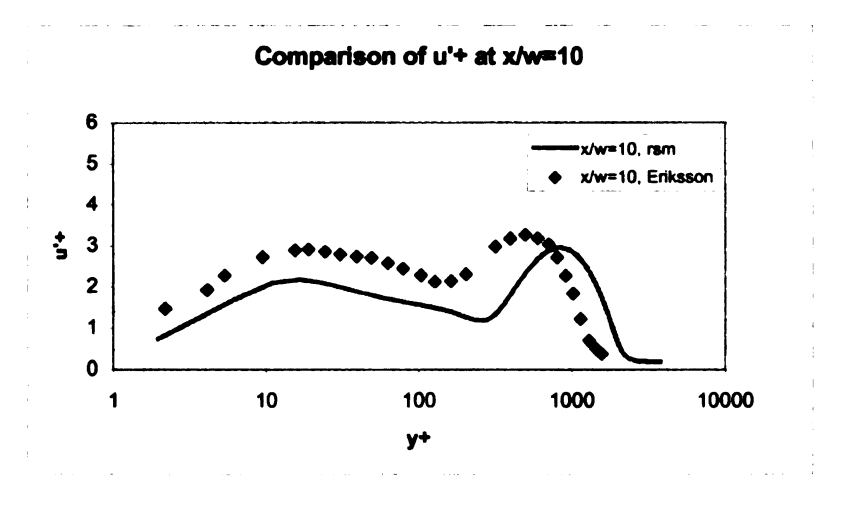
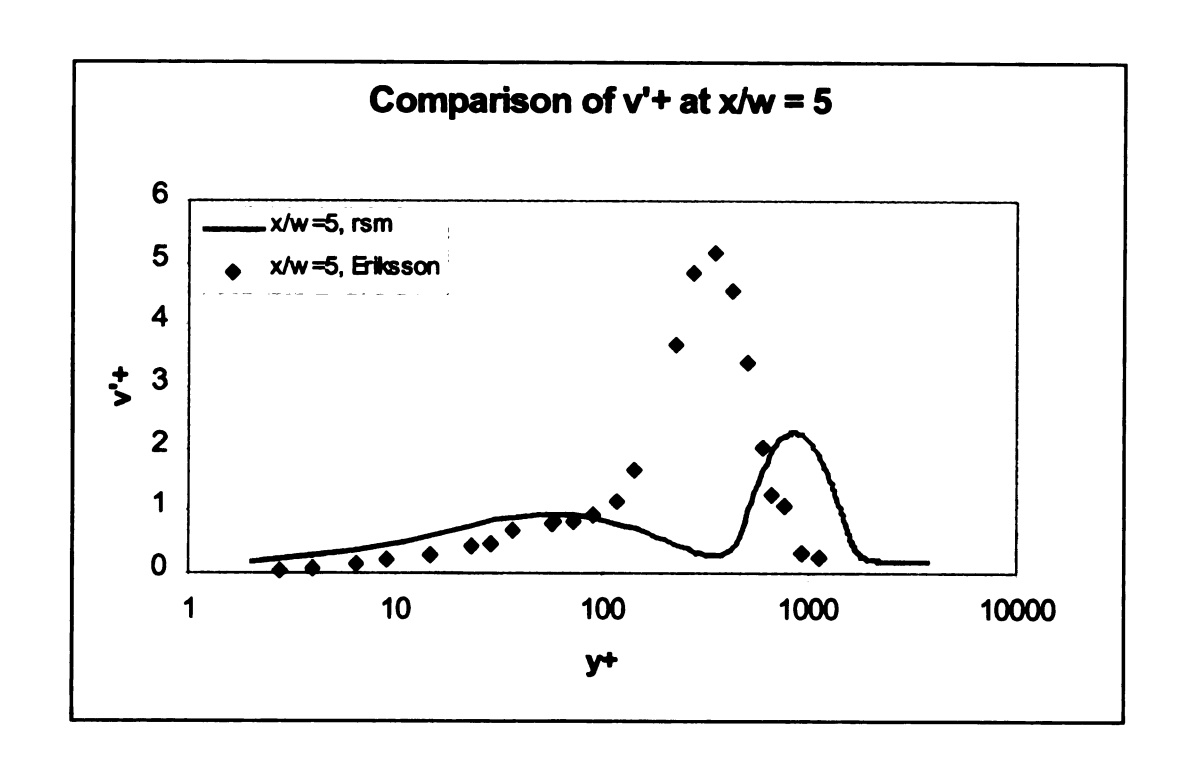


Figure 29. Comparison of u' (Inner Scaling, B)



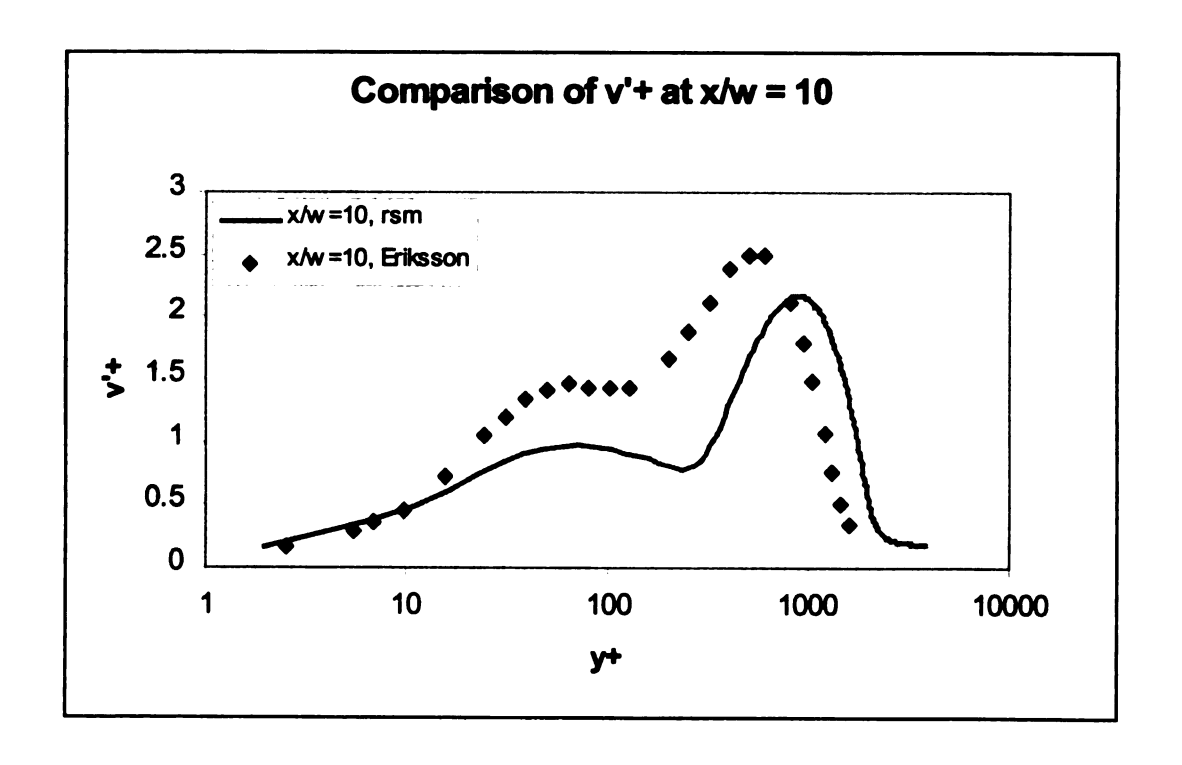
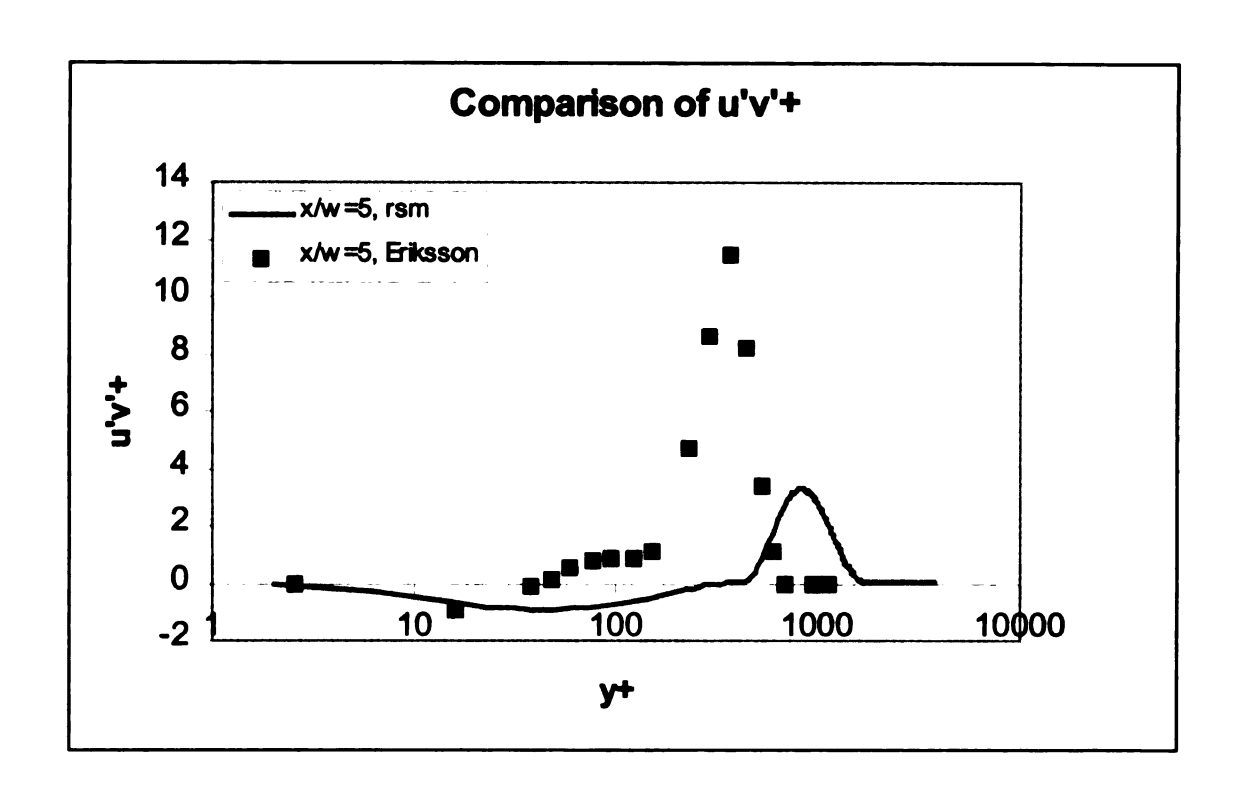


Figure 30. Comparison of $\overline{v'}^{\dagger}$ (Inner Scaling)



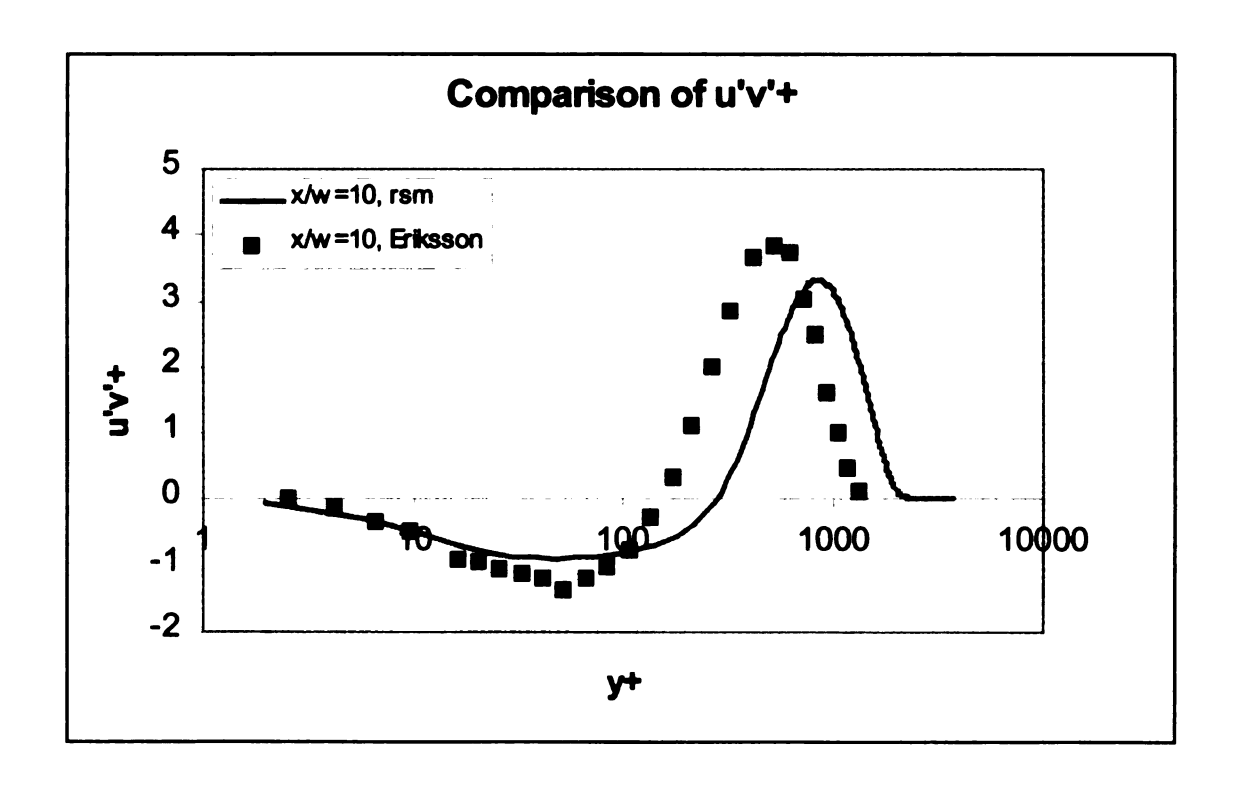


Figure 31. Comparison of $\overline{u'v'}^{\dagger}$ (Inner Scaling)

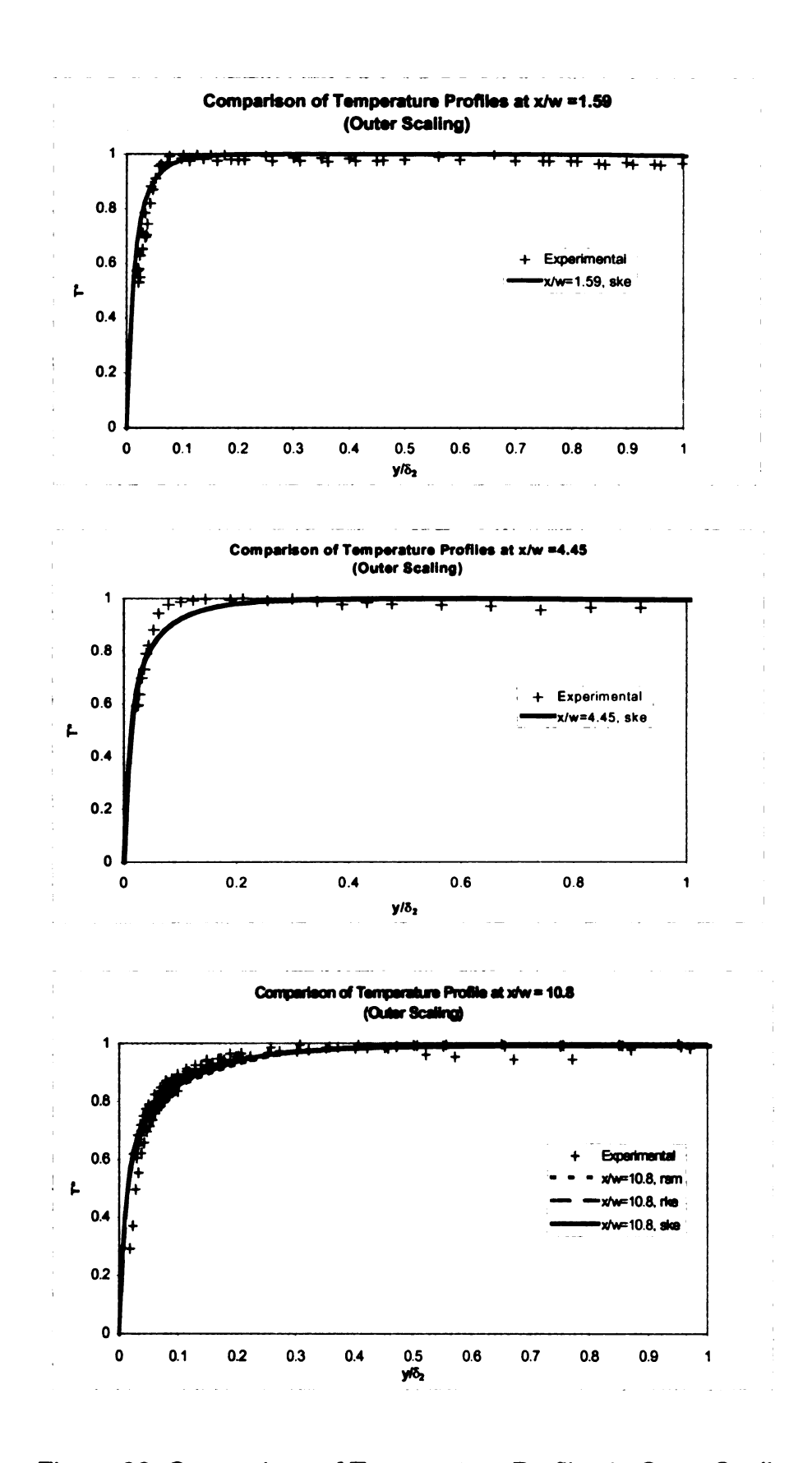


Figure 32. Comparison of Temperature Profiles in Outer Scaling

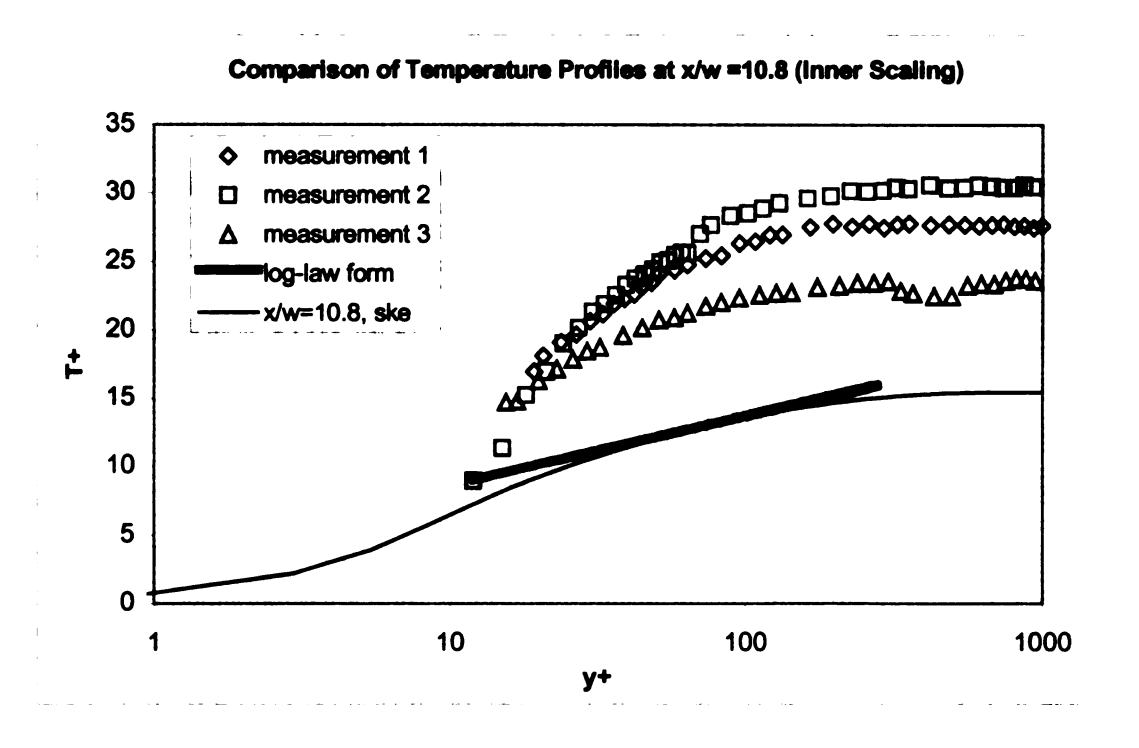


Figure 33. Comparison of Inner-Scaled Temperature Profiles at x/w = 10.8

Chapter 4

SIMULATIONS WITH PHASE CHANGE MODELS

The mass transfer of water, especially that which occurs on the interior surface of the windshield, is the most important factor that affects the visibility of the driver in an automotive vehicle. Therefore, a successful simulation of the mass transfer is a crucial step towards computer-aided design for the windshield defogger optimization.

Analogous to the relationship between temperature distribution and heat transfer, the concentration distribution of water needs to be predicted in order to simulate mass transfer. Analogous to the heat transfer, the simulation of the velocity field forms an important basis of mass transfer predictions as can be seen in the concentration equation (2.9). On the other hand, the phase change phenomenon involved in defogging will affect the temperature distribution. With thermodynamic equilibrium taken into account, the concentration distribution (mass transfer) is coupled with the temperature distribution (heat transfer) of water, even if the velocity distribution is assumed to be unaffected by the phase change.

In this chapter, the impact of phase change (condensation/evaporation) on heat and mass transfer will be investigated, and the task of modeling the phase change phenomenon will be considered with respect to the commercial CFD code FLUENT 5.0.

4.1 Some Basics about Mass Transfer

Before the phase change models are introduced, it beneficial to introduce a brief review about some basic ideas in mass transfer.

4.1.1 General Mixture

Suppose a single-phased mixture has n species. The mass concentration (also known as the partial density) of species i', $\rho_{i'}$, is defined as

$$\rho_{i'} = \frac{m_{i'}}{V} \tag{4.1}$$

where $m_{l'}$ is the mass of species i' in the mixture sample; and V is the volume of the mixture sample. The density of the mixture, ρ , is the sum of the partial densities:

$$\rho = \sum_{i'=1}^{n} \rho_{i'} \tag{4.2}$$

The mass fraction of species i', $\Phi_{i'}$, is defined as

$$\Phi_{i'} = \frac{\rho_{i'}}{\rho} \tag{4.3}$$

which is the main variable involved in the concentration equation

$$\frac{\partial}{\partial t} (\rho \Phi_{i'}) + \frac{\partial}{\partial x_i} (\rho u_i \Phi_{i'}) = -\frac{\partial}{\partial x_i} J_{i',i} + R_{i'} + S_{i'}$$
(2.9)

and Fick's law is

$$J_{i',i} = -\rho D_{i',m} \frac{\partial \Phi_{i'}}{\partial x_i} \tag{2.10}$$

The following equations hold when the sum of the volumetric rates of creation for all the individual species is zero:

$$u = \frac{1}{\rho} \sum_{i'=1}^n \rho_{i'} u_{i'}$$

$$v = \frac{1}{\rho} \sum_{i'=1}^{n} \rho_{i'} v_{i'} \tag{4.4}$$

where u and v are the bulk or mass-averaged velocity components of the mixture; and u_i and v_i are the x and y velocity components of species i'.

The mole fraction of species i' in a sample mixture containing N moles is defined as

$$x_{i'} = \frac{N_{i'}}{N}$$
 (4.5)

where $N_{i'}$ is the number of moles of i' in that sample. Clearly,

$$N = \sum_{i'=1}^{n} N_{i'} \tag{4.6}$$

and

$$\sum_{i'=1}^{n} x_{i'} = 1 {(4.7)}$$

If M_i and M are the molar mass of species i' and the mixture, respectively, then

$$N_{i'} = \frac{m_{i'}}{M_{i'}} \tag{4.8}$$

$$N = \frac{m}{M} \tag{4.9}$$

and
$$M = \sum_{i'=1}^{n} x_{i'} M_{i'}$$
 (4.10)

The relationship between the mass and mole fractions of species i' is

$$x_{i'} = \frac{M}{M_{i'}} \Phi_{i'} \tag{4.11}$$

It is worth noting that, for an ideal gas mixture,

$$x_{i'} = \frac{P_{i'}}{P} \tag{4.12}$$

where Pr is the partial pressure of species i'; and

$$P = \sum_{i'=1}^{n} P_{i'} \tag{4.13}$$

4.1.2 Water Vapor and Dry Air

With Fick's law, the velocity component of air in the binary vapor-air mixture can be written as [10]

$$u_{a} = u - \frac{\rho_{a} + \rho_{v}}{\rho_{a}} D \frac{\partial}{\partial x} \left(\frac{\rho_{a}}{\rho_{a} + \rho_{v}} \right), \quad v_{a} = v - \frac{\rho_{a} + \rho_{v}}{\rho_{a}} D \frac{\partial}{\partial y} \left(\frac{\rho_{a}}{\rho_{a} + \rho_{v}} \right)$$
(4.14)

where u_a and v_a are the x and y velocity components of air; u and v are the bulk or mass-averaged velocity components of the mixture.

For a water vapor and dry air mixture, the relative humidity is defined as

$$\phi = \frac{m_v}{m_{col}} = \frac{P_v}{P_{col}} \tag{4.15}$$

where P_v is the partial pressure of vapor in the mixture; and P_{sat} is the saturation pressure of the vapor. For an ideal gas mixture under a constant total pressure, P_v (say 1 atm),

$$\phi = \frac{P_{v}}{P_{sat}} = \frac{P_{v}/P}{P_{sat}/P} = \frac{x_{v}}{(x_{v})_{sat}}$$
(4.16)

where x_v is the mole fraction of vapor; and $(x_v)_{sat}$ is the saturation mole fraction.

At a given pressure, there exists a temperature dependent "moisture capacity" of air, which is the maximum amount of moisture the air can hold. At this point, the air is saturated, and the relative humidity is 100 percent. Any further drop in temperature or addition of moisture results in condensation of water vapor into liquid water (dew) in order to keep the thermodynamic equilibrium. The dew point temperature, T_{dp}, is defined as the temperature at which condensation begins if the air is cooled at constant pressure [19]. Note that as a mixture cools at constant pressure, the partial pressure of vapor P_v remains constant until the temperature drops below the dew point.

There exists a definite relation between the saturation pressure, P_{sat}, and the saturation temperature, T_{sat}, during a phase change process. By treating the vapor as an ideal gas and the latent heat of condensation/evaporation as a constant, this relation can be described by the Clapeyron-Clausius equation [19]

$$\ln\left(\frac{P_2}{P_1}\right)_{sat} \cong \frac{L}{R}\left(\frac{1}{T_1} - \frac{1}{T_2}\right)_{sat} \tag{4.17}$$

where L is the assumed constant latent heat at some average value; and R is the gas constant of water vapor. L, R, T_1 , and T_2 are all expressed in the SI unit system.

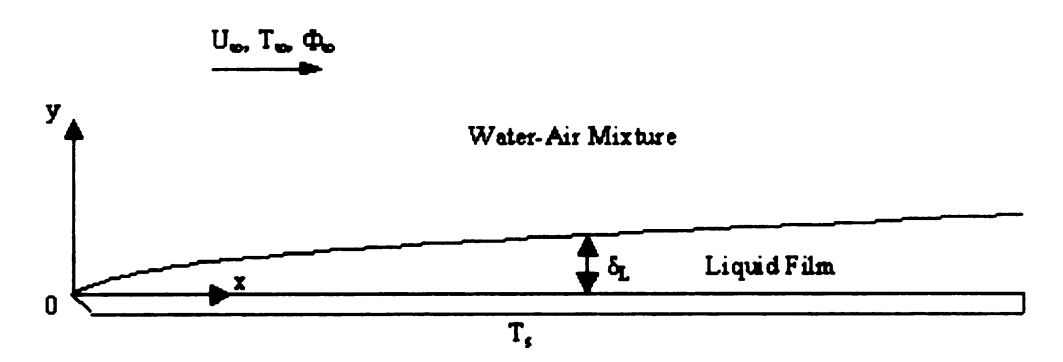
4.2 Surface Phase Change Model

For the time being, the situation of forced convection condensation on a flat plate in the presence of a non-condensable gas will be taken as an example to illustrate the ideas of phase change modeling. The analysis of evaporation has the same nature.

4.2.1 Model Analysis

Due to the limitation of the current version of FLUENT, it is difficult to include the liquid condensate film (see Figure 4) in the simulation. The "thin film" assumption employed by many researchers mentioned in Chapter 1 is adopted in the present model.

As in Figure 4 (reproduced below), the liquid film which remains on the surface is assumed to be infinitesimally thin so that it has no influence on the velocity field and heat transfer.



The key approximation of the surface phase change model is that the condensation occurs ONLY on the surface of the plate.

The fluid is assumed to be an ideal gas mixture of water vapor and dry air. In other words, the flow is in single (gaseous) phase with binary species (vapor and air) in the computational domain. The boundary of the computational domain actually starts from the interface between the gaseous phase and liquid film.

Since the phase change (condensation or evaporation) is assumed to occur ONLY on the surface, there are no droplets of liquid water formed volumetrically in the computational domain. No thermodynamic equilibrium is required, the vapor remains in the gaseous phase even when the local temperature is below

the dew point. Thus, volumetrically, neither latent heat release nor mass consumption needs to be accounted for in the gaseous phase.

The latent heat released at the interface does not affect the temperature distribution because the temperature is always held constant on the surface. The flow in the computational domain can not "see" the latent heat released when condensation occurs on the surface, but can see only the constant temperature condition. By keeping the surface temperature constant, the latent heat released due to condensation is absorbed into the plate surface instead of the flow.

Again, analogous to convection heat transfer, the driving force of the mass transfer onto the surface of the plate is the concentration differential of vapor between the interface and the main stream of the flow.

With the above assumptions, the boundary conditions at the interface can be defined as:

- The temperature is the same as the one on the wall surface, T_s;
- The mass fraction of water vapor is the one corresponding to the saturated concentration of vapor at T_s;
- The no-slip (u=0), impermeable surface model (v=0) is adopted for the velocity.

Strictly speaking, the impermeable surface condition imposed at the interface is another approximation [14] (called impermeable surface model).

Actually, the interface is impermeable to air only, and is "sucking" (condensation) or "blowing" (evaporation) for the species of water vapor. The exact velocity boundary condition at the interface should be

$$v_a|_{v=0} = 0$$
 (4.18)

where v_a is the y velocity component of air. With equation (4.14), the equivalent statement of equation (4.17) is

$$v\big|_{v=0} = \frac{\rho_a + \rho_v}{\rho_a} D \frac{\partial}{\partial y} \left(\frac{\rho_a}{\rho_a + \rho_v} \right)$$
 (4.19)

However, the v = 0 approximation is justified only when the concentration of the species of interest is "low", namely, lower than a critical level [14]:

$$\frac{\rho_w - \rho_\infty}{\rho} < Sc^{1-n} \tag{4.20}$$

where Sc is the Schmidt number (0.6 for air-vapor mixture); n is 1/3 when Sc is greater than 0.5, and 1/2 when Sc is less than 0.5. The air-vapor mixture meets this critical condition in the range of normal room temperature, which makes the impermeable surface model (v = 0) valid for the current study.

4.2.2 Model Implementation

The ideal gas mixture of non-condensable air and condensable water vapor was first set up in the "Define... Materials..." panel in FLUENT [12], with air as the main species. The density of the mixture is computed with the ideal gas law for an incompressible flow [12]

$$\rho = \frac{P_{op}}{RT\sum_{i'}\frac{\Phi_{i'}}{M_{i'}}} \tag{4.21}$$

where P_{op} is the operating pressure (1 atm). Theoretically, this makes all of the governing equations mentioned in Chapter 2 coupled together even if the

physical properties other than the density are assumed constants. Therefore, all the governing equations should be solved together, which makes the simulation more time-consuming.

As mentioned earlier, there exists a strong analogy between heat transfer and mass transfer. The temperature distribution can be obtained by solving the energy equation (2.4), from which FLUENT calculates the wall heat flux output and make it available to the user. Ironically, the current version of FLUENT does not provide the species mass flux output on the wall although the species concentration field has been obtained by solving the species concentration equation (2.9).

In order to get the vapor mass flux on the wall with equation (2.10), the derivative of the vapor is needed. A User Defined Function (UDF) was developed in a C program (attached as Appendix E), compiled, linked and run with the solver to get the information needed for the mass flux. In this UDF, the mass fraction of vapor is stored in the first User Defined Scalar, UDS(0) (C_UDSI(c,t,0) and F_UDSI(f,t,0) in the code), which makes the derivatives of the vapor mass faction available to the user (C_UDSI_G(c,t,0) in the code). For reference, the saturated mole fraction corresponding to the local temperature is calculated with equation (4.23) and stored in the second User Defined Scalar, UDS(1). The mass flux was calculated with equation (2.10) and stored in the third User Defined Scalar, UDS(2).

All the above operations were realized via the Define_Adjust function (or Macro [12]) named "spec_grad" in the code. The solver calls the Define_Adjust function at the beginning of every iteration [12].

If P_1 in equation (4.17) is set to be 1atm (equal to the mixture pressure of the current study), the saturation pressure of the vapor at temperature T can be obtained as

$$(P_{\nu})_{sat} = e^{\frac{L}{R}(\frac{1}{T_1} - \frac{1}{T})}$$
 [atm] (4.22)

where T_1 is the temperature at which the saturation pressure of the vapor takes the value of 1 atm. That is, T_1 is the boiling point of water (373.15 K) at 1 atm.

The pressure of the mixture for the current study is about 1 atm. For an ideal gas, the ratio of vapor partial pressure to the total pressure of the mixture equals the mole fraction as described in equation (4.12). Therefore,

$$(x_{\nu})_{sat} = \frac{(P_{\nu})_{sat}}{P} = \frac{e^{\frac{L}{R}(\frac{1}{T_{1}} - \frac{1}{T})}[atm]}{1[atm]} = e^{\frac{L}{R}(\frac{1}{T_{1}} - \frac{1}{T})}$$
 (4.23)

The saturated mass fraction is then obtained via the following equation [11]

$$(\Phi_{\nu})_{sat} = \frac{r(x_{\nu})_{sat}}{1 - (x_{\nu})_{sat}(1 - r)}$$
(4.24)

where r is the ratio of molecular weights of vapor (18 kg/kmol) and the air (29 kg/kmol). This calculation is consistent with equation (4.11), and is valid for non-saturated mixture as well.

In the UDF of Appendix E, the saturated mass fraction of vapor computed with equations (4.23) and (4.24) is imposed as the boundary condition for the plate of interest (via the DEFINE_PROFILE function [12]).

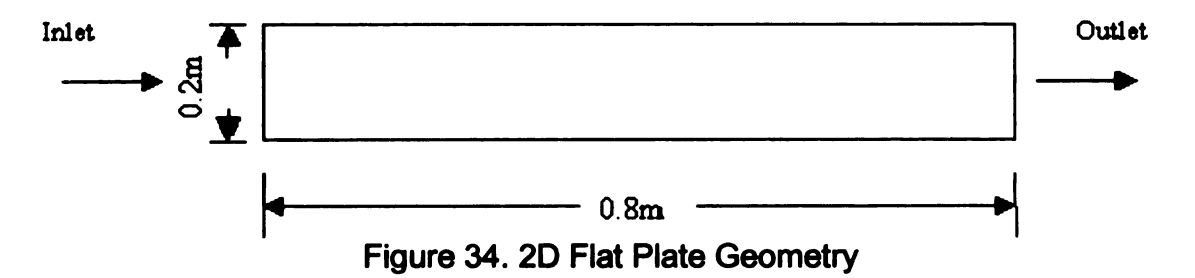
According to equations (4.16) and (4.23), the relative humidity, ϕ , can be obtained in FLUENT via manipulation in the "Define...Custom Field Functions..." menu [12]:

$$\phi = \frac{x_{v}}{\left(x_{v}\right)_{sat}} = \frac{x_{v}}{e^{\frac{L}{R}\left(\frac{1}{T_{1}} - \frac{1}{T}\right)}}$$

4.2.3 Results and Comparisons

The Flat Plate Case

To begin with, the 2D geometry in Figure 34 was created for the case of forced convection condensation on a flat plate in the presence of a non-condensable gas.



The distance between the two parallel plates is 0.2 m. The lengths of plates are both 0.8 m. The vapor-air mixture enters the system from the inlet with a constant velocity of 3 m/s, and goes out of the system at the outlet where a constant pressure is assumed. The lower plate is a thermally active one that is of interest, with a constant temperature and the corresponding saturated vapor mass fraction. The top plate is adiabatic with a zero gradient vapor mass fraction.

97

As seen in the comparisons in Appendix F, the numerical solutions for velocity and temperature of laminar flow are in good agreement with the similarity solutions [17] by Blasius and Pohlhausen without considering mass transfer (In FLUENT, set the fluid to be air only.). The good agreement suggests the above 2D geometry is acceptable to perform the simulation for a flat plate case illustrated in Figure 4.

For the mass transfer simulation, an ideal gas mixture of vapor and air is set up with the "Define... Materials..." menu [12]. The mass diffusivity, D, of the vapor in the mixture is assumed to be a constant. In order to compare the simulations with analytical solutions, the inlet temperature was first set equal to the temperature on the lower plate, say 303.15 K (30 °C). And the inlet (or main stream) mass fraction was set to be corresponding to 50% relative humidity (ϕ). With equation (4.16), the mole fraction, x_{∞} , corresponding to the relative humidity ϕ is obtained by

$$x_{\infty} = \phi(x_{\nu})_{sat} \tag{4.25}$$

Since FLUENT requires the mass fraction as the input for the concentration boundary condition, the corresponding mass fraction, Φ_{∞} , is then obtained with equation (4.24).

Alternatively, the inlet main stream mass fraction Φ_{∞} corresponding to the relative humidity ϕ_{∞} can be calculated via the so called absolute or specific humidity, ω , which is defined as

$$\omega = \frac{m_v}{m_a} \qquad \text{(kg water vapor/kg dry air)} \tag{4.26}$$

The relationship between the relative humidity and absolute humidity is

$$\omega = \frac{0.622\phi P_{sat}}{P - P_{sat}} \tag{4.27}$$

where P_{sat} can be computed from equation (4.22); and P is 1 atm.

The inlet mass fraction can then be calculated as

$$\Phi_{\infty} = \frac{\omega_{\infty}}{1 + \omega_{\infty}} \tag{4.28}$$

The local mass transfer coefficient of vapor along the lower plate is of interest in terms of mass transfer, which is defined as

$$h_{m} = \frac{J_{w}}{\rho_{w} - \rho_{m}} \tag{4.29}$$

where J_w is the mass flux at the wall; ρ_w is the mass concentration at the wall; and ρ_∞ is the mass concentration in the main stream. With equation (2.10),

$$J_{w} = -\rho D \left(\frac{\partial \Phi}{\partial y} \right)_{y=0} \tag{4.30}$$

where ρ is the mixture density at the wall; D is the mass transfer coefficient (mass diffusivity); and Φ is the mass fraction of vapor.

The analytical solution of h_m for the case of laminar flow over a flat plate is [14]

$$h_m = 0.332 \left(\frac{v}{D}\right)^{1/3} \left(\frac{U_{\infty}x}{v}\right)^{1/2} \frac{D}{x}$$
 (4.31)

when $v/D \ge 0.5$ (valid for the air-vapor mixture), where v is the kinetic viscosity of the fluid (assumed to be the same as dry air, 0.00001568867 m²/s).

The numerical solution of h_m is obtained by equation (4.29), where J_w is replaced by UDS(2) at the wall. Note that the value of UDS(2) at the wall is the value stored at the center of the wall-adjacent cell (as seen in Figure 35) since the face value of the derivative of UDS(0) is not available. This approximation requires the near wall mesh to be fine enough so that the mass fraction distribution, UDS(0), can treated as linear.

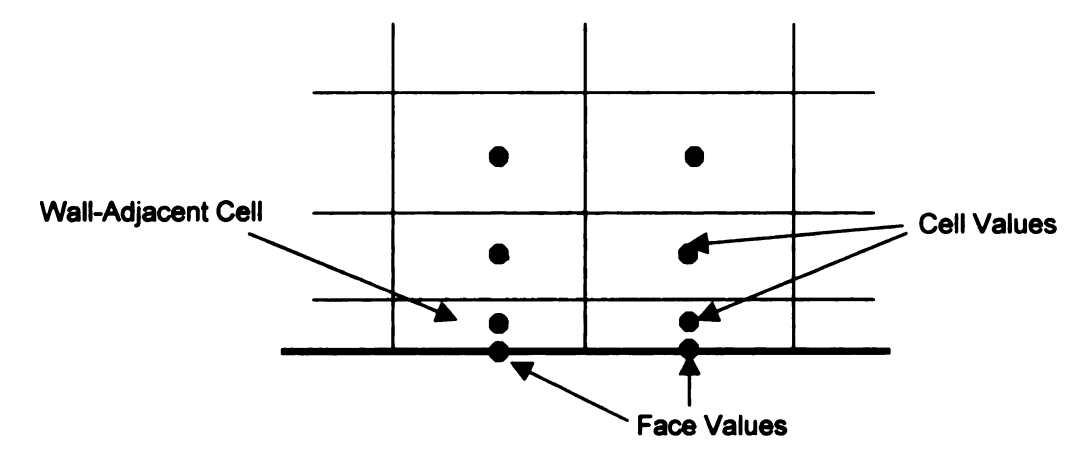


Figure 35. Illustration of Face and Cell Values

The comparison of the numerical and analytical solutions for h_m along the plate is shown in Figure 36. The ratio of the analytical solution to the numerical one is given in Figure 37.

The agreement between the analytical and numerical solutions suggests that FLUENT is an acceptable tool to perform mass transfer problem without volumetric phase change, at least for the case of laminar flow over a flat plate.

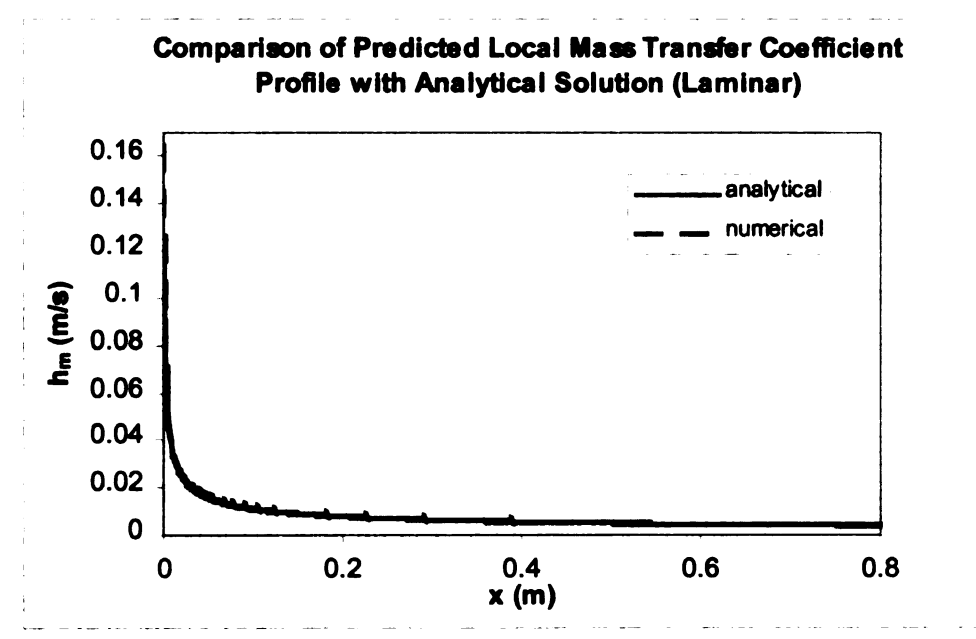


Figure 36. Comparison of Mass Transfer Coefficient (Laminar, Flat Plate)

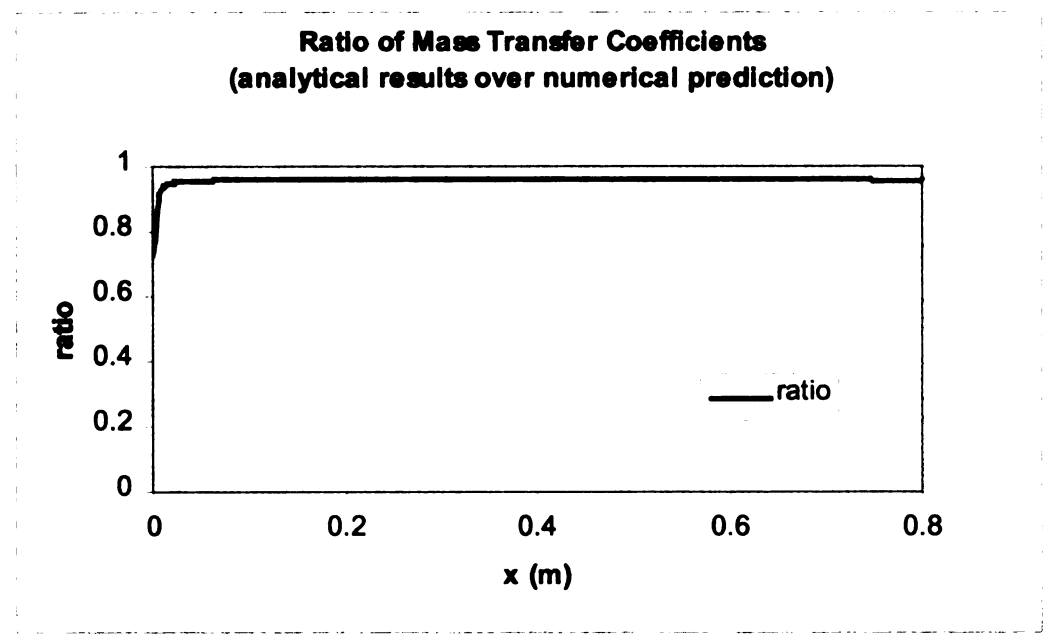


Figure 37. Ratio of Analytical to Numerical Solutions for h_m (Laminar, Flat Plate)

The Experimental Facility Case

The same surface phase change model was applied to the experimental facility.

Similar to the flat plate case, the inlet mass fraction boundary condition is obtained by equation (4.28). The mass fraction on the thermally active surface is imposed as saturated according to the surface temperature via the same UDF in Appendix E.

An important difference from the flat plate case is the treatment of the turbulence effect on the mass transfer prediction. Instead of using equation (2.10) for the laminar flow, equation (2.11) is adopted to calculate the mass flux, $J_{i',i}$, for the turbulent flow. The impact of turbulence on the mass transfer is also considered in the UDF in Appendix E. (When applied for laminar flows, the turbulence viscosity μ_t (C_MU_T(c,t) in the code) is equal to zero.) As seen in equation (2.11), the prediction of the turbulent viscosity μ_t is important for the mass transfer simulation in turbulence flows since it affects the effective mass diffusivity.

Only three cases of simulation were performed, as it is rather computationally expensive with the current hardware resources:

Case 1: The inlet temperature (approximately equal to the jet temperature) of the air-vapor mixture is 25°C with a relative humidity of 60% (the corresponding mass fraction was calculated with equations (4.27) and (4.28); the plate temperature is 5°C with saturation vapor mass fraction.

- Case 2: The inlet/jet temperature is 24°C with a relative humidity of 75%; the plate temperature is set to be 4°C with saturation vapor mass fraction.
- Case 3: The inlet/jet temperature is 25 °C with a relative humidity of
 85%; the wall temperature is 5 °C with saturation vapor mass fraction.

The velocity of the jet nozzle is 10 m/s for all three cases.

Figure 38 represents the predictions of local vapor mass flux, Jw, at the wall. Jw is also the flux of water condensed on the surface of the wall. Note that the original value of Jw is negative from the CFD code since the direction of it is out of the computational domain. The absolute value is taken in the figure as it makes more physical sense in terms of water condensed on the wall.

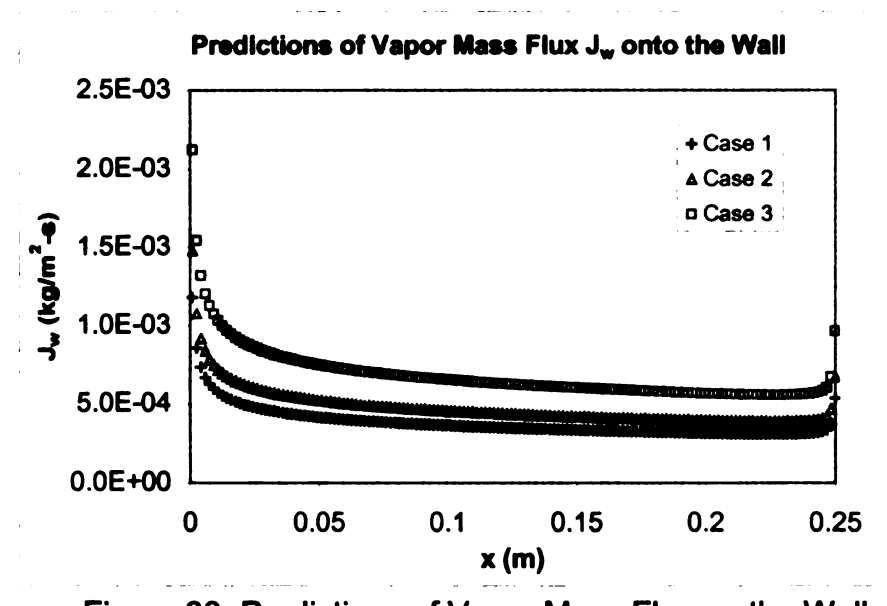


Figure 38. Predictions of Vapor Mass Flux on the Wall

The predictions of mole fraction profiles of water vapor for the three cases are included as Appendix G.

Note that with the current surface phase change model, the mole/mass fraction is predicted by the concentration equation without considering local thermodynamic equilibrium. It is possible, especially for higher inlet/jet humidity (like in Case 3), that the predicted vapor mole/mass fraction is higher than the local saturation mole/mass fraction. That is, the vapor is super cooled. The super cooling tends to happen in the near wall region where the temperature is low (possibly lower than the dew point).

To investigate the super cooling that can happen using predictions of the current model, the relative humidity profiles at the location x/w = 10.8 are obtained by dividing the predicted mole fraction profile with the saturation mole fraction profile corresponding to the predicted local temperature. As seen in Figure 39, the surface phase change model predicts super cooling in the near wall region (0 $\le y \le 3.0e-4$ m for Case 3) when the inlet/jet humidity is relatively higher (Case 3).

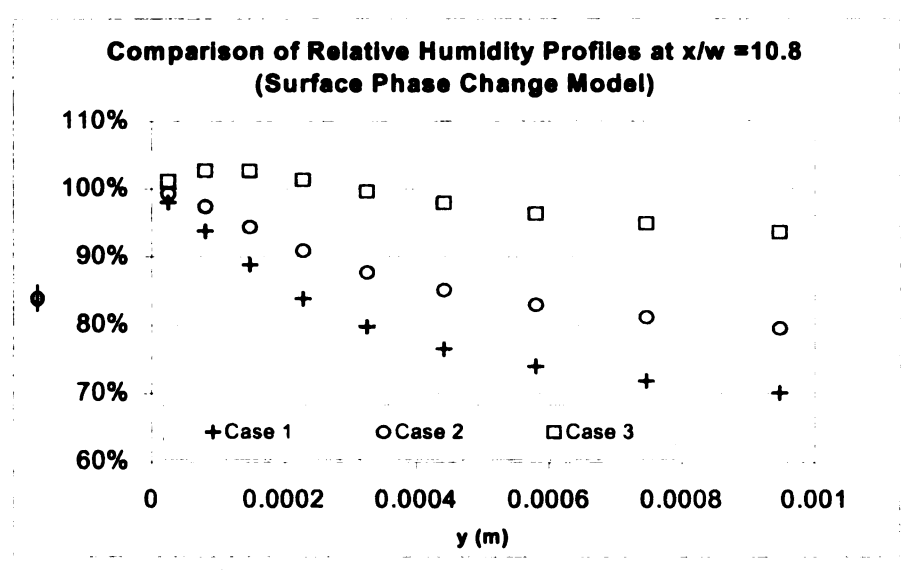


Figure 39. Comparison of Relative Humidity at x/w =10.8

However, whether the super cooling really happens in the real experiments is questionable. It is generally believed [9] [10] [11] that as the local temperature drops below the dew point, there will be water droplets formed to keep the local thermodynamic equilibrium, as will be considered later in the volumetric phase change model. The current model assumes the vapor stays in the gaseous phase even when it is super cooled.

Multiplying the averaged values of the mass flux predictions in Figure 38 $(\overline{J_w})$ by the plate area (A), the global condensation rate, \dot{m}_p , for the plate can be obtained: $\dot{m}_p = \overline{J_w} A$. To compare with experimental drip-off tests, the unit of \dot{m}_p is defined in terms of grams per minute (g/min).

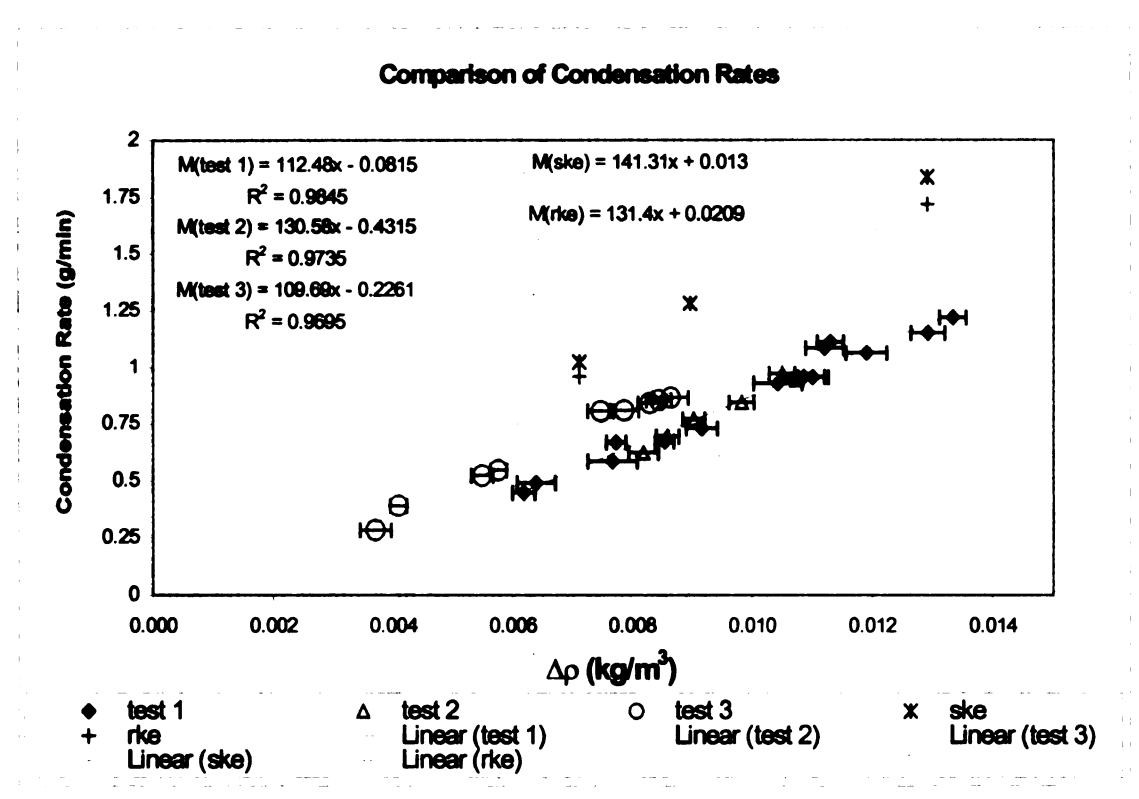


Figure 40. Comparison of Condensation Rate of the Plate

Figure 40 is the comparison of the predicted condensation rate on the plate with experimental drip-off tests. The abscissa ($\Delta \rho_{v}$, kg/m³) in the plot is the difference of vapor mass concentration between the inlet/jet and the surface of the wall. As seen in the figure, the predicted condensation rate is very linear. The intercept of the curve is very close to the origin, which suggests that as the concentration differential is zero there is no drip-off of water.

The slope of the curves have the meaning of the averaged mass transfer coefficient, \overline{h}_m , if divided by the area of the plate. The linearity of the predictions suggests that \overline{h}_m does not vary with the concentration differential so long as the jet velocity stays the same (10 m/s). As seen in the figure, the predicted slope is close to the experimental data, while the absolute values of the condensation rate are less than 20% off from the tested data. The realizable k- ϵ model gives lower condensation rates because it predicts lower turbulent viscosity. As seen in equation (2.11), a lower μ_t will result in lower predictions for the mass flux. The author offers the following possible reasons for the discrepancies in the above comparison:

The mass flux of the numerical calculation accounts for the water VAPOR that goes onto the interface between the gaseous mixture and the liquid film. It is not clear whether the total amount of vapor going through the interface will COMPLETELY condense into water liquid. If not, it may be a reason why the experimental data have lower values than the predicted ones.

- It is suspected that, experimentally, there may exist a flow transition from laminar to turbulence on the plate surface. If the flow is laminarlike at the developing region close to the jet nozzle, the mass transfer of vapor onto the plate will be reduced. However, this numerical simulation does not include the flow transition.
- Experimentally, the temperature in the area close to the edges of the plate may be higher than it is supposed to, under the influence of the ambient flow with higher temperature. This will result in higher saturation mass fraction in the corresponding area, and lower concentration difference between the main stream and the plate, which will reduce the mass flux of vapor onto the plate.
- Another possible reason for the disagreement may be the three-dimensional effects at the end of the thermally active plate. The numerical simulation is performed with a 2D model, which is an appropriate approximation close to the jet nozzle according to the experimental measurements in the z direction. But at the end of the plate, the 2D approximation was not experimentally validated. If the three-dimensional effect is significant in this region, it may be a factor that causes the disagreement.

The Sherwood number based on the slot width, $Sh = \frac{h_m w}{D}$, in a study similar to the current one was measured by Mabuchi et al [20], where h_m is the local mass transfer coefficient, w is the width of the jet nozzle, and D is the mass diffusivity. The comparison of the numerical calculations and the published data

for the turbulent case (tripped data in [20]) is shown in Figure 41. In this case, the flow is turbulent from the beginning of the wall jet, and there is no flow transition from laminar to turbulence.

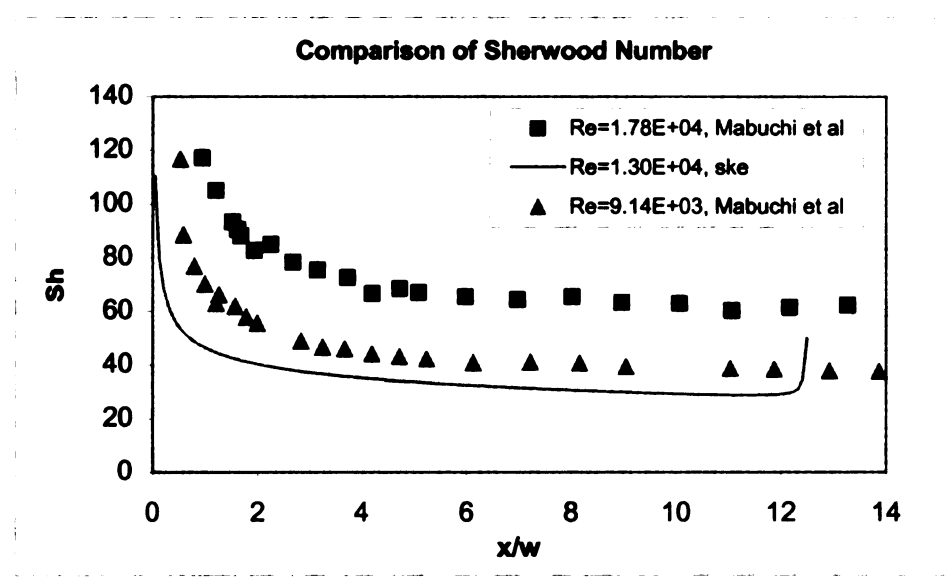


Figure 41. Comparison of Sherwood number

The possible explanation for the above comparisons is that, in the developing region of the wall jet, the Sherwood number may depend more on the velocity of the jet, U_{jet} , than on the width of the jet nozzle, w. The higher the jet velocity is, the higher the Sherwood numbers are. Although the slot width based Reynolds number for the current study (Re \cong 1.3e+4) lies between the ones in the published data, the jet velocity for all the published data (\ge 14.4 m/s) is greater than that for the current study (10 m/s).

4.3 Volumetric Phase Change Model

4.3.1 Model Analysis

The simple case of the forced convection condensation on a flat plate in the presence of a non-condensable gas situation is again employed as the example for the model illustration.

In the volumetric phase change model, the same "thin film" assumption is adopted as in the surface phase change model, which means that the liquid film on the wall has no influence on the velocity field and the heat transfer. Moreover, the impermeable surface model is still assumed valid at the interface between the liquid film and the gaseous vapor-air mixture. The computation starts from the interface where the mass fraction of vapor is saturated.

The key point of the volumetric phase change model is that the possible formation of liquid droplets (fog) in the volume of the flow is considered, which is the major difference compared to the surface phase change model. In the previous surface phase change model, the volumetric condensation is not considered, which means that the thermodynamic equilibrium is only maintained on the wall surface. Thus, there will be no phase change occurring volumetrically even if the vapor is super-cooled. However, as mentioned earlier, when the local temperature is below the dew point, it is possible that the water vapor will condense into liquid water droplets (fog) to keep local thermodynamic equilibrium in the volume of the flow. When the condensation occurs, there will be latent heat released, which will affect the temperature distribution. Meanwhile, there will be a loss (or sink) of mass in the gaseous phase as the water vapor condenses out into the liquid phase. Analytically, the condensation phenomenon will cause an additional source term (sink term for evaporation) in the energy equation, and a

sink term (source term for evaporation) in the vapor concentration equation and the overall mass continuity equation, assuming that the phase change does not affect the form of the momentum (Navier-Stokes) equations.

Note that in FLUENT, the user can not manipulate the basic forms of the governing equations. The only possibility for to the user is to use the user defined source terms in these equations.

In order to account for the impact of the volumetric phase change, the source terms in the energy, concentration, and continuity equations need to be figured out, and expressed in terms of the flow variables being solved in the governing equations.

Besides the same assumptions as in the surface phase change model, the additional assumptions in the volumetric phase change model include:

- The volume of the condensed droplets in the gaseous phase is negligible so that classical Navier-Stokes equations are still valid.
- The velocity components of gas and dispersed phases are equal.
- The temperature of the gas and the dispersed liquid phase are equal.
- There is no interaction between the droplets.

With the above assumptions, the only effects of the volumetric phase change are the additional source terms in the energy, the vapor concentration and the overall continuity equations. The fluid is still modeled as a single (gaseous) phase, dual species mixture (air and vapor) in the computation. The phase change effects are accounted for with the source terms.

To develop the source terms needed, the control volume shown in Figure 42 is considered in the gaseous phase.

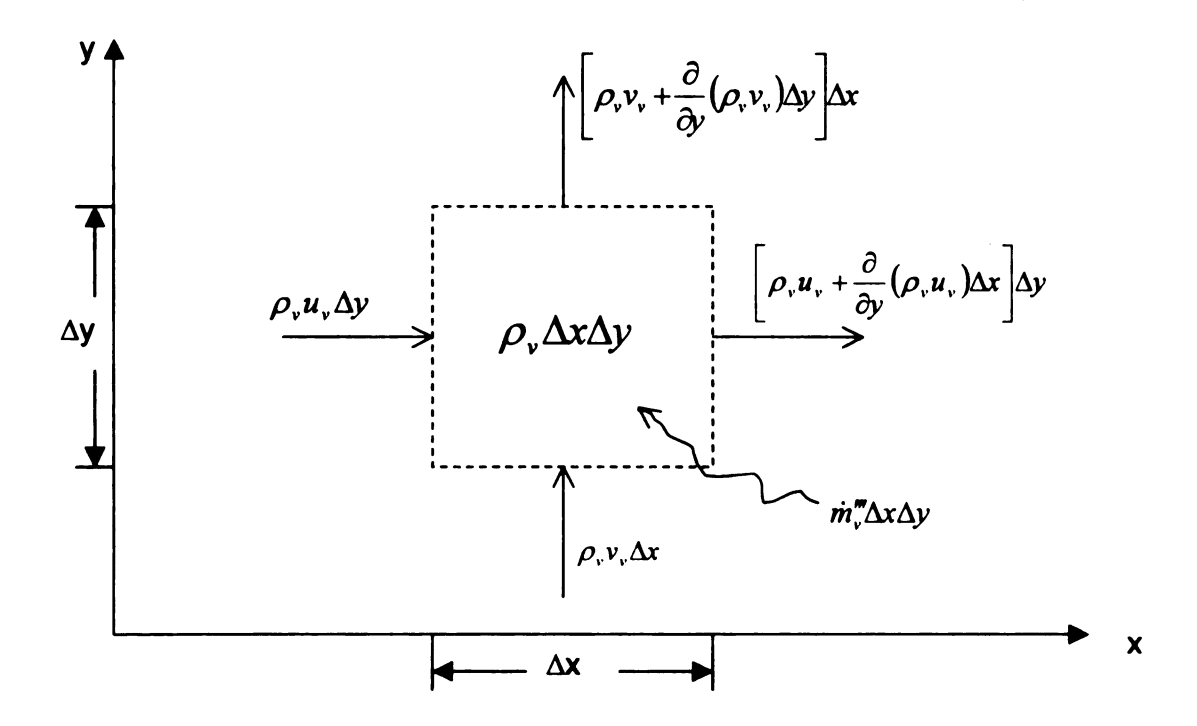


Figure 42. Control Volume for Phase Change Analysis

First, the mass conservation of water vapor is considered in the $\Delta x \Delta y$ control volume. The conservation principle is the statement that the net flow of the water vapor into the control volume must equal the rate of vapor accumulation inside the control volume [14]:

$$\frac{\partial \rho_{\nu}}{\partial t} \Delta x \Delta y = \rho_{\nu} u_{\nu} \Delta y - \left[\rho_{\nu} u_{\nu} + \frac{\partial}{\partial x} (\rho_{\nu} u_{\nu}) \Delta x + \cdots \right] \Delta y
+ \rho_{\nu} v_{\nu} \Delta x - \left[\rho_{\nu} v_{\nu} + \frac{\partial}{\partial y} (\rho_{\nu} v_{\nu}) \Delta y + \cdots \right] \Delta x + \dot{m}_{\nu}^{m} \Delta x \Delta y$$
(4.32)

The velocity components u_v and v_v refer strictly to the motion of water vapor relative to the control volume. They should be distinguished from the mass-averaged velocity components (u and v) of the bulk flow in equation (4.4).

Worth noting is that the product $\rho_v u_v$ represents the mass flux of water vapor in the x direction, per unit area normal to the x direction. The term $\dot{m}_v^{\prime\prime\prime}$ on the right hand side of equation (4.32) is the volumetric rate of the creation of the water vapor, which is also the source term, S_m , needed in the vapor concentration and overall continuity equations to account for the phase change. The vapor generation rate $\dot{m}_v^{\prime\prime\prime}$ is negative (sink) when the water vapor is consumed during the condensation process.

Also note that since the fluid in the computation accounts for the gaseous phase only, the relationship of velocity components of the individual species and that of the bulk flow represented in equation (4.4) does not hold any more. The reason is that the sum of the volumetric rates of creation for the two species (air and vapor) is not zero, but $\dot{\mathbf{m}}_{v}^{w}$.

The next step is to write the source term \dot{m}_{v}^{m} (or S_{m}) in terms of the flow variables solved in the governing equations mentioned in Chapter 2.

Dividing by $\Delta x \Delta y$ and invoking the limit $(\Delta x, \Delta y) \rightarrow 0$, the vapor conservation statement (4.32) can be reduced to

$$\dot{m}_{v}^{m} = \frac{\partial \rho_{v}}{\partial t} + \frac{\partial}{\partial x} (\rho_{v} u_{v}) + \frac{\partial}{\partial v} (\rho_{v} v_{v}) \tag{4.33}$$

Since the present study is for the steady state, the source term S_m can be written as

$$S_{m} = \dot{m}_{v}^{m} = \frac{\partial}{\partial x} (\rho_{v} u_{v}) + \frac{\partial}{\partial v} (\rho_{v} v_{v})$$
 (4.34)

Similar to the analysis for equation (4.14), the velocity components of vapor can be written as

$$u_{v} = u - \frac{\rho_{a} + \rho_{v}}{\rho_{v}} D \frac{\partial}{\partial x} \left(\frac{\rho_{v}}{\rho_{a} + \rho_{v}} \right), \quad v_{v} = v - \frac{\rho_{a} + \rho_{v}}{\rho_{v}} D \frac{\partial}{\partial y} \left(\frac{\rho_{v}}{\rho_{a} + \rho_{v}} \right)$$
(4.35)

According to the statement of the volumetric phase change model, the air and vapor are the only species in the single gaseous phase. Therefore, $\rho = \rho_v$ + ρ_a . By the definition of mass fraction in equation (4.3), equation (4.35) can be further written as

$$u_{\nu} = u - \frac{1}{\Phi_{\nu}} D \frac{\partial}{\partial x} (\Phi_{\nu}), \qquad v_{\nu} = v - \frac{1}{\Phi_{\nu}} D \frac{\partial}{\partial y} (\Phi_{\nu})$$
 (4.36)

and

$$\rho_{\nu} = \rho \Phi_{\nu} \tag{4.37}$$

Substituting equations (4.36) and (4.37) into equation (4.34), the source term S_m can be written as

$$S_{m} = \frac{\partial}{\partial x} \left[\rho \Phi_{v} \left(u - \frac{1}{\Phi_{v}} D \frac{\partial}{\partial x} (\Phi_{v}) \right) \right] + \frac{\partial}{\partial y} \left[\rho \Phi_{v} \left(v - \frac{1}{\Phi_{v}} D \frac{\partial}{\partial y} (\Phi_{v}) \right) \right]$$
(4.38)

Now, all the variables in the expression of S_m are the ones being solved by the governing equations in FLUENT. This source should go into both the vapor concentration equation (2.9) and the overall continuity equation (2.1). Term R_i in equation (2.9) drops out since there is no chemical reaction.

Accompanying the mass source term of vapor due to phase change, there is an energy source term S_h for the energy equation (2.4) to account for the latent heat released during the phase change. Apparently,

$$S_h = -LS_m \tag{4.39}$$

where L is the latent heat of water vapor, which is assumed to be a constant in the normal temperature range inside a vehicle.

4.3.2 Model Implementation

Another user defined function (UDF) was developed to implement the volumetric phase change model, which is included as Appendix H.

Introducing the condensation into the computation is accomplished by calculating the saturation mass fraction of water vapor according to the local temperature $(\Phi_v)_{sat}$ via equation (4.24), and then comparing it to Φ_v , the vapor mass fraction at the same location returned by the solver via the concentration equation (2.9) with source term S_m included. If the Φ_v is greater than $(\Phi_v)_{sat}$, it means that the vapor is super-cooled at this location. In order to keep the local thermodynamic equilibrium, Φ_v is adjusted down to the local $(\Phi_v)_{sat}$. Physically, the adjustment introduces a vapor mass sink and the release of latent heat in the volume of the flow where condensation occurs. Mathematically, the adjustment produces finite source terms S_m and S_h in the governing equations. On the other hand, if Φ_v is smaller than $(\Phi_v)_{sat}$, no adjustment is made for Φ_v , and the source terms S_m and S_h are both zeros. The solver keeps iterating to solve the governing

equations with the above-mentioned adjustment until a converged solution is reached.

In the UDF included as Appendix H, the adjustment of vapor mass fraction is made in the DEFINE_ADJUST function (macro) named as spec_grad. For comparison, the local saturation mass fraction of water vapor $(\Phi_v)_{sat}$ is stored in the user defined scalar UDS(3). The adjusted vapor mass fraction is stored in UDS(0). The vapor mass flux components $\rho_v u_v$ and $\rho_v v_v$ are stored in UDS(1) and UDS(2), respectively. Again, the purpose of storing the flow variables into a user defined scalars is to get the relative derivatives of the variables that can not be returned directly by the solver to the UDF but are necessary to specify the source terms needed in the governing equations. The cell values of the derivatives of the UDS are available to the user when developing the UDF code. None of the transport equations of the user defined scalars (UDS's) is solved.

One of the difficulties about using the UDS is that assigning the cell values for a UDS (as seen in Figure 35) does not automatically assign the face values to it. If no special assignment is made and the transport equation of the UDS is not solved, the face values will be defaulted as zeros. However, the face values of the above mentioned UDSs are very important because they actually serve as the boundary conditions for the flow variables the UDSs stand for. Therefore, the face values of the UDSs should be assigned to be consistent with the corresponding cell values.

In the current UDF, UDS(1) and UDS(2) are functions of the derivatives of UDF(0) as shown in equation (4.36). However, unlike the cell values, the face

values of the derivative of a UDS are not available to the user, which makes it difficult to specify the face values of UDS(1) and UDS(2). Although currently there is no good solution to this problem according to the technical support personnel of FLUENT, INC., the author tried two methods to work around this problem.

- (1) One is to specify the face values of UDS(1) and UDS(2) to be the same as the cell values at the wall-adjacent cells (as in the UDF of Appendix H)
- (2) the other is to extrapolate face values UDS(1) and UDS(2) with their cell value and derivatives at wall-adjacent cell (as in the UDF included as Appendix I).

4.3.3 Results and Comparisons

Unfortunately, no valuable results were obtained by the above mentioned implementation, even for the flat plate case.

Through observation of the behaviors of the residuals, the iteration is highly unstable. The residuals jump back and forth as the iteration goes on. The computational results vary from one iteration to another, and never come to a stable and converged solution.

The unstableness in method (2) of the implementation is much worse than that in method (1), which suggests the iteration is sensitive to the face values (boundary conditions) of UDS(1) and UDS(2) ($\rho_V u_V$ and $\rho_V v_V$). Although it gives better stability compared to method (2), method (1) is theoretically an incorrect way to get the face values of UDS(1) and USD(2) since the vapor mass fraction,

 Φ_{v} , on the wall surface is definitely different from that at the center of the wall-adjacent cell. Besides, as mentioned earlier, none of the ways gives stable and converged results.

4.4 Summary and Discussion

Despite the questionable assumption that no water droplets (fog) form volumetrically to keep the thermodynamic equilibrium, the practical value of the surface phase change model for defogger designs is yet to be further investigated by comparison with experimental measurements.

It is believed that the volumetric phase change model is in the conceptready stage with the theoretical analysis of the model if source terms manipulation is the way to handle the phase change problem. The author offers two possible reasons for the incompleteness of the model implementation.

- From the standpoint of model implementation, apparently imposing the boundary values of ρ_vu_v and ρ_vv_v by method (2) is still not appropriate or needs to be refined.
- Form the standpoint of the the formulation source terms, S_m and S_h are highly non-linear with respect to the flow variables solved in the governing equations, which makes the equations more difficult to solve. Since the algorithm to solve the equations is not open to the users, it is uncertain whether the algorithm is compatible with the non-linearity of the source terms.

Chapter 5

COCLUSIONS AND RECOMMENDATIONS FOR FUTURE WORK

5.1 Simulations without Phase Change

A 2D steady state simulation of the wall jet experimental facility was performed with three different turbulence models, namely, the standard k- ϵ model, the realizable k- ϵ model, and the Reynolds stress model (RSM). The two-layer zonal model was employed as the near wall treatment for all three turbulence models.

In outer scaling, the numerical results of velocity field from all three turbulence models are in good agreement with the experimental data. The standard k- ϵ model gives even better mean velocity profile predictions, especially in the relatively well-developed region of the jet. In addition, it gives better match of the y_m/δ_2 prediction to the experimental measurements compared to the other two models. The Reynolds stress model (RSM) provides better predictions for the turbulence fluctuations. It is not generally expected that the standard k- ϵ model (or the any version of k- ϵ model) will out perform the RSM in predicting the mean velocity profiles. The reason for the unexpected model performance in the current study is not clear.

In inner scaling, the numerical results of the velocity field by the different models are virtually identical in the near wall region (y^+ < 100), but all the

predictions for the mean velocity are quantitatively smaller than the experimental data.

The temperature simulation results of different turbulence models are virtually identical, and in good agreement with the experimental test in outer scaling. In inner scaling, the predictions for the mean temperature profiles are lower than the experimental data.

Compared to the measurements, the velocity and temperature predictions in the developing region ($x/w \le 7.62$) are not as good as that in the well developed region ($x/w \ge 10$) since the turbulence models were originally developed for fully developed turbulent flows. For a simulation with a commercial CFD code, there is little room for improvement of predictions unless more suitable models for developing turbulent flows appear.

5.2 Simulations with Phase Change

Two phase change models (surface and volumetric) were developed to simulate the mass transfer of water vapor to the cooled wall of a wall jet.

The surface phase change model is realizable from the viewpoint of implementation, and is computationally stable as no user defined source terms were introduced in the governing equations. The shortcoming of this model is the questionable assumption that the phase change ONLY occurs on the wall surface, which may be one of the reasons for the discrepancy between the numerical prediction and experimental drip-off test data. Numerically, the validation of this model needs to be further investigated in the following range:

- The validation of the impermeable surface model mentioned in Chapter
 4, which makes the mass transfer completely analogous to the heat
 transfer.
- The limits on velocity, temperature, and vapor concentration conditions in order for the key assumption of the model to hold.

The volumetric phase change model is believed to be in a concept-ready state. Several possible reasons may account for the incompleteness of the model implementation with the commercial code. Further work is needed:

- It is difficult to implement the volumetric model even with the aid of the user defined function. If feasible at all, the user defined function for the model implementation needs to be further refined and improved in a much deeper level with the technical support from FLUENT, INC..
- The validation of the impermeable surface model may play an even more important role in the volumetric phase change model compared to the surface phase change model, noting it is not exactly the correct boundary condition for velocity on the interface.
- The possible investigation of the compatibility between the algorithm of the code and the highly nonlinear source terms.

For both the surface and volumetric models, the impact of the turbulence viscosity prediction on the vapor mass transfer, and the possible flow transition from laminar to turbulent on the wall may be interesting for future studies.

Although there may exist plenty of room for development from the users' side, as a commercially available software, the current version of FLUENT is not

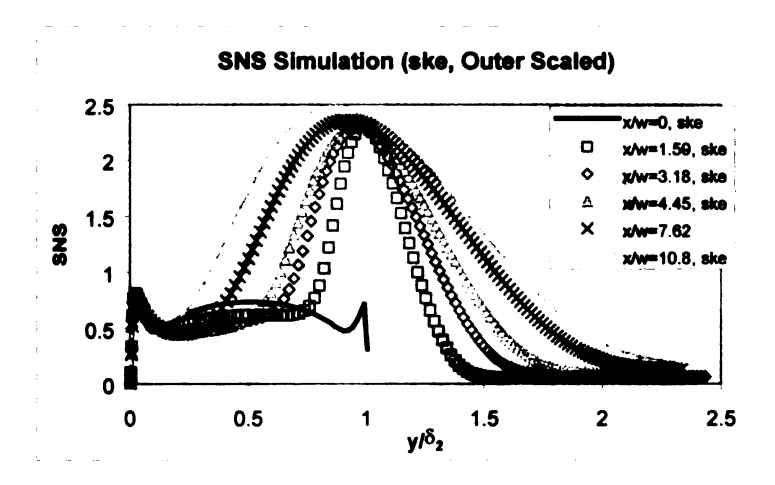
developed enough to handle the mass transfer simulation with phase change. If possible for the algorithm of the code, it would be beneficial to the users if the code

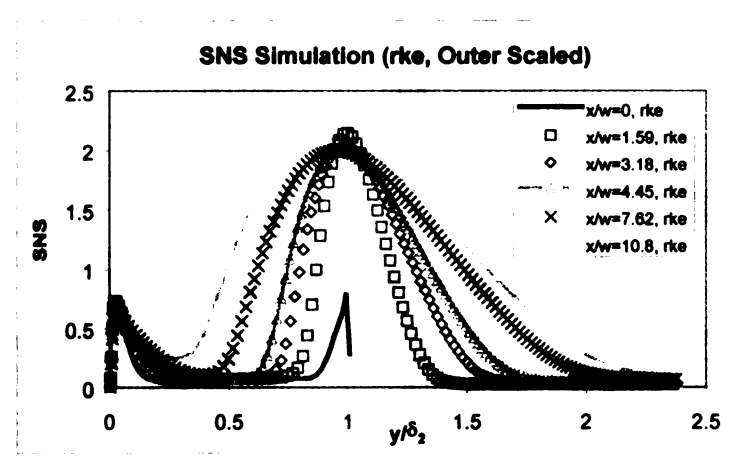
- has the velocity components of each individual species available so that the user can both specify them as boundary conditions (v_v at the wall equals zero for the current case) and use them in user defined source terms:
- has the gradients of the all the flow variables solved in the governing equations available in the user defined functions;
- allows the user to specify the movement of the wall with user defined functions;
- automatically assigns the face value of a user defined scalar consistent with its cell value when the transport equation of the scalar is not being solved.

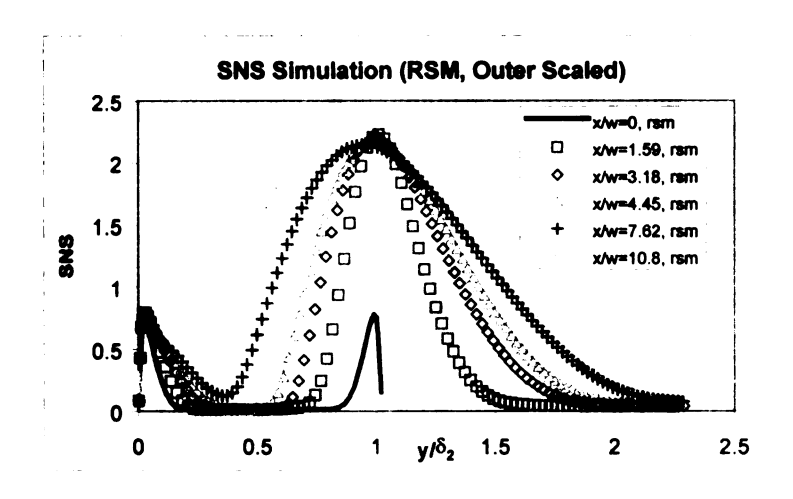
APPENDICES

APPENDIX A

SIMULATIONS OF OUTER-SCALED SNS

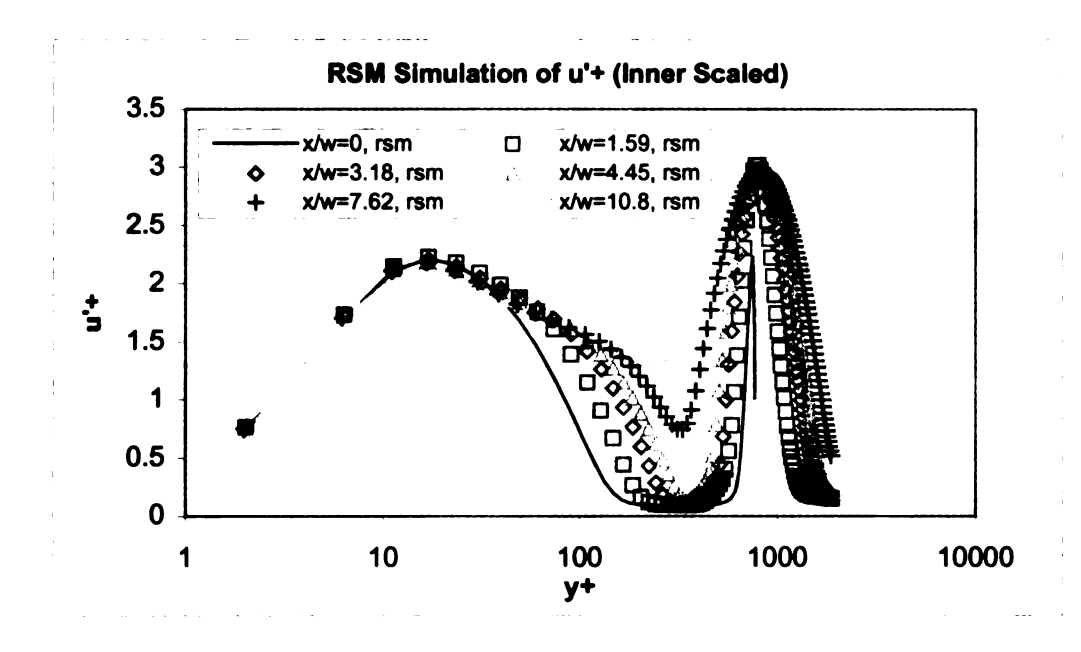


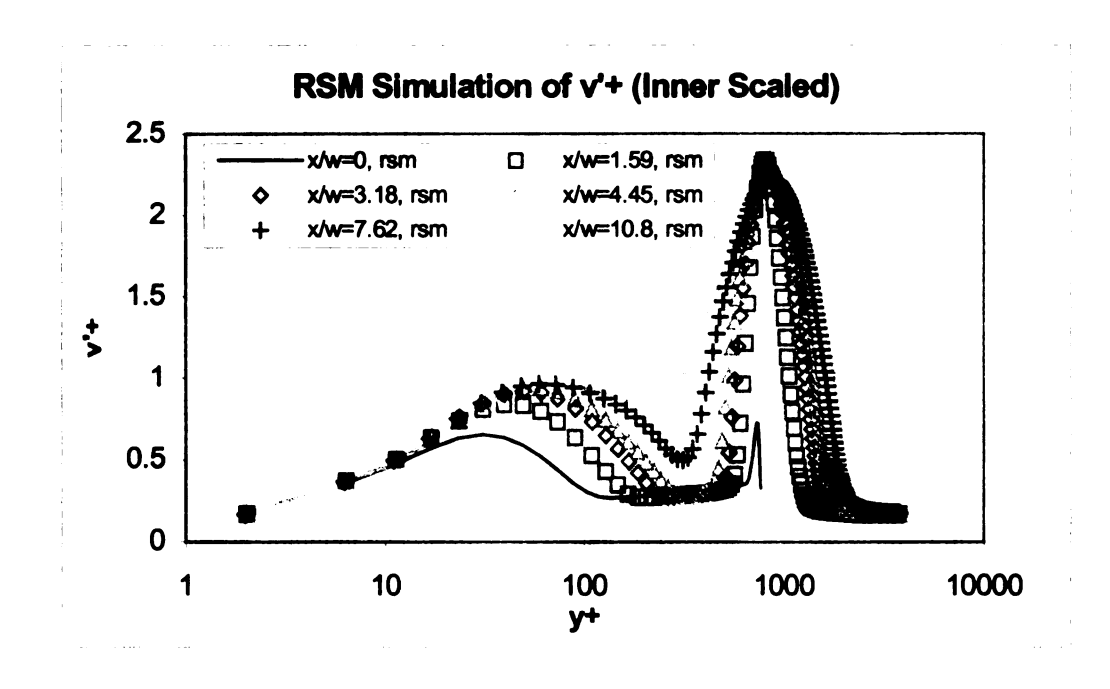


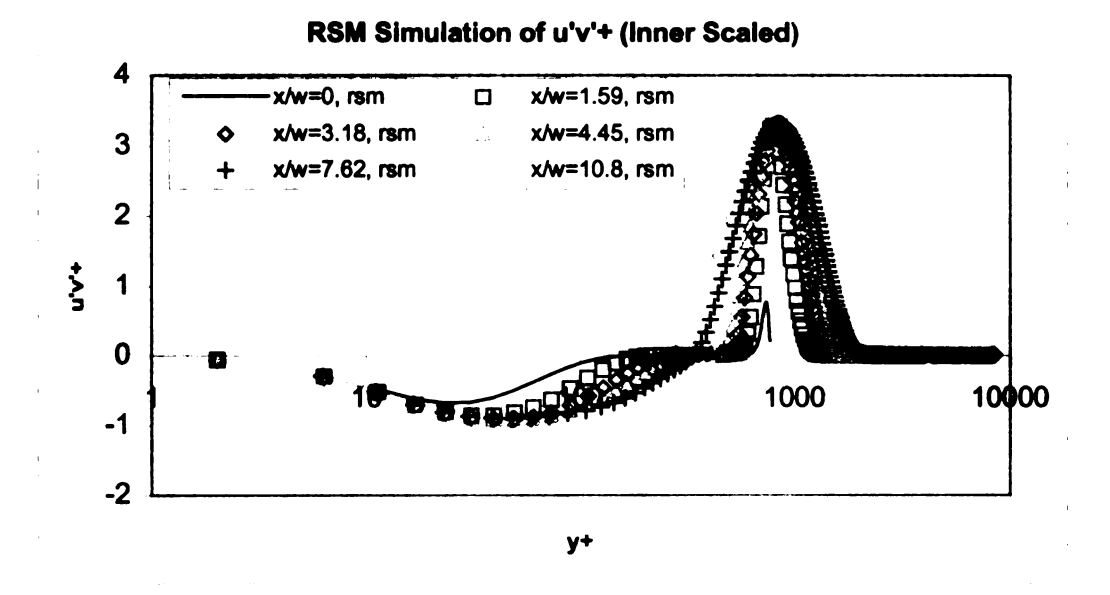


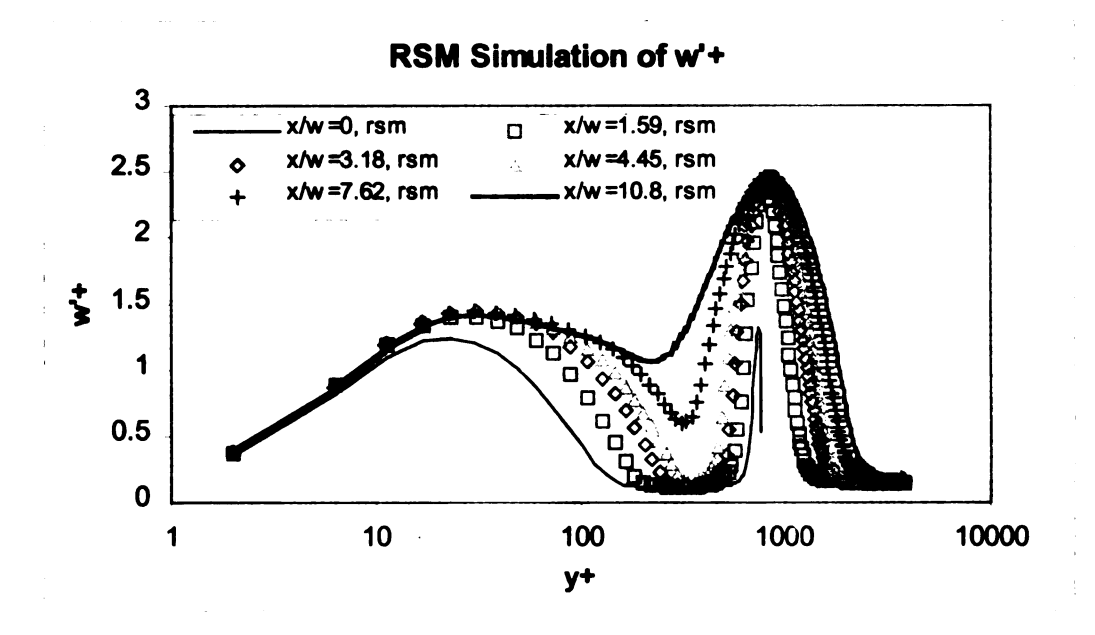
APPENDIX B

SIMULATIONS OF INNER-SCALED FLUCTUATIONS WITH RSM



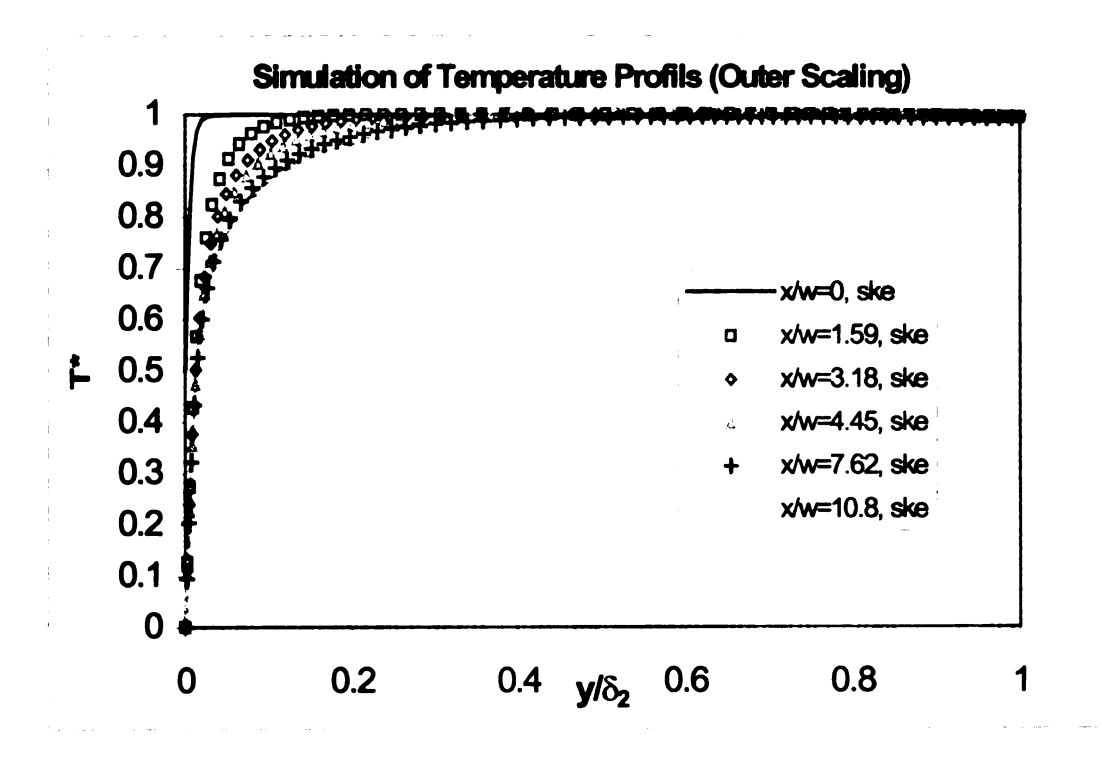






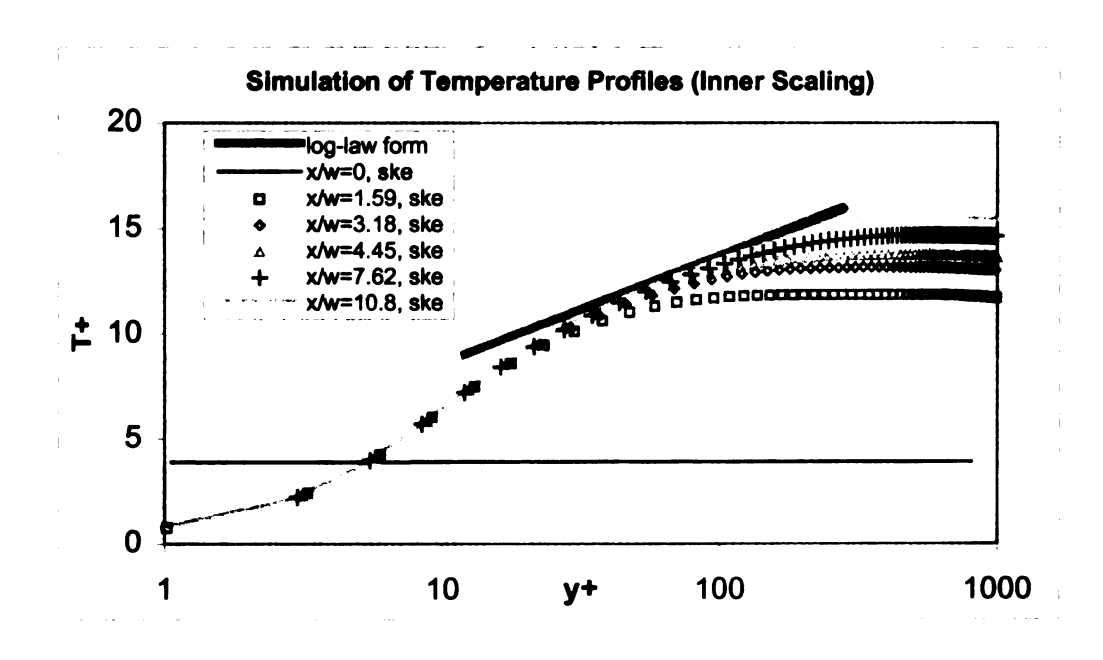
APPENDIX C

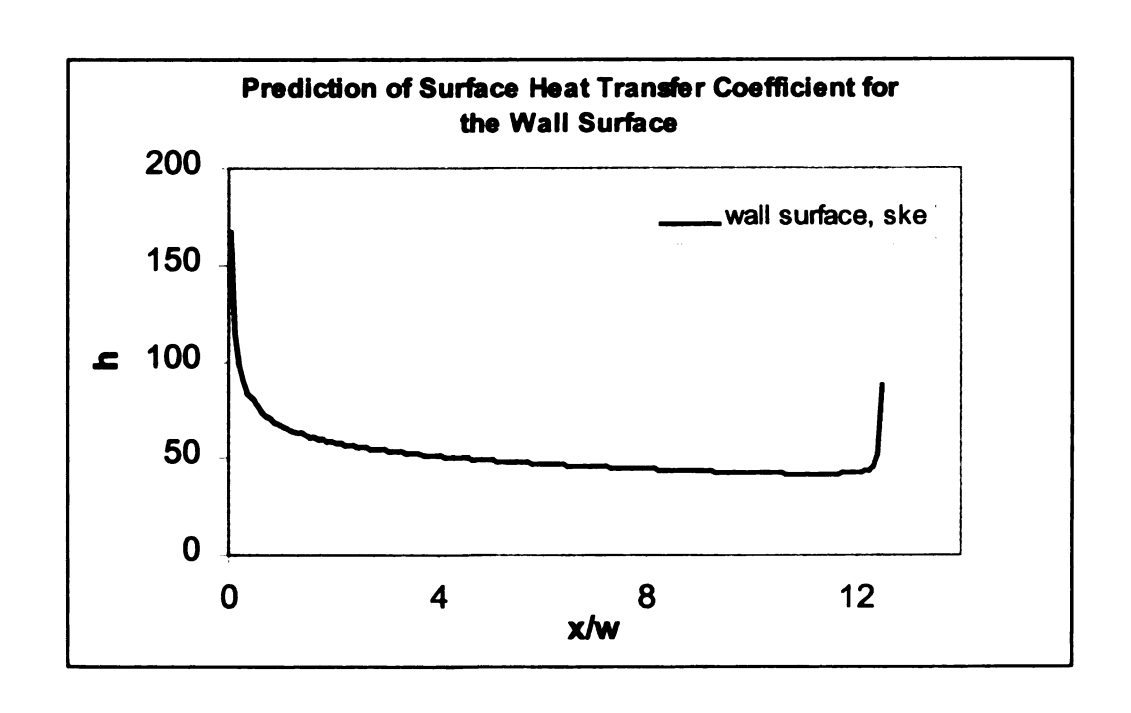
SIMULATION OF TEMPERATURE PROFILS (OUTER SCALING)



APPENDIX D

SIMULATION OF THE INNER-SCALED TEMPERATURE PROFILE AND THE HEAT TRANSFER COEFFICIENT





APPENDIX E

UDF TO IMPOSE SATURATION MASS FRACTION AS BOUNDARY CONDITION AND CALCULATE THE VAPOR MASS FLUX

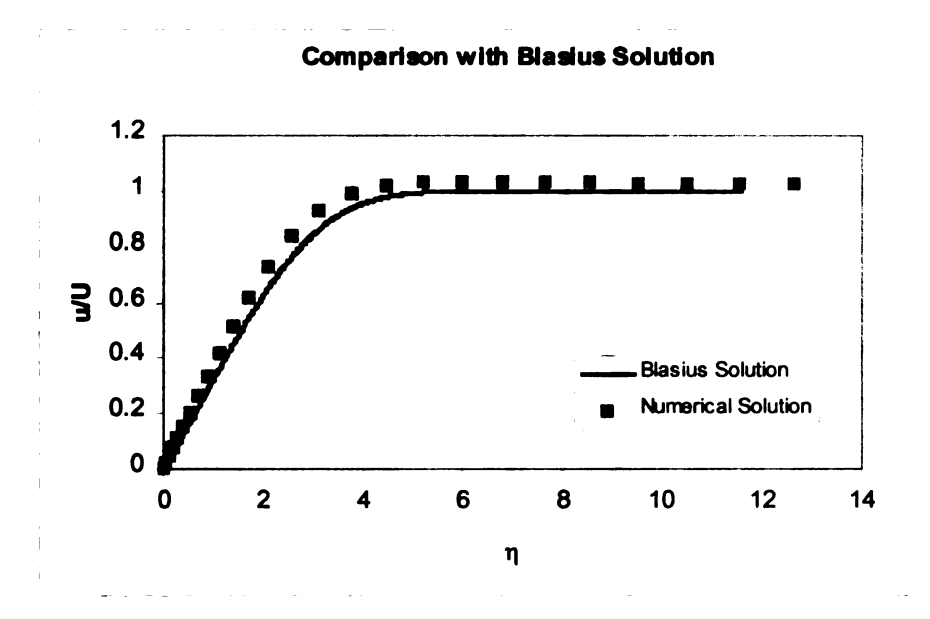
(SURFACE PHASE CHANGE MODEL)

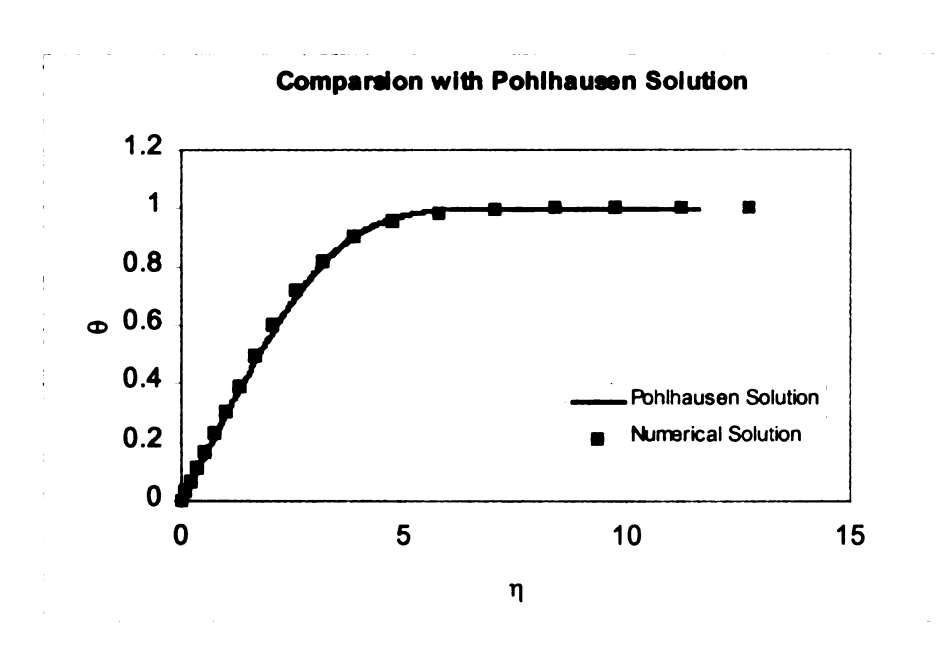
```
#include "udf.h"
#define L 2400.0e3 /* latent heat of water [J/kg] */
#define b L*18 / 8314.4
\#define \ a \ b / (273.15 + 100.)
DEFINE ADJUST(spec grad, domain)
/* This function assigns the saturated mole fraction of
  vapor to UDSI(1), and calculated mass fraction of
  vapor to UDSI(0) */
{
      Thread *t;
      cell t c;
      face t f;
      thread_loop_c (t,domain)
            begin c loop_all (c,t)
                  float MLFS = \exp(a - b / C T(c,t));
                  if (NULL != THREAD STORAGE(t, SV UDS I(1)) &&
                         NULL != THREAD STORAGE(t,SV UDS I(0)))
                         C UDSI(c, t, 1) = MLFS;
                         C\_UDSI(c,t,0) = C\_YI(c,t,0);
                   }
            end_c_loop_all (c,t)
      }
      thread_loop_f (t,domain)
            if (NULL != THREAD STORAGE(t, SV UDS I(1)) &&
                  NULL != THREAD STORAGE(t, SV UDS I(0)))
            {
                  begin_f_loop (f,t)
                         float FMLFS = \exp(a - b / F T(f,t));
                         F UDSI(f,t,1) = FMLFS;
                         F_{UDSI}(f,t,0) = F_{YI}(f,t,0);
                   end f loop (f,t)
```

```
}
      }
      thread_loop_c (t,domain)
      /* Stores the y direction mass flux
        of vapor in UDS(2) */
            begin_c_loop_all (c,t)
                  if (NULL != THREAD STORAGE(t,SV UDS I(0)) &&
                         NULL != T STORAGE R NV(t,SV UDSI G(0)))
                  {
                         float diff eff = 2.88e-5 +
                                             C MU T(c,t)/0.7;
                         C\_UDSI(c,t,2) = -C\_R(c,t)* diff\_eff*
                                              C_UDSI_G(c,t,0)[1];
                  }
            end_c_loop_all (c,t)
      }
}
DEFINE_PROFILE(plate_mf, t, position)
/* This function specifies the concentration profile of
   water vapor as saturated on boundary wall surface
   according to the local surface temperature. */
{
      face t f;
      begin_f_loop (f,t)
            float FMLFS = exp(a - b / F T(f,t));
            F_PROFILE(f,t,position) = (FMLFS * 18./29.) /
            (\overline{1}. - FMLFS * (1. - 18./29.));
      end_f_loop (f,t)
}
```

APPENDIX F

COMPARISON OF NUMERICAL PREDITION WITH THE SIMILARITY SOLUTION (LAMINAR FLOW, FLAT PLATE)

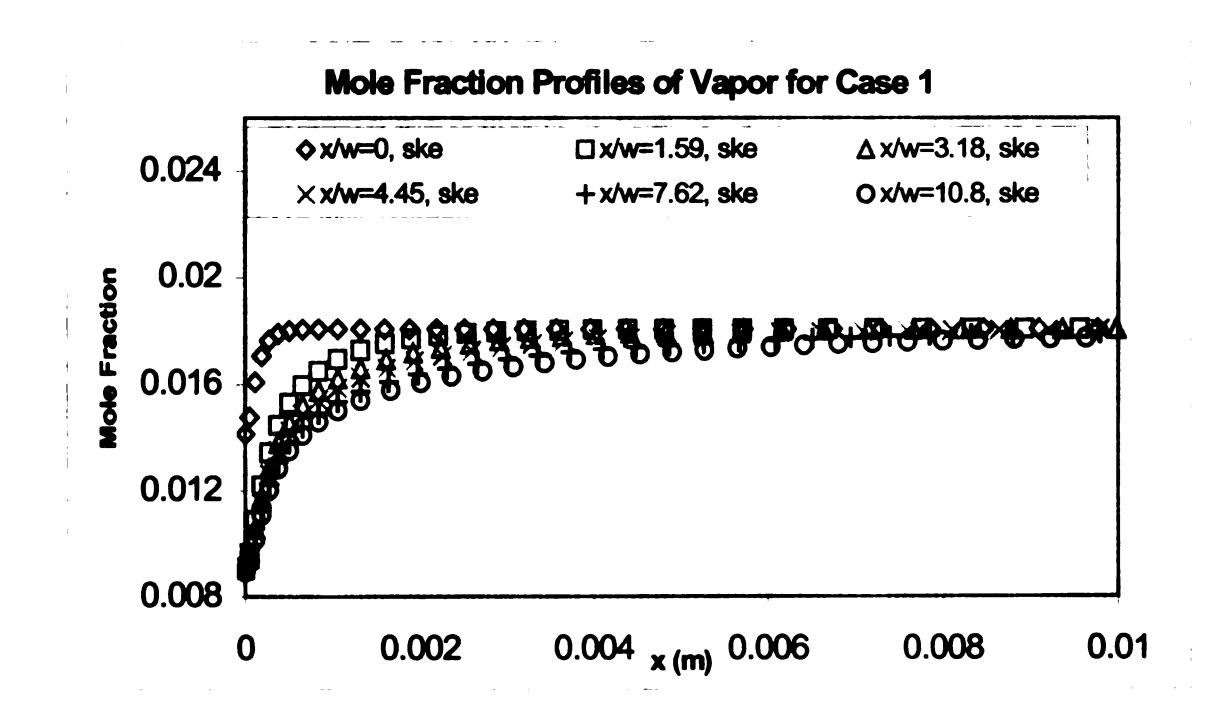




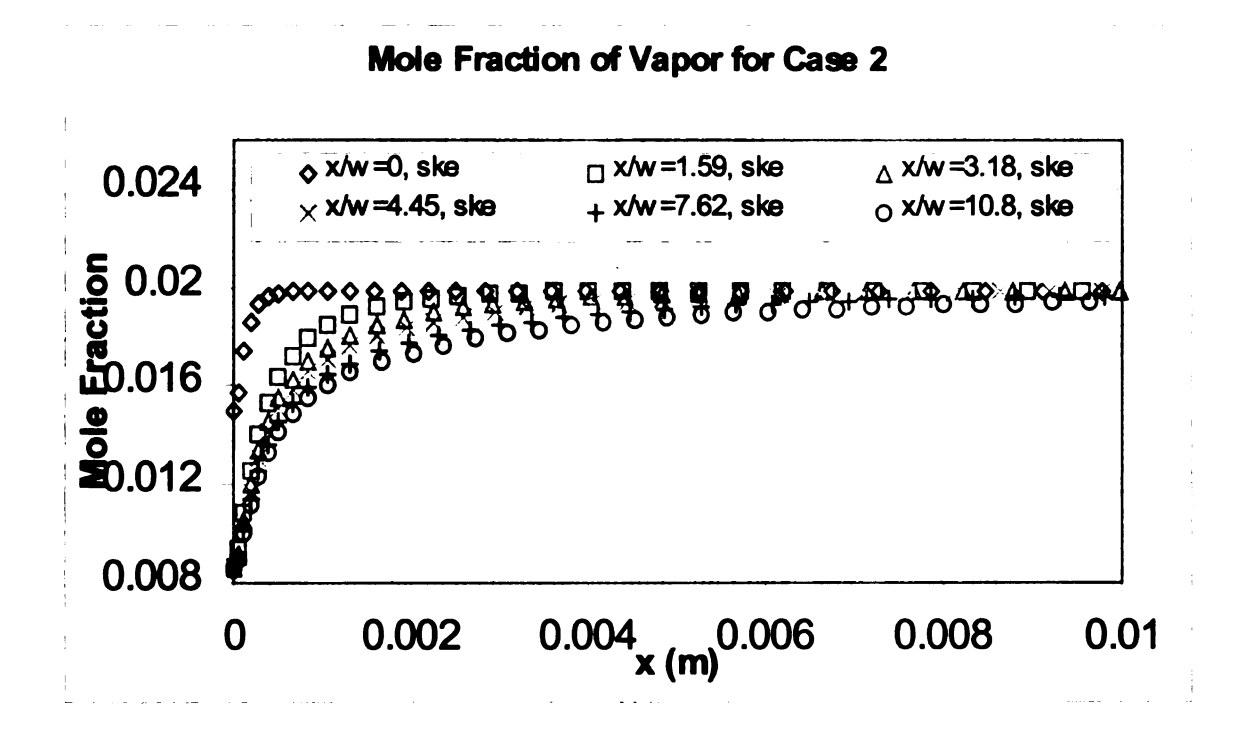
APPENDIX G

PREDICTION OF MOLE FRACTION PROFILES OF WATER VAPOR BY THE SURFACE PHASE CHANGE MODEL

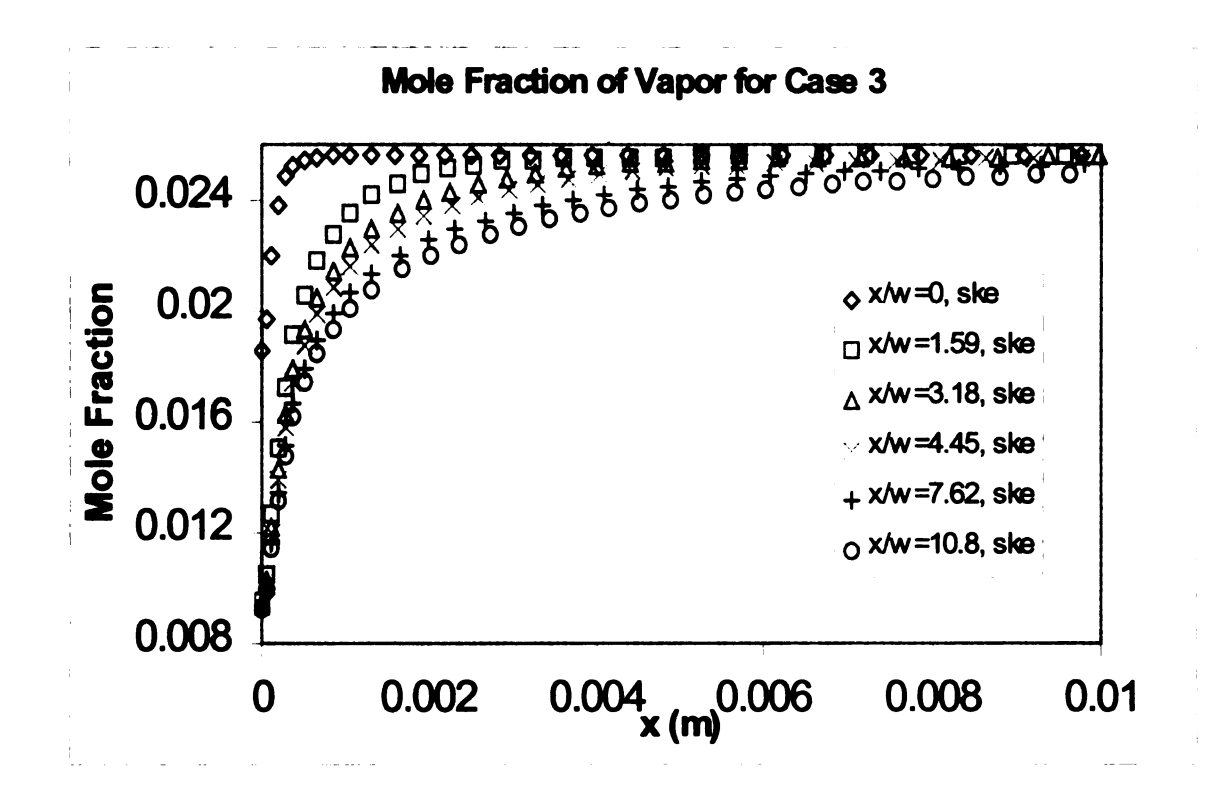
Case 1:



Case 2:



Case 3:



APPENDIX H

USER DEFINED FUNCTION FOR THE VOLUMETRIC PHASE CHANGE MODEL (METHOD (1))

```
#include "udf.h"
#include "sg.h"
#define L 2400.0e3 /* latent heat of water [J/kg] */
#define b L*18 / 8314.4
\#define \ a \ b / (273.15 + 100.)
DEFINE ADJUST(spec grad, domain)
      Thread *t;
      cell_t c;
      face t f;
      float MLFS; /* saturation mole fraction */
      float MSFS; /* saturation mass fraction */
      float UVPR; /* x velocity of vapor */
      float VVPR; /* y velocity of vapor */
      thread loop c (t, domain)
            begin_c_loop_all (c,t)
                   MLFS = exp(a - b / C_T(c,t));
                         /* equation (4.23) */
                   MSFS = (MLFS * 18./29.) / (1. - MLFS * 18./29.) / (1. - MLFS * 18./29.)
                   (1. - 18./29.));
                         /* equation (4.24) */
                   if (C_YI(c,t,0) > MSFS) C_YI(c,t,0) = MSFS;
                   if (C_YI(c,t,0) <= 0.0)
                         C YI(c,t,0) = 1.0e-12;
                   /* adjust the mass fraction of vapor if it is
                   higher than the saturation value. */
                   if (NULL != THREAD STORAGE(t,SV UDS I(3)) &&
                         NULL != THREAD STORAGE(t,SV UDS I(0)))
                   {
                         C_{UDSI}(c,t,3) = MSFS;
                         C\_UDSI(c,t,0) = C\_YI(c,t,0);
                   }
            end_c_loop_all (c,t)
      }
```

```
thread loop f (t, domain)
      if (NULL != THREAD STORAGE(t, SV UDS I(3)) &&
            NULL != THREAD_STORAGE(t,SV_UDS_I(0)))
      {
            begin f loop (f,t)
                  float FMLFS = \exp(a - b / F T(f,t));
                  float FMSFS = (FMLFS * 18./29.) /
                   (1. - FMLFS * (1. - 18./29.));
                  F UDSI(f,t,3) = FMSFS;
                  F_UDSI(f,t,0) = F_YI(f,t,0);
            end_f_loop (f,t)
thread_loop_c (t,domain)
      if (NULL != THREAD STORAGE(t, SV UDS I(0)) &&
            NULL != T_STORAGE_R_NV(t,SV_UDSI_G(0)))
      {
            begin c loop all (c,t)
                  float diff_eff = 2.88e-5 +
                                           (C MU T(c,t)/0.7);
                  UVPR = C U(c,t) - diff eff *
                        C UDSI G(c,t,0)[0]/C UDSI(c,t,0);
                  VVPR = C_V(c,t) - diff_eff *
                        C\_UDSI\_G(c,t,0)[1]/C\_UDSI(c,t,0);
                  C\_UDSI(c,t,1) = C\_R(c,t) * C\_UDSI(c,t,0)
                                      * UVPR;
                  C\_UDSI(c,t,2) = C\_R(c,t) * C\_UDSI(c,t,0)
                                      * VVPR;
            end_c_loop_all (c,t)
      }
thread_loop_f (t,domain)
/* assign face value with way (1) */
      if (NULL != THREAD_STORAGE(t,SV_UDS_I(0)) &&
            NULL != THREAD STORAGE(t, SV UDS I(1)) &&
            NULL != THREAD STORAGE(t, SV UDS I(2)))
      {
            begin_f_loop (f,t)
                  cell_t cell = F_CO(f,t);
                  Thread *c_thread = THREAD_TO(t);
```

```
if (NULL !=
                         T_STORAGE_R_NV(c_thread,SV_UDSI_G(0)))
                               F UDSI(f,t,1) =
                                           C_UDSI(cell,c_thread,1);
                               F_{UDSI}(f,t,2) =
                                           C UDSI(cell, c thread, 2);
                         }
                  end_f_loop (f,t)
            }
      }
}
DEFINE PROFILE (plate mf, t, position)
/* specify saturation mass fraction at the boundary */
      face t f;
      begin_f_loop (f,t)
            float FMLFS = exp(a - b / F_T(f,t));
            F PROFILE(f,t,position) = (FMLFS * 18./29.) /
                                     (1. - FMLFS * (1. - 18./29.));
      end f loop (f,t)
}
DEFINE SOURCE (mass src, c, t, dS, eqn)
/* source term of continuity and concentration equation */
  float source;
      if (NULL != T STORAGE_R_NV(t,SV_UDSI_G(1)) &&
              NULL != T STORAGE R NV(t, SV UDSI G(2)) &&
              NULL != THREAD STORAGE(t, SV UDS I(0)) &&
              NULL != THREAD STORAGE(t,SV_UDS_I(3)))
        {
              if (C UDSI(c,t,0) < C UDSI(c,t,3))
                    source = 0.;
              else
                    source = C UDSI G(c,t,1)[0] +
                               C_UDSI_G(c,t,2)[1];
                         /* equation (4.34) */
  dS[eqn] = 0;
  return source;
}
DEFINE_SOURCE(energy_src, c, t, dS, eqn)
/* source term for energy equation */
  float source;
      if (NULL != T STORAGE R NV(t,SV UDSI G(1)) &&
```

APPENDIX I

USER DEFINED FUNCTION FOR THE VOLUMETRIC PHASE CHANGE MODEL (METHOD (2))

```
#include "udf.h"
#include "sq.h"
#define L 2500.0e3 /* latent heat of water [J/kg] */
#define b L*18 / 8314.4
\#define \ a \ b / (273.15 + 100.)
DEFINE ADJUST(spec_grad, domain)
      Thread *t;
      cell_t c;
      face_t f;
      float MLFS;
      float MSFS;
      float UVPR;
      float VVPR;
      thread_loop_c (t,domain)
            begin_c_loop_all (c,t)
                  MLFS = exp(a - b / C_T(c,t));
                  MSFS = (MLFS * 18./29.) / (1. - MLFS *
                           (1. - 18./29.));
                  if (C_YI(c,t,0) > MSFS) C_YI(c,t,0) = MSFS;
                  if (C YI(c,t,0) \le 0.0)
                                            C_{YI}(c,t,0) = 1.0e-12;
                  if (NULL != THREAD_STORAGE(t,SV_UDS_I(3)) &&
                        NULL != THREAD STORAGE(t,SV UDS I(0)))
                  {
                        C UDSI(c,t,0) = C YI(c,t,0);
                        C_UDSI(c,t,3) = MSFS;
            end_c_loop_all (c,t)
      }
      thread_loop_f (t,domain)
            if (NULL != THREAD STORAGE(t, SV UDS I(3)) &&
                  NULL != THREAD_STORAGE(t,SV_UDS_I(0)))
            {
```

```
begin_f_loop (f,t)
                  float FMLFS = exp(a - b / F_T(f,t));
                  float FMSFS = (FMLFS * 18./29.) /
                               (1. - FMLFS * (1. - 18./29.));
                  F_{UDSI}(f,t,0) = F_{YI}(f,t,0);
                  F UDSI(f,t,3) = FMSFS;
            end f loop (f,t)
      }
}
thread loop c (t, domain)
            if (NULL != THREAD STORAGE(t,SV UDS I(0)) &&
            NULL != T STORAGE R NV(t, SV UDSI G(0)))
            {
                  begin c loop all (c,t)
                  float diff_eff = 2.88e-5 +
                                            (C MU T(c,t)/0.7);
                  UVPR = C_U(c,t) - diff_eff *
                         C UDSI G(c,t,0)[0]/C_UDSI(c,t,0);
                  VVPR = C_V(c,t) - diff_eff *
                         C\_UDSI\_G(c,t,0)[1]/C\_UDSI(c,t,0);
                  C\_UDSI(c,t,1) = C\_R(c,t) * C\_UDSI(c,t,0)
                                      * UVPR;
                  C\_UDSI(c,t,2) = C\_R(c,t) * C\_UDSI(c,t,0)
                                      * VVPR;
            end_c_loop_all (c,t)
      }
}
thread loop f (t, domain)
/* assign the face value with way (2) */
      if (NULL != THREAD STORAGE(t,SV UDS I(1)) &&
            NULL != THREAD STORAGE(t, SV UDS I(2)))
      {
            begin_f_loop (f,t)
                  cell t cell = F CO(f,t);
                  Thread *c thread = THREAD TO(t);
                   if (NULL !=
                  T STORAGE R NV(c thread, SV UDSI G(1))
                   && NULL !=
                   T_STORAGE_R_NV(c_thread,SV UDSI G(2)))
                         if (THREAD_ID(t) == 2)
```

```
float xf[ND ND], xc[ND ND],
                                           ds[ND ND], dn;
                                     F CENTROID(xf,f,t);
                                     C CENTROID(xc,cell,c_thread);
                                     NV VV(ds, =, xf,-,xc);
                                     dn = NV MAG(ds);
                                     F UDSI(f,t,1) =
C UDSI(cell,c thread,1) - dn * C UDSI G(cell,c_thread,1)[1];
                                     F UDSI(f,t,2) =
C UDSI(cell,c thread,2) - dn * C UDSI G(cell,c thread,2)[1];
                               }
                               else
                               {
                                     F UDSI(f,t,1) = 0.;
                                     F_UDSI(f,t,2) = 0.;
                         }
                  end f loop (f,t)
            }
      }
      thread loop c (t, domain)
      /* store y mass flux in UDS(4) */
            begin_c_loop_all (c,t)
                  if (NULL != THREAD STORAGE(t, SV_UDS_I(0)) &&
                         NULL != T STORAGE R NV(t, SV_UDSI_G(0)))
                   {
                         float diff eff = 2.88e-5 +
                                                  (C_MU_T(c,t)/0.7);
                         C UDSI(c,t,4) = - C_R(c,t) * diff_eff *
                                              C UDSI G(c,t,0)[1];
            end c loop all (c,t)
      }
}
DEFINE PROFILE(plate mf, t, position)
{
      face_t f;
      begin_f_loop (f,t)
            float FMLFS = exp(a - b / F_T(f,t));
            F PROFILE(f,t,position) = (FMLFS * 18./29.) /
                                     (1. - FMLFS * (1. - 18./29.));
      }
```

```
end f_loop (f,t)
}
DEFINE SOURCE (mass_src, c, t, dS, eqn)
  float source;
      if (NULL != T STORAGE R NV(t,SV_UDSI_G(1)) &&
              NULL != T_STORAGE_R_NV(t,SV_UDSI_G(2)) &&
              NULL != THREAD STORAGE(t, SV UDS I(0)) &&
              NULL != THREAD STORAGE(t, SV_UDS_I(3)))
        {
              if (C_UDSI(c,t,0) < C_UDSI(c,t,3))</pre>
                     source = 0.;
              else
                     source = C_UDSI_G(c,t,1)[0] +
                                C_UDSI_G(c,t,2)[1];
  dS[eqn]=0;
  return source;
}
DEFINE SOURCE(energy_src, c, t, dS, eqn)
  float source;
      if (NULL != T STORAGE_R_NV(t,SV_UDSI_G(1)) &&
              NULL != T_STORAGE_R_NV(t,SV_UDSI_G(2)) &&
              NULL != THREAD STORAGE(t, SV UDS I(0)) &&
              NULL != THREAD_STORAGE(t,SV_UDS_I(3)))
        {
              if (C_UDSI(c,t,0) < C_UDSI(c,t,3))</pre>
                     source = 0.;
              else
                     source = -L * (C_UDSI_G(c,t,1)[0] +
                                       C UDSI_G(c,t,2)[1]);
  dS[eqn]=0;
  return source;
}
```

LIST OF REFERENCES

LIST OF REFERENCES

- [1] Hoke, P. B. (1998). EXPERIMENTAL MEASUREMENT OF SLIT RESPONSE FUNCTION AND CORRECTION APPLIED TO INFRARED THERMOGRAPHIC MEASUREMENTS, Thesis for MS degree, Department of Mechanical Engineering, Michigan State University.
- [2] Launder, B. E. and Rodi, W. (1981). THE TURBULENT WALL JET, Prog. Aerospace Sci., Vol.19, pp.81-128.
- [3] Schwarz, W. H. and Cosart, W. P. (1961). THE TWO-DIMENSIONAL TURBULENT WALL JET, Journal of Fluid Mechanics, Vol. 10, pp.481-495.
- [4] Kruke, V. and Eskinazi, S. (1964). THE WALL-JET IN A MOVING STREAM, Journal of Fluid Mechanics Vol. 20, pp. 555-579.
- [5] Wygnanski, I., Katz, Y. and Horev, E. (1992). ON THE APPLICABILITY OF VARIOUS SCALING LAWS TO THE TURBULENT WALL JET, J. Fluid Mech., vol. 234, pp. 669-690.
- [6] Potter, M. and Foss, J. (1982). FLUID MECHANICS, pp. 422, Great Lakes Press, Inc.
- [7] Eriksson, J. G., Karlsson, R. I. and Persson, J. (1998). AN EXPERIMENTAL STUDY OF A TWO-DIMENSIONAL PLANE TURBULENT WALL JET, Experiments in Fluids 25, pp. 50-60.
- [8] Sparrow, E. M., Minkowycz, W. J. and Saddy, M. (1967). FORCED CONVECTION CONDENSATION IN THE PRESENCE OF NONCONDENSABLES AND INTERFACIAL REISISTANCE, Int. J. Heat Mass Transfer Vol. 10, pp. 1829-1845
- [9] Hijikata, K. and Mori, Y (1973). FORCED CONVECTIVE HATE TRANSFER OF A GAS WITH CONDENSING VOPOUR AROUND A FLAT PLATE, Heat Transfer-Jap. Res. 2, pp. 81-101.

- [10] Legay-Desesquelles, F. and Prunet-Foch, B (1986). HEAT AND MASS TRANSFERWITH CONDENSATEION IN LAMINAR AND TURBULENT BOUNDARY LAYERS ALONG A FLAT PLATE, Int. J. Heat Mass Transfer, Vol. 29, No. 1, pp.95-105.
- [11] Matuszkiewicz, A. and Vernier, Ph. (1991). TWO-PHASE STRUCTURE OF THE CONDENSATION BOUNDARY LAYER WITH A NON-CONDENSING GAS AND LIQUID DROPLETS, Int. J. Multiphase Flow, Vol. 17, No. 2, pp. 213-225.
- [12] FLUENT INCORPORATED (1998). FLUENT 5 User's Guide.
- [13] Tannehill, J. C., Anderson, D. A. and Pletcher, R. H. (1997). COMPUTATIONAL FLUID MECHANICS AND HEAT TRANSFER, Second Edition. Taylor & Francis.
- [14] Bejan, A. (1993). HEAT TRANSFER. John Wiley & Sons, Inc.
- [15] Hinze, J. O. (1975). TURBULENCE, 2 ed., McGraw-Hill, New York.
- [16] Posey, S., Kremenetsky, M. and Jassim, A. (1999). PARALLEL PROCESSING IS BRINGING CFD CLOSER TO THE FLUIDS OF THE REAL WORLD. Mechanical Engineering, March 1999, pp. 57-59.
- [17] Bejan, A. (1995). CONCTION HEAT TRANSFER, SECOND EDITION. John Wiley & Sons, Inc.
- [18] Hoke, P. B., Wang, Q., McGrath, J. J. and AbdulNour B. S. (1999). EXPERIMENTAL AND NUMERICAL STUDY OF A CONDENSING FLOW IN A DEVELOPING WALL JET. Turbulence and Shear Flow Phenomena, First International Symposium, DoubleTree Resort, Santa Barbara, CA. September 12-15. (Publishing Pending)
- [19] Cengel, Y. A. and Boles, M. A. (1989). THERMODYNAMICS AN ENGINEERING APPROACH. McGraw-Hill, Inc.
- [20] Mabuchi, I. and Kumada, M. (1972). STUDY ON HEAT TRANSFER TO TURBULENT JETS WITH ADJACENT BOUNDARIES (1ST REPORT, FLOW DEVELOPMENT AND MASS TRANSFER IN PLANE

TURBULENT WALL JET), Bulletin of JSME, Vol 15, No. 88, pp. 1236-1245.